Die approbierte gedruckte Originalversion dieser Dissertation ist an der TU Wien Bibliothek verfügbar.
The approved original version of this doctoral thesis is available in print at TU Wien Bibliothek.

TECHNISCHE UNIVERSITÄT WIEN

Dissertation

Metal-oxide surfaces as a support for model single atom catalysis

ausgeführt zum Zwecke der Erlangung des akademischen Grades eines Doktors der technischen Wissenschaften unter der Leitung von

Univ.-Prof. Gareth S. Parkinson, PhD

Institut für Angewandte Physik (E134)

eingereicht an der Technischen Universität Wien, Fakultät für Physik
durch

Dipl.-Ing. Lena Puntscher
01426561

Wien, Jänner 2025

Acknowledgements

Working in this research group on my thesis has been an incredible experience—fun, exciting and also challenging in the best possible way. I want to begin by thanking Gareth Parkinson, who guided me through the past years with immense support and enthusiasms, always being available to answer my questions. I am grateful to Ulrike Diebold for sharing her wealth of knowledge and experience, and to Michael Schmid for solving countless technical problems an reviewing all our publications with an eye for detail.

I feel privileged to have been part of such a wonderful research group. The extremely friendly environment, supportive colleagues, and engaging discussions during lunch breaks made my time even more enjoyable. Scientifically, I have worked most closely with Panukorn Sombut and Chunlei Wang—thank you both for all the valuable discussions, your help, and the fun times we shared.

Finally, I want to thank my parents Elisabeth and Heinrich, my sister Theresa, and my husband Daniel for endless support and for making life so much better.

Die approbierte gedruckte Originalversion dieser Dissertation ist an der TU Wien Bibliothek verfügbar.
The approved original version of this doctoral thesis is available in print at TU Wien Bibliothek.

Die approbierte gedruckte Originalversion dieser Dissertation ist an der TU Wien Bibliothek verfügbar.
The approved original version of this doctoral thesis is available in print at TU Wien Bibliothek.

Abstract

Supported metal nanoparticles on metal oxides are widely utilized in heterogeneous catalysis. Downsizing these precious metal nanoparticles enhances the fraction of active surface atoms, improving the per-atom efficiency. Further reducing the size of nanoparticles ultimately reaches the single-atom scale, where individual metal atoms are anchored directly to the support, resulting in so called "single-atom" catalysts (SAC). SAC has emerged as a key strategy in the field of catalysis in the past decade, offering reduced precious metal usage and high selectivity, as the metal atoms coordinated to the support materials resemble organometallic complexes commonly used in homogeneous catalysis.

This thesis focuses on surface science studies of model SAC, to overcome the largely unknown atomic structures of metal atoms on various metal oxide supports. Understanding these structures is essential for fine-tuning catalytic systems to enhance efficiency and selectivity.

The work is divided into three main chapters, each addressing different metal oxide surfaces. The first chapter examines the influence of water vapour on the dispersion and sintering of Pt, Rh, Ni, and Ir adatoms on two well-defined TiO_2 surfaces, rutile $TiO_2(110)$ and anatase $TiO_2(101)$, by STM and XPS. Under UHV conditions, a trend in dispersion is observed, ranging from highly dispersed single atoms to predominantly clusters, with the order Ir $>$ Ni $>$ Pt $>$ Rh, which aligns with the oxygen affinity of the metals, with the exception of Pt. However, the impact of water vapour varies significantly: water promotes dispersion of Ni adatoms, induces sintering for Ir, and has little effect on Rh and Pt. The behaviour also differs between the two TiO_2 surfaces, highlighting the complexity of support-metal interactions.

The second chapter investigates the Rh/α-$Fe_2O_3(1\bar{1}02)$ system, where a previous study found that Rh forms clusters when deposited in UHV, but water vapour during deposition stabilizes Rh adatoms as single-atoms on the surface via coordination with OH ligands. For this thesis, nc-AFM with a CO-functionalized tip was utilized, identifying that two OH ligands stabilize the Rh adatoms, with occasional coordination of a third species, likely a water molecule.

The final chapter focuses on the Rh/$Fe_3O_4(001)$ system, aiming to understand the hydroformylation reaction catalysed by single Rh adatoms, by utilizing STM, TPD and XPS. Prior to the experiments with Rh, the interaction of C_2H_4 with the bare

surface was analysed. Then the adsorption of the individual reactants (CO, C_2H_4 and H_2) on the Rh adatoms was studied, along with the feasibility of co-adsorption of CO and C_2H_4. While co-adsorption was not observed at the given pressure regime, the study provides valuable insights into the interaction of reactants with Rh adatoms. Overall, these studies provide fundamental insights into the adsorption behaviour and reactivity of model SAC systems. They highlight the unpredictable yet crucial role of water in SAC, advance the understanding of metal-support interactions critical for optimizing catalytic systems, and analyse the fundamental steps of the industrially important hydroformylation reaction.

Die approbierte gedruckte Originalversion dieser Dissertation ist an der TU Wien Bibliothek verfügbar.
The approved original version of this doctoral thesis is available in print at TU Wien Bibliothek.

Die approbierte gedruckte Originalversion dieser Dissertation ist an der TU Wien Bibliothek verfügbar.
The approved original version of this doctoral thesis is available in print at TU Wien Bibliothek.

Kurzfassung

Nanopartikel aus katalytisch aktiven Metallen koordiniert zu Metalloxiden finden breite Anwendung in der heterogenen Katalyse. Eine Verkleinerung dieser Edelmetall Nanopartikel erhöht den Anteil aktiver Oberflächenatome und verbessert so die Effizienz pro Atom. Wenn man die Partikelgröße weiter reduziert, führt das schließlich zu einzelnen Metaltomen, welche direkt an die Trägeroberfläche gebunden sind. Diese sogenannten "Einzelatom-Katalysatoren" (SAC) haben sich in den letzten zehn Jahren als Schlüsselstrategie in der Katalyse etabliert, da sie nicht nur den Edelmetallverbrauch reduzieren, sondern auch eine hohe Selektivität bieten, da die Metallatome, die am Trägermaterial koordiniert sind, Organometall Komplexen ähneln, welche üblicherweise in der homogenen Katalyse verwendet werden.
Diese Doktorarbeit fokussiert sich auf Studien der Oberflächenpysik, an Modell SAC, um die weitgehend unbekannten atomaren Strukturen von Metallatomen auf verschiedenen Metalloxid Trägern zu entschlüsseln. Diese Strukturen zu verstehen ist entscheidend für das fine-tuning katalytischer Systeme um die Effizienz und Selektivität zu verbessern.
Die Arbeit ist in drei Hauptkapitel unterteilt, die jeweils unterschiedliche Metalloxidoberflächen behandeln. Das erste Kapitel untersucht den Einfluss von Wasserdampf auf die Dispersion und das Clustern von Pt-, Rh-, Ni- und Ir-Adatomen, anhand von STM und XPS, auf zwei wohldefinierten TiO_2-Oberflächen: Rutil $TiO_2(110)$ und Anatas $TiO_2(101)$. Unter UHV-Bedingungen wird ein Trend in der Dispersion beobachtet, der von hoch dispergierten Atomen zu überwiegend Clusters reicht, in der Reihenfolge Ir $>$ Ni $>$ Pt $>$ Rh, was mit der Sauerstoffaffinität der Metalle übereinstimmt, außer mit der von Pt. Der Einfluss von Wasserdampf variiert jedoch erheblich: Während Wasser die Dispersion von Ni-Adatomen fördert, induziert es das Clustern von Ir und hat nur wenig Einfluss auf Rh und Pt. Darüber hinaus unterscheiden sich die Ergebnisse zwischen den beiden TiO_2-Oberflächen, was die Komplexität der Träger-Metall Interaktionen verdeutlicht.
Das zweite Kapitel befasst sich mit dem Rh/α-$Fe_2O_3(1\bar{1}02)$ System, bei dem eine frühere Studie zeigte, dass Rh in UHV zu Clustern aggregiert, während Wasserdampf während der Deposition Rh als Einzelatome auf der Oberfläche durch Koordination mit OH-Liganden stabilisiert. Für diese Arbeit wurde nc-AFM mit CO-funktionalisierter Spitze verwendet. Dadurch konnte festgestellt werden, dass zwei

OH-Liganden die Rh-Adatome stabilisieren, und dass gelegentlich eine dritte Spezies, wahrscheinlich ein Wassermolekül, an das Rh Atom koordiniert ist.
Das abschließende Kapitel konzentriert sich auf das Rh/Fe_3O_4(001) System mit dem Ziel, die Hydroformylierung, katalysiert von einzelnen Rh Atomen, mittels STM, TPD und XPS zu verstehen. Vor den Experimenten mit Rh wurde die Interaktion von C_2H_4 mit der bloßen Oberfläche analysiert. Anschließend wurde die Adsorption der einzelnen Reaktanten (CO, C_2H_4 und H_2) an den Rh-Adatomen untersucht, ebenso wie die Möglichkeit einer Co-Adsorption von CO und C_2H_4. Während bei den gegebenen Druckverhältnissen keine Co-Adsorption beobachtet wurde, liefert die Studie wertvolle Einblicke in die Interaktion der Reaktanten mit Rh-Adatomen.
Insgesamt liefern diese Studien grundlegende Einblicke in das Adsorptionsverhalten und die Reaktivität von Modell-SAC Systemen. Sie verdeutlichen die unvorhersehbare, aber entscheidende Rolle von Wasser in SAC Systemen und erweitern das Verständnis von Träger-Metall Interaktionen, das für die Optimierung katalytischer Systeme von entscheidender Bedeutung ist. Weiter wurden grundlegende Schritte einer industriell wichtigen Reaktion, der Hydroformylierung, analysiert.

Die approbierte gedruckte Originalversion dieser Dissertation ist an der TU Wien Bibliothek verfügbar.
The approved original version of this doctoral thesis is available in print at TU Wien Bibliothek.

Contents

Die approbierte gedruckte Originalversion dieser Dissertation ist an der TU Wien Bibliothek verfügbar.
The approved original version of this doctoral thesis is available in print at TU Wien Bibliothek.
TU Bibliothek Your knowledge hub WIEN

Die approbierte gedruckte Originalversion dieser Dissertation ist an der TU Wien Bibliothek verfügbar.
The approved original version of this doctoral thesis is available in print at TU Wien Bibliothek.

1 Introduction

1.1 Single-Atom Catalysis (SAC)

Catalysis plays a major role in modern industry, enabling the large-scale production of chemicals, fuels, and pharmaceuticals. The majority of industrial catalysts consist of metal nanoparticles supported on substrates, which facilitate reactions by providing multiple active sites. However, these nanoparticle-based catalysts often require substantial amounts of precious metals, resulting in high costs and, in some cases, suboptimal efficiency, as only the outermost metal atoms participate in catalysis. While Pt-group metals are among the most effective catalysts, they are rare and expensive. Consequently, downsizing these materials and maximising the surface area relative to the volume has become a significant focus in recent years. Single-atom catalysis (SAC) [1–3] represents a promising advancement in catalyst downsizing. In SAC, isolated metal atoms are dispersed and stabilized on a cheap support material. This design maximizes atom efficiency by ensuring that each atom serves as an active site, enabling the optimal use of precious metals. When exclusively single atoms are adsorbed on the support, SAC can achieve high selectivity, unlike nanoparticles, which often struggle with selectivity issues due to variations in cluster size. Moreover, the local structure of the active metal atom, coordinated to surface atoms from the support material, closely resembles that of organometallic complexes due to its charged state and coordination with multiple ligands. [4–6] Organometallic complexes are commonly employed in homogeneous catalysis, where their well-defined coordination environment facilitates high selectivity and reactivity. As a result, SAC not only significantly reduces the amount of precious metal required but it also combines advantages of both heterogeneous and homogeneous catalysis. At the same time, it eliminates key disadvantages of homogeneous catalysis, such as separation challenges of the catalyst and the reactants as well as environmental impact. Consequently, SAC serves as a bridge between heterogeneous and homogeneous catalysis, opening

Die approbierte gedruckte Originalversion dieser Dissertation ist an der TU Wien Bibliothek verfügbar.
The approved original version of this doctoral thesis is available in print at TU Wien Bibliothek.

new possibilities in the field of catalysis.

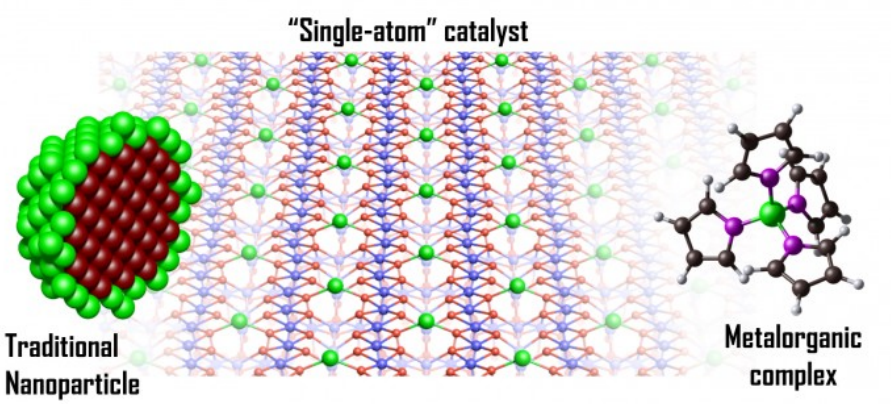

Figure 1.1: Catalytically active single atoms (green atoms) supported on inexpensive materials combine the benefits of heterogeneous catalysis, such as high stability with the advantages of homogeneous catalysis, such as high selectivity, while eliminating the loss of precious metals often trapped within nanoparticles (red atom, right side). Reprinted from [7].

It has been known for a while that single metal atoms supported on inexpensive materials, such as metal oxides, can catalyse reactions. [8–10] However, a 2011 study by Zhang et al. on the Pt_1/FeO_x system demonstrated that this catalyst was more active for low-temperature CO oxidation than Au and highly selective in the presence of H_2 [11]. This study sparked significant interest in the field of SAC, leading to a rapidly increase in publications exploring SAC in heterogeneous, photocatalytic, and electrocatalytic reactions. [1–3, 12, 13]

SAC exhibits unique properties across various reactions, including oxidation reactions, water-gas shift, and hydrogenation reactions. [14–18] Despite these promising applications, the underlying mechanisms of SAC remain incompletely understood.

The primary challenge in SAC remains the aggregation of single metal atoms into nanoclusters during the synthesis. Therefore, developing methods to synthesize thermally stable SAC is essential for maximizing efficiency and performance. [13, 19, 20]. Typically, in SAC synthesis, the metal atoms are deposited onto the support from solution. The resulting catalyst is then separated, dried, and calcined to remove remaining organic ligands. To confirm the dispersion of metal atoms on the surface, scanning transmission electron microscopy (STEM) is employed [21], which allows for

Die approbierte gedruckte Originalversion dieser Dissertation ist an der TU Wien Bibliothek verfügbar.
The approved original version of this doctoral thesis is available in print at TU Wien Bibliothek.
TU Bibliothek Your knowledge hub WIEN

the identification of heavy atoms against the lighter support material. However, while STEM reveals the presence of metal atoms, it does not provide information about their coordination environment, oxidation state, or interactions with adsorbed reactants. To address this, X-ray absorption near-edge structure (XANES) and infrared absorption spectroscopy (IRAS) are used to gather data on the average coordination and charge state of the atoms. Nevertheless, the precise atomic structure of the metal atoms often remains elusive. Theoretical calculations are frequently employed to address this, but they typically rely on oversimplified models. This understanding, however, is critical for fine-tuning catalytic systems to enhance efficiency and selectivity.

1.2 The surface science approach

For an in-depth understanding of the coordination environment of active sites at the atomic level, the "surface science approach" was employed. This method utilizes well-defined single-crystalline surfaces to produce model SACs with uniformly dispersed metal adatoms. The surfaces are cleaned under ultra-high vacuum (UHV) conditions, and catalytically active metal atoms are subsequently vapour-deposited onto the support material. The model SAC are characterised using surface science techniques outlined in chapter 2. Reactivity studies are performed by exposing the catalysts to well-defined quantities of molecules at controlled temperatures. Finally, the experimental data are complemented by DFT+U calculations to provide a theoretical perspective.

1.3 Thesis outline

This thesis explores new potential model systems for their suitability, assess the impact of water on support-metal interactions and deals with the adsorption behaviour and reactivity of a well-established SAC model system. Four different metal-oxide surfaces were employed: two TiO_2 surfaces, rutile $TiO_2(110)$ and anatase $TiO_2(101)$

Die approbierte gedruckte Originalversion dieser Dissertation ist an der TU Wien Bibliothek verfügbar.
The approved original version of this doctoral thesis is available in print at TU Wien Bibliothek.
TU Bibliothek Your knowledge hub WIEN

and two iron oxide surfaces, α-$Fe_2O_3(1\bar{1}02)$ and $Fe_3O_4(001)$. These surfaces are described in section 1.4 and 1.5. All of the materials investigated are widely used in SAC, making the understanding of metal-support interactions and reactivity studies with model SAC systems essential for optimizing catalytic performance. Chapter 2 provides an overview of the methods employed in this work, along with a detailed description of the analysis chambers and standard experimental procedures.
Chapter 3 discusses the effects of water vapour during the deposition of several catalytically active metals onto the two TiO_2 surfaces employed. The results in this chapter have been published in the following peer-reviewed papers:

- Sombut, P., **Puntscher, L.**, Atzmueller, M., Jakub, Z., Reticcioli, M., Meier, M., Parkinson, G. S., Franchini, C., **Role of Polarons in Single-Atom Catalysts: Case Study of Me_1 [Au_1, Pt_1, and Rh_1] on TiO_2(110).** Topics in Catalysis 65, 1620–1630 (2022).

- **Puntscher, L.**, Daninger, K., Schmid, M., Diebold, U., Parkinson, G. S. **A study of Pt, Rh, Ni and Ir dispersion on anatase TiO_2(101) and the role of water.** Electrochimica Acta 449, 142190 (2023).

Chapter 4 discusses the effects of water vapour during the deposition of Rh onto α-$Fe_2O_3(1\bar{1}02)$. The results in this chapter have been published in the following peer-reviewed paper:

- Kraushofer, F., **Haager, L.**, Eder, M., Rafsanjani-Abbasi, A., Jakub, Z., Franceschi, G., Riva, M., Meier, M., Schmid, M., Diebold, U., Parkinson, G. S. **Single Rh adatoms stabilized on α-$Fe_2O_3(1\bar{1}02)$ by coadsorbed water.** ACS Energy Letters 7, 375–380 (2021).

In Chapter 5, the adsorption behaviour of a well-established model SAC system—single dispersed Rh adatoms stabilized on the $Fe_3O_4(001)$ surface—was investigated. The primary objective was to gain deeper insights into the hydroformylation reaction catalysed by a SAC. Prior to conducting experiments with Rh, the interaction of C_2H_4, with the bare surface was analysed. Next, the adsorption behaviour of C_2H_4 and H_2 with Rh adatoms was investigated and finally, the feasibility of co-adsorption of CO and C_2H_4 on Rh adatoms was analysed. Parts of the results presented in this chapter have been published in the following peer-reviewed papers:

Die approbierte gedruckte Originalversion dieser Dissertation ist an der TU Wien Bibliothek verfügbar.
The approved original version of this doctoral thesis is available in print at TU Wien Bibliothek.
TU Bibliothek Your knowledge hub WIEN

- **Puntscher, L.**, Sombut, P., Wang, C., Ulreich, M., Pavelec, J., Rafsanjani-Abbasi, A., Meier, M., Lagin, A., Setvin, M., Diebold, U., Franchini, C., Schmid, M., Parkinson, G. S. **A Multitechnique Study of C_2H_4 Adsorption on Fe_3O_4(001).** The Journal of Physical Chemistry C 127, 18378–18388 (2023).

- Wang, C., Sombut, P., **Puntscher, L.**, Ulreich, M., Pavelec, J., Rath, D., Balajka, J., Meier, M., Schmid, M., Diebold, U., Franchini, C., Parkinson, G. S. **A Multi-Technique Study of C_2H_4 Adsorption on a Model Single-Atom Rh_1 Catalyst.** The Journal of Physical Chemistry C 128, 15404–15411 (2024).

Die approbierte gedruckte Originalversion dieser Dissertation ist an der TU Wien Bibliothek verfügbar.
The approved original version of this doctoral thesis is available in print at TU Wien Bibliothek.

1.4 Titanium dioxide

Titanium dioxide, also known as titania, is a transition metal oxide with the chemical formula TiO_2. It is a semiconductor with a wide band gap and has a broad range of applications, including photocatalysis [22–24], solar cells [25], gas sensors [26] and biosensors [27, 28]. Due to its bright white colour, very high refractive index, low cost, and non-toxic properties, TiO_2 is also the most commonly used white pigment in paints, fibers, papers, food colouring and sunscreen. [29]

TiO_2 primarily crystallizes in three different structures: rutile (a = b = 4.584 Å) [30] and anatase (a = b = 3.782 Å, c = 9.502 Å), both of which exhibit tetragonal symmetry, and brookite (a = 5.436 Å, b = 9.166 Å, c = 5.135 Å) which has rhombohedral symmetry. [31] Among these, rutile is the most stable structure and most commonly occurs in nature. For practical applications, however, only the rutile and anatase phases are of significance. Both of their building blocks consist of a Ti atom coordinated to six O atoms. Their unit cells are illustrated in Figure 1.2.

The Ti-O system exhibits a large number of stable phases with various possible crystal structures. [31] As a result, TiO_2 is easily reduced. Reducing the thermodynamically stable rutile TiO_2 single crystals induces a color transformation from their initial transparency to a deep blue. Intrinsic defects arising from the reduction process lead to n-type doping, which imparts conductivity to the single crystals. This characteristics renders rutile TiO_2 single crystals an advantageous system for surface science studies. The (110) facet of rutile TiO_2 exhibits the highest energy stability and has been extensively studied using surface science techniques. To date, it is one of the best-characterized surface. [32]

While large single crystals favour the thermodynamically stable rutile phase, anatase is more stable at the nanoscale due to the low free energy exhibited by the (101) surface. Consequently, the anatase polymorph plays a more crucial role in nanotechnology than the rutile phase. For instance, most photovoltaic cells are based on porous thin films of anatase TiO_2. [33] In the field of SAC, the anatase phase is particularly important, as nanoparticles of anatase are commonly used as support material. [34] However, obtaining large, pure single crystals of the anatase phase is significantly more challenging. Anatase is metastable and transforms into rutile at relatively low temperatures. [35] Nonetheless, extensive surface science research has been conducted on anatase, especially on its facet with the lowest surface energy, the

Die approbierte gedruckte Originalversion dieser Dissertation ist an der TU Wien Bibliothek verfügbar.
The approved original version of this doctoral thesis is available in print at TU Wien Bibliothek.
TU Bibliothek Your knowledge hub WIEN

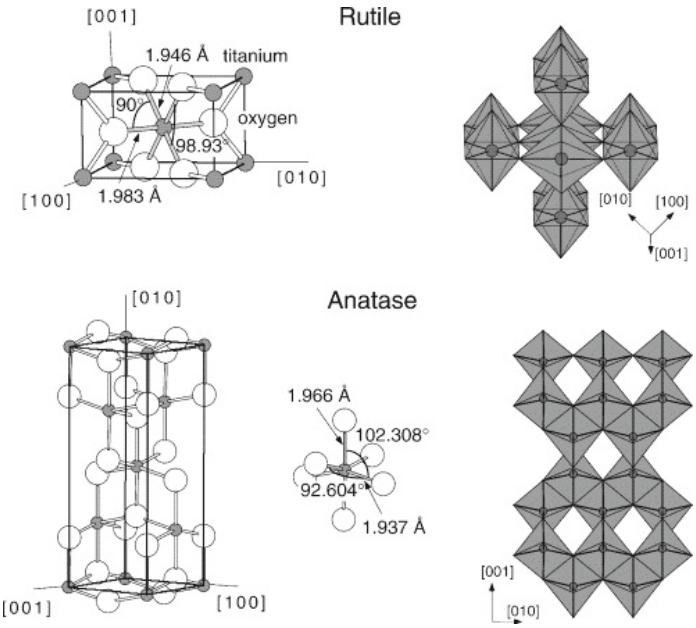

Figure 1.2: Bulk structure of rutile and anatase TiO_2. Both of their building blocks consist of a Ti atom coordinated to six O atoms in a slightly distorted octahedral symmetry. Bond lengths and angles of the Ti atoms are indicated on the left side. On the right side, the stacking of the octahedra for both structures is shown. Reprinted from [32].

anatase TiO_2(101) surface. [36, 37]
This thesis focuses on the most stable facets of rutile and anatase: the rutile TiO_2(110) surface and the anatase TiO_2(101) surface, as support material for model SAC.

1.4.1 The rutile TiO_2(110) surface

Rutile TiO_2(110) is one of the most extensively studied systems in surface science. [32, 38, 39] This is primarily due to the availability of high-quality single-crystalline samples, which are both widely accessible and inexpensive, as well as to the straightforward preparation of the surface under UHV conditions. The (110) facet is a Tasker Type 2 surface [40], characterized by a charge neutral repeat unit without a dipole moment perpendicular to the surface. Similar to the bulk, the rutile TiO_2(110) surface is semiconducting, with a band gap of ≈3 eV. [41]
The structure of this surface is well-characterised from previous studies. Quantita-

Die approbierte gedruckte Originalversion dieser Dissertation ist an der TU Wien Bibliothek verfügbar.
The approved original version of this doctoral thesis is available in print at TU Wien Bibliothek.
TU Bibliothek Your knowledge hub WIEN

tive structural techniques such as SXRD and LEED *I(V)* [42, 43], scanning probe microscopy studies [44], and DFT calculations [45] confirm the model of the surface shown in side and top view in Figure 1.3. The surface is composed of two types of Ti and O atoms. Rows of 6-fold coordinated Ti atoms (Ti_{6c}) alternate with rows of 5-fold coordinated Ti atoms (Ti_{5c}) along the $[\bar{1}10]$ direction, with the Ti_{5c} atoms having a dangling bond perpendicular to the surface. This arrangement creates a surface where every other row of terminal O atoms is missing. 2-fold coordinated O atoms, known as bridging O (O_{br}), are bonded to two Ti_{6c} and protrude from the surface. The other type of surface O, 3-fold coordinated O atoms (O_{3c}), resemble the O atoms in the bulk structure. Along the $[\bar{1}10]$ direction, one row of O_{br} alternates with two rows of O_{3c}, with a row of Ti_{5c} in between.

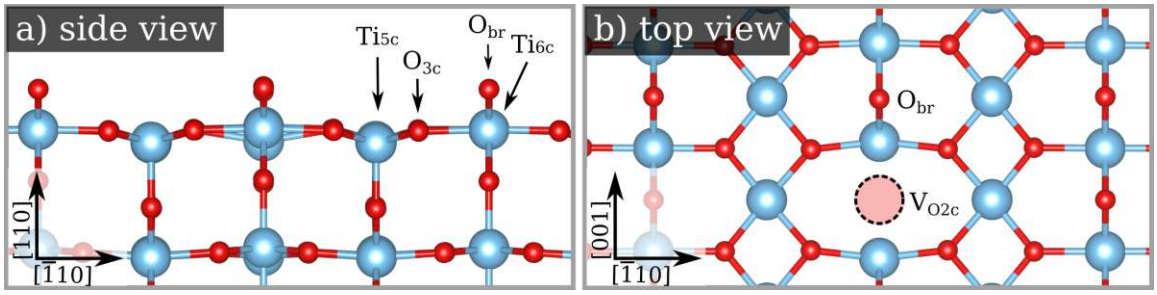

Figure 1.3: Model of the rutile $TiO_2(110)$ surface. O atoms are shown in red, Ti atoms are shown in blue. a) presents a side view of the surface, with two different types of Ti and O atoms marked by arrows. In the top view (b), the position of an oxygen vacancy ($V_{O_{2c}}$) is indicated by a circle.

To obtain a clean and flat surface, which is essential for STM imaging, the sample is typically prepared in vacuum through cycles of ion sputtering (for this thesis: 1 keV, Ar^+, 15 min) followed by high-temperature annealing (for this thesis: 700–800 °C, 20 min). Sputtering preferentially removes O atoms, as they are lighter than the Ti atoms. During subsequent annealing, the surface is partially restored, with the oxygen deficiency most easily accommodated in the bridging O row. As a result, intrinsic oxygen vacancies ($V_{O_{2c}}$) are created throughout the cleaning cycles. ($V_{O_{2c}}$ are shown Figure 1.3 b) and Figure 1.4 a)). Each $V_{O_{2c}}$ acts as an e^- donor, contributing two excess electrons to the material. When the sample is annealed at high temperatures, bulk-assisted reoxidation occurs, partially restoring the surface through migration of O atoms from the bulk. After several sputter and anneal cycles, this process leads to

Die approbierte gedruckte Originalversion dieser Dissertation ist an der TU Wien Bibliothek verfügbar.
The approved original version of this doctoral thesis is available in print at TU Wien Bibliothek.
TU Bibliothek Your knowledge hub WIEN

an overall reduction and n-type doping of the sample. Additionally, excess Ti^{3+} ions from the sputtered surface diffuse into the bulk, further reducing the sample. [46] The reduced rutile $TiO_2(110)$ surface is commonly reffered to as r-$TiO_2(110)$.
STM imaging is typically performed in empty-state mode (with a positive sample bias), enabling electrons to tunnel from the tip into the empty states of the conduction band. Imaging in filled-state mode (with a positive sample bias) is more challenging due to the ≈3 eV band gap, which nominally does not contain any energy levels. In this case, the excess electrons which are donated to the material by defects can be directly imaged.
An empty state STM image of the r-$TiO_2(110)$ surface is shown in Figure 1.4 a). Dark and bright rows alternate along the $[1\bar{1}0]$ direction, with the dark rows occasionally interrupted by bright features. Intuitively, one might expect the brighter rows, which appear higher in apparent height, to correspond to the protruding O_{br} rows and the geometrically lower Ti_{5c} rows to correspond to the dark rows. However, the opposite is true because the STM image contrast is dominated by the electronic structure of the surface. [47] O atoms rarely have electronic states near the Fermi level, so the O_{br} do not contribute to the STM image and appear in a dark contrast. Instead, the cationic Ti_{5c} are imaged and appear in a brighter contrast. The surface unit cell of rutile $TiO_2(110)$ is rectangular, with side lengths of 6.48 Å along the $[\bar{1}10]$ direction and 2.95 Å along the [001] direction (see Figure 1.4 a)).
The most common defect, the aforementioned $V_{O_{2c}}$, is marked with an arrow in Figure 1.4 a). This defect exposes the underlying Ti atoms, which appear as white feature on the dark rows.
While sputtering and annealing above 700 °C creates an almost stoichiometric (1×1) surface (Figure 1.4 a)), a reconstruction forms when the reduced surface is annealed at lower temperatures. In STM, this reconstruction appears as bright strings along the [001] direction (Figure 1.4 b)). It exhibits a (2×1) symmetry, with a doubling of periodicity along the $[1\bar{1}0]$ direction. [48]
This thesis investigates the influence of water on metal adatoms deposited on the r-$TiO_2(110)$ surface. Therefore, it is essential to understand the adsorption and interaction of water with the bare r-$TiO_2(110)$ surface. A TPD based study assigns the monolayer desorption peak on the stoichiometric surface to 275 K, attributed to chemisorbed water molecules bonded to Ti^{4+} sites. The multilayer desorption peak is assigned to 160 K. [49]

Die approbierte gedruckte Originalversion dieser Dissertation ist an der TU Wien Bibliothek verfügbar.
The approved original version of this doctoral thesis is available in print at TU Wien Bibliothek.
TU Bibliothek Your knowledge hub WIEN

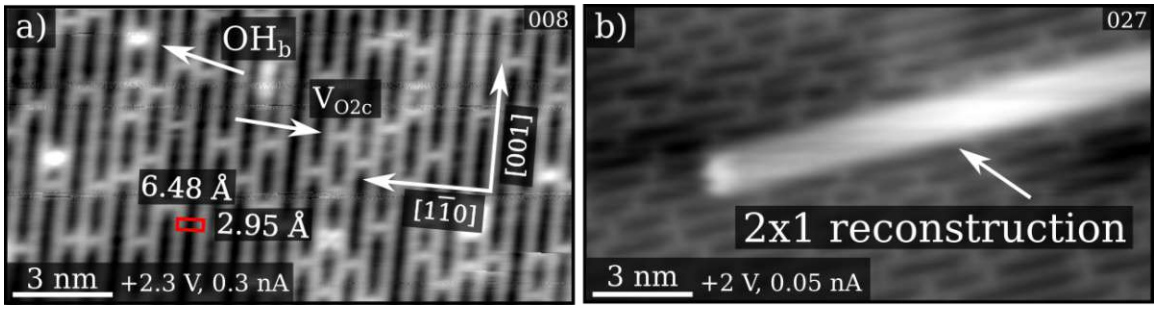

Figure 1.4: RT-STM images of r-TiO_2(110). a) shows the surface with (1×1) symmetry. The bright rows correspond to Ti_{5c}, while the dark rows correspond to O_{br}. Two defects are marked with arrows: on the left side, an oxygen vacancy ($V_{O_{2c}}$) and, on the ride side, a bridging hydroxyl (OH_b). The latter forms when a water molecule from the residual gas in the UHV chamber dissociates at a $V_{O_{2c}}$, filling the vacancy with a hydroxyl group. The unit cell is marked with a red rectangle. b) shows the most common reconstruction of r-TiO_2(110), displaying (2×1) symmetry.

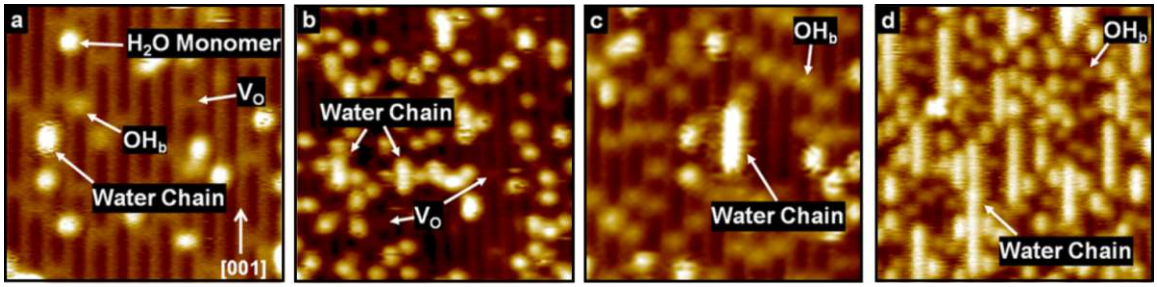

Figure 1.5: STM images of water interaction with the r-TiO_2(110) surface. a) (1.5 V, 10 pA) shows the surface at 50 K with 0.04 ML water coverage, where short water chains, water monomers, and OH_b are visible. b) (1.5 V, 10 pA) shows the surface at 50 K with 0.13 ML water coverage, revealing longer one-dimensional water chains. c) (1.5 V, 10 pA) shows the surface at 50 K after annealing the sample in b) to 190 K for 5 min. The water chain appears streaky at the edges. d) (1.5 V, 10 pA) shows the surface at 50 K with 0.5 ML water coverage after annealing to 190 K for 5 min. Adapted from [50]

Die approbierte gedruckte Originalversion dieser Dissertation ist an der TU Wien Bibliothek verfügbar.
The approved original version of this doctoral thesis is available in print at TU Wien Bibliothek.
TU Bibliothek Your knowledge hub WIEN

When the reduced surface is exposed to water molecules at room temperature, $V_{O_{2c}}$ sites act as active sites for water dissociation, leading to the adsorption of hydroxyl groups. The hydroxyl groups form so-called bridging hydroxyl defects (OH_b) (marked with an arrow in Figure 1.4 a)). [51, 52] If water vapour is dosed at low temperature (50 K) onto the r-TiO_2(110) surface and subsequently heated to 190 K, the adsorbed water molecules organize into one-dimensional chains along the Ti rows (shown in Figure 1.5). At low coverage, isolated water molecules can also be observed on the Ti rows under the same conditions (Figure 1.5 a)) [50]

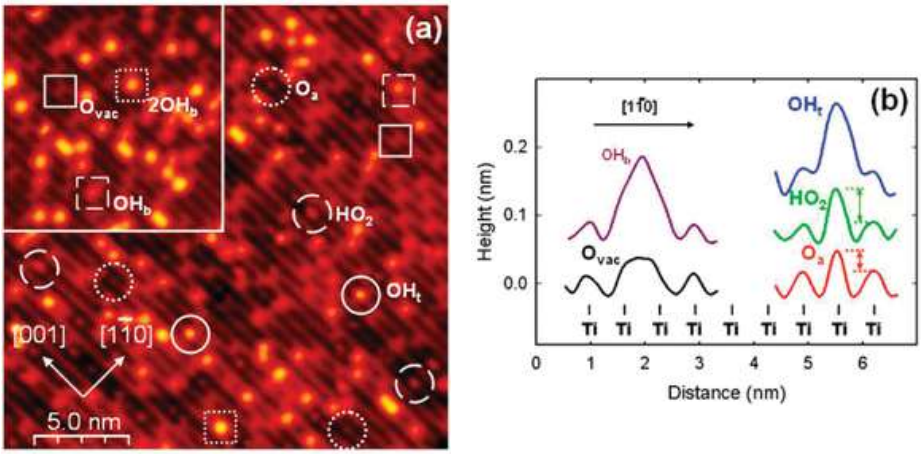

Figure 1.6: STM image of a partially hydroxylated r-TiO_2(110) surface after exposure to O_2. The inset in a) shows the surface prior to O_2 exposure. b) presents a line profile of the apparent height of various features along the [1$\bar{1}$0] direction. Reprinted from [53]

In addition to water, the influence of O_2 on model SAC systems on r-TiO_2(110) was studied. It has been demonstrated that O_2 dissociates at the $V_{O_{2c}}$ sites, with one O atom filling the O vacancy, while the other one adsorbs on the Ti_{5c} sites, forming a species referred to as O_a (see Figure 1.6). On a partly hydroxylated r-TiO_2(110) surface, hydroxylated $V_{O_{2c}}$ sites react with O_a species, healing the vacancy and forming so-called terminal hydroxyls (OH_t). These OH_t groups adsorb at Ti_{5c} sites and occur slightly brighter than the O_a species in the STM images (see Figure 1.6). [53]

Die approbierte gedruckte Originalversion dieser Dissertation ist an der TU Wien Bibliothek verfügbar.
The approved original version of this doctoral thesis is available in print at TU Wien Bibliothek.
TU Bibliothek Your knowledge hub WIEN

1.4.2 The anatase TiO_2(101) surface

To gain a deeper understanding of SAC on TiO_2, it is essential to study not only the rutile phase but also the anatase phase. As mentioned earlier, TiO_2 in its nanocrystalline anatase phase is predominantly used as a support material in SAC. The thermodynamically most stable anatase TiO_2(101) surface has a band gap of ≈3.2 eV. [41]

While synthesizing single crystals of the rutile phase is relatively straightforward, obtaining large single-crystalline anatase samples is more challenging. Although anatase can be grown synthetically, this typically results in relatively small and expensive samples. [41] Alternatively, relatively pure, naturally occurring single-crystalline mineral samples can be found in nature. [54, 55] Despite the difficulties in obtaining suitable samples for surface science experiments, the anatase TiO_2(101) surface is now relatively well-characterised. In LEED, it exhibits a (1×1) symmetry. [37] Due to the surface's pm symmetry, the terraces have a triangular shape, and the step edges show a preferable orientation. [56]

The anatase TiO_2(101) surface features a sawtooth-like termination, with Ti atoms being 5-fold and 6-fold coordinated and O atoms being 2-fold and 3-fold coordinated (shown in Figure 1.7). The O_{2c} atoms are located at the ridge of the sawtooth-like structure. [36, 37]

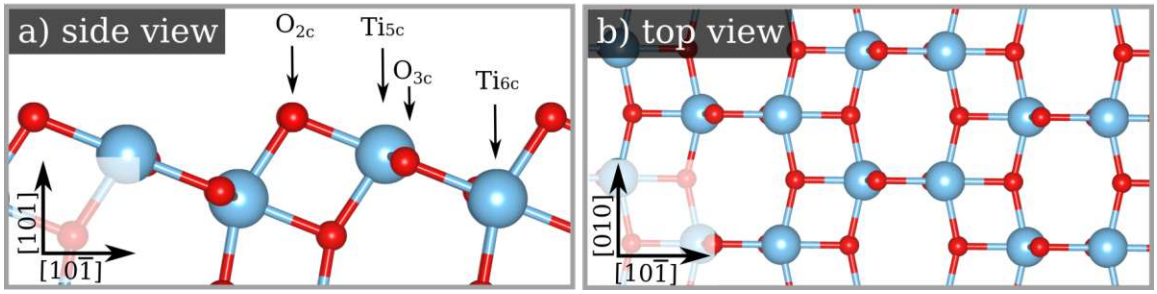

Figure 1.7: Model of the anatase TiO_2(101) surface. The surface exhibits a sawtooth like termination with fully coordinated and undercoordinated Ti and O atoms, respectively. (marked with an arrow in a)). The O atoms are coloured red and the Ti atoms are coloured blue.

Experiments for this thesis were conducted on a single-crystalline mineral sample. The surface preparation resembles the preparation of rutile TiO_2(110). Cycles of ion

Die approbierte gedruckte Originalversion dieser Dissertation ist an der TU Wien Bibliothek verfügbar.
The approved original version of this doctoral thesis is available in print at TU Wien Bibliothek.
TU Bibliothek Your knowledge hub WIEN

sputtering (for this thesis: 1 keV, Ar^+, 10 min) and subsequent high-temperature annealing (for this thesis: 600–620 °C, 20 min) in UHV were carried out. To reoxidise, after lattice oxygen was preferentially removed during ion sputtering, and to flatten the surface, the sample was annealed in O_2 at a partial pressure of $5 \cdot 10^{-7}$ mbar. It should be noted that reoxidising the single crystal at temperatures higher than 450 °C leads to Fe segregation to the surface, as Fe is present in the crystal as a bulk impurity. [57] For this reason, the sample was reoxidised (for this thesis: 400 °C, 20 min) after every 5^{th} cleaning cycle.

One might expect that reducing the sample through ion sputtering and UHV annealing would easily remove the O_{2c} atoms, creating a defect similar to that observed on the rutile TiO_2(110) surface. However, surface O vacancies on the anatase TiO_2(101) surface are unstable. Even when O vacancies are generated via electron bombardment, they diffuse into the bulk at relatively low temperatures, [58, 59] and remain as subsurface vacancies. [60] A possible explanation for the absence of surface oxygen vacancies on the anatase TiO_2(101) surface is the strong binding of O_{2c} atoms to Ti_{5c} sites. On the rutile TiO_2(110) surface, O_{br} atoms are coordinated to Ti_{6c}. Removing O_{2c} atoms from the anatase TiO_2(101) surface results in two 4-fold coordinated Ti^{3+} cations, whereas removing O_{br} atoms from the rutile TiO_2(110) surface leaves two 5-fold coordinated Ti^{3+} cations. The highly undercoordinated Ti cations on the anatase TiO_2(101) surface are likely less stable than the Ti cations on the rutile TiO_2(110) surface.

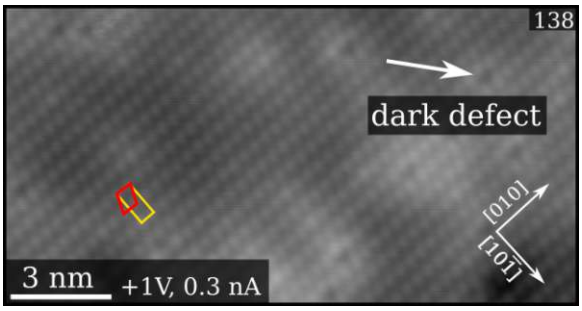

Figure 1.8: RT-STM image of the anatase TiO_2(101) surface. a) shows the surface after several cleaning cycles in UHV. The primitive surface unit cell is marked in red (a = 3.78 Å, b = 5.46 Å and $\alpha = 110°$) and the rectangular unit cell is marked in yellow (a = 3.78 Å, b = 10.24 Å). Inhomogeneously distributed dark defects are marked with an arrow.

Die approbierte gedruckte Originalversion dieser Dissertation ist an der TU Wien Bibliothek verfügbar.
The approved original version of this doctoral thesis is available in print at TU Wien Bibliothek.
TU Bibliothek Your knowledge hub WIEN

Figure 1.8 a) shows RT-STM images of the anatase TiO_2(101) surface after several cleaning cycles. Rows of oval-shaped protrusions run along the [010] direction and are attributed to Ti_{5c} and O_{2c} atoms, with the tunnelling signal extending across both of the species. [56] Dark features between the rows (marked with an arrow in 1.8) are inhomogeneously distributed over the surface. The features were previously assigned to extrinsic Nb dopants, as Nb is commonly present in mineral anatase TiO_2 samples. [58] However, in this thesis, it was not possible to detect Nb in the XPS survey spectra, likely because the coverage, measured by STM to be 0.02–0.03 ML, is too low.

The influence of co-adsorbed water on metal adatoms was also investigated on the anatase TiO_2(101) surface. A TPD study has shown that water desorbs from the anatase TiO_2(101) surface below 250 K [61]. However, after exposing the sample to the residual gas, water molecules were observed, likely adsorbed at surface defects. (More details can be found in chapter 3.3)

Die approbierte gedruckte Originalversion dieser Dissertation ist an der TU Wien Bibliothek verfügbar.
The approved original version of this doctoral thesis is available in print at TU Wien Bibliothek.

1.5 Iron oxides

Iron oxides are highly abundant, stable, and non-toxic materials, making them ideal as a support in SAC. In addition to functioning as a support material, iron oxides possess catalytic properties and are employed in various processes, including Fischer–Tropsch synthesis, Fenton oxidation, ethylbenzene dehydrogenation, and photoelectrochemical water splitting. [62–65] Apart from catalysis, they are also utilized in several technological applications, such the steel production, biomedical applications [65, 66] and as energy storing media [67].

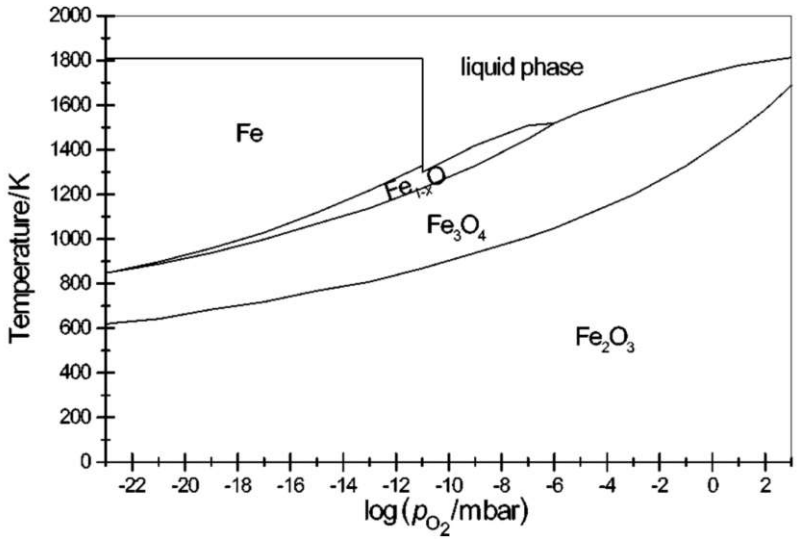

Figure 1.9: Calculated temperature-pressure phase diagram of the Fe-O system. Reprinted from [68]

Figure 1.9 shows the phase diagram of the Fe-O system. At ambient conditions, hematite (α-Fe_2O_3) is the energetically most favoured form of iron oxide and thus the most abundant. Magnetite (Fe_3O_4), however, is only stable under reducing conditions, such as elevated temperatures or low oxygen pressure. Nevertheless, it is highly abundant at ambient conditions due to the significant energetic cost of recrystallization to hematite. Maghemite (γ-Fe_2O_3), an intermediate phase between hematite and magnetite, has a Fe_2O_3 stoichiometry but is isostructural to magnetite because of randomly distributed iron vacancies. This intermediate state is also commonly found in nature. The least stable form is wüstite ($Fe_{1-x}O$), which is only stable un-

Die approbierte gedruckte Originalversion dieser Dissertation ist an der TU Wien Bibliothek verfügbar.
The approved original version of this doctoral thesis is available in print at TU Wien Bibliothek.
TU Bibliothek Your knowledge hub WIEN

der strong reducing conditions making it rare in nature.
This thesis primarily focuses on the two most stable forms of iron oxides: hematite and magnetite.

1.5.1 Hematite

Hematite is the most oxidized form of iron oxide and crystallizes in the corundum structure. [69] Figure 1.10 shows the hexagonal unit cell (a = 5.04 Å, c = 13.75 Å [70]) (a) and the respective face-sharing octahedra (b), as well as the primitive rhombohedral unit cell (a= 5.44 Å, α = 55.2° [70]) (c) and the respective face-sharing ocathedra (d). Because of its hexagonal structure, the crystallographic directions are commonly given in a four-digit notation.

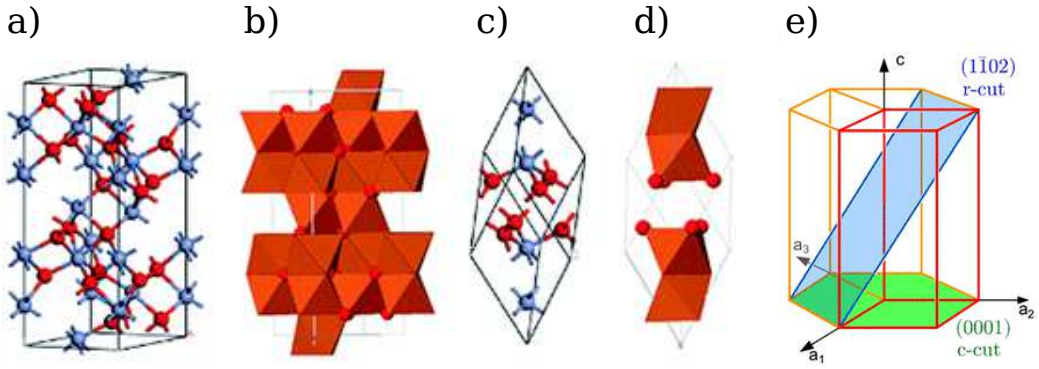

Figure 1.10: Ball and stick model of the crystal structure of hematite (a-d). In a) the hexagonal and in c) the primitive rhombohedral unit cell is shown. b) and d) show the face-sharing octahedra of the hexagonal and rhombohedral unit cell. Fe atoms are coloured grey and O atoms red. In e) the (0001) and the (1$\bar{1}$02) planes of the corundum structure are highlighted. The hexagonal unit cell is marked in red. Adapted from [71] and [72]

Hexagonal close-packed (hcp) planes of O^{2-} anions are stacked along the [0001] direction, with Fe^{3+} cations occupying two-thirds of the interstitial octahedral sites. A slight distortion from the ideal packing arises due to repulsion between neighbouring occupied face sharing octahedra. Consequently, the cations shift towards the unshared faces, leading to two different Fe-O bond lengths of 1.96 Å and 2.12 Å. [71, 73]

Die approbierte gedruckte Originalversion dieser Dissertation ist an der TU Wien Bibliothek verfügbar.
The approved original version of this doctoral thesis is available in print at TU Wien Bibliothek.
TU Bibliothek Your knowledge hub WIEN

At low temperatures, hematite is antiferromagnetic, with the spins perpendicular to the (0001) plane. Spin-canting occurs at the Morin temperature (260 K), resulting in spin orientation within the (0001) plane. Above 260 K, the ferromagnetic interaction is weak due to the spins not being perfectly antiparallel. [74] In its natural form, and in the absence of impurities, the conductivity is low and anisotropic. [75] The conductivity along the [0001] direction is higher by four orders of magnitude compared to perpendicular to the [0001] direction. This is due to the magnetic structure, which facilitates electron movement within the Fe layers but restricts it across the oxygen planes. [76–78]
Natural hematite crystals expose several low-index surfaces, with the (0001) and $(1\bar{1}02)$ facets being energetically favoured and commonly observed in nature, a finding supported by DFT calculations. [79] The (0001) surface, referred to as the c-cut surface and the $(1\bar{1}02)$, referred to as the r-cut surface are seen in Figure 1.10 e). While the (0001) surface has extensively been studied, it is challenging to prepare a stoichiometric surface under UHV conditions. [80] The $(1\bar{1}02)$ surface has received less attention, but recent surface science studies unravelled its surface termination. [72]
In this thesis the $Fe_2O_3(1\bar{1}02)$ surface was used as a support material for SAC.

1.5.2 The α-$Fe_2O_3(1\bar{1}02)$ surface

Two different surface terminations are known to form on the $Fe_2O_3(1\bar{1}02)$ surface under UHV conditions. The first is a stoichiometric bulk-truncated surface with (1 × 1) symmetry. Due to the stacking of positive and negative planes in the repeat unit, there is no dipole moment perpendicular to the surface, which is characteristic for a Tusker type 2 surface. [40] Experimental evidence from Low Energy Electron Diffraction (LEED) and Auger Electron Spectroscopy (AES) already suggested a bulk-truncated termination over 30 years ago. [81, 82] A more recent study by Kraushofer et al. combined several surface science techniques and DFT+U based calculations to further analyse the α-$Fe_2O_3(1\bar{1}02)$ surface, containing the first STM and nc-AFM images on this surface. [72] Figure 1.11 shows a top and side view of the corresponding model. Characteristic for this surface termination are the zig-zag rows of O and Fe running along the $[\bar{1}101]$ direction.
The second surface termination forms under reducing conditions leading to a recon-

Die approbierte gedruckte Originalversion dieser Dissertation ist an der TU Wien Bibliothek verfügbar.
The approved original version of this doctoral thesis is available in print at TU Wien Bibliothek.
TU Bibliothek Your knowledge hub WIEN

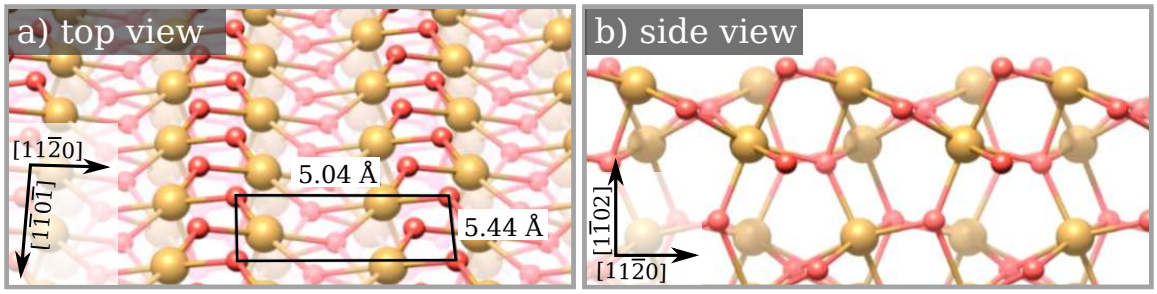

Figure 1.11: Model of the bulk-truncated α-$Fe_2O_3(1\bar{1}02)$ surface in top view a) and side view b). Characteristic zig-zag rows of surface Fe and O are clearly visible in the top view. The surface unit cell (a = 5.04 Å, b = 5.44 Å) is highlighted in a). O is coloured red, Fe is coloured yellow.

struction with a (2 × 1) symmetry. Several models for this reconstruction have been proposed in the past, based on the presence of O vacancies or the removal of every other oxygen zig-zag row. These models were derived solely from spectroscopic and diffraction data. [83, 84] The study by Kraushofer et al. proposes a new model for the surface reconstruction. [72]

To create the (1 × 1) symmetry, the surface must be annealed in an O_2 environment, whereas obtaining the (2 × 1) symmetry requires high temperatures under UHV conditions. [85]

Only the bulk-truncated surface was utilized in this thesis. Figure 1.12 shows typical STM and nc-AFM images of the as-prepared surface. Based on STM, it is believed that the Fe sublattice is imaged in empty state mode, with the bright zig-zag rows along the [$\bar{1}$101] direction corresponding to surface Fe. They are 5 Å apart, which fits well with the surface model calculated by DFT+U. In contrast to STM, which primarily detects electronic structures, nc-AFM responds more to the positions of atoms and their chemical identities. A short-range interaction between tip and surface on oxide surfaces leads to images dominated by ionic and covalent interactions [86–88], and can further be influenced by Pauli repulsion [89] and tip bending [90]. Thus, depending on the tip termination and its reactivity with the surface, either a strong attractive or a localized repulsive interaction with the surface ions is recognized. Studies on TiO_2 have demonstrated that anionic terminated tips feel attractive interaction with surface cations, whereas the interaction with the O atoms is repulsive and significantly weaker, and that the opposite is true for cationic terminated tips.

Die approbierte gedruckte Originalversion dieser Dissertation ist an der TU Wien Bibliothek verfügbar.
The approved original version of this doctoral thesis is available in print at TU Wien Bibliothek.
TU Bibliothek Your knowledge hub WIEN

[87, 88, 91]. It is assumed that the imaging in Figure 1.12 b) was performed with a negatively charged tip, resulting in the dark zig-zag rows likely being composed of Fe atoms. This represents an inverted contrast compared to the STM images. [72]

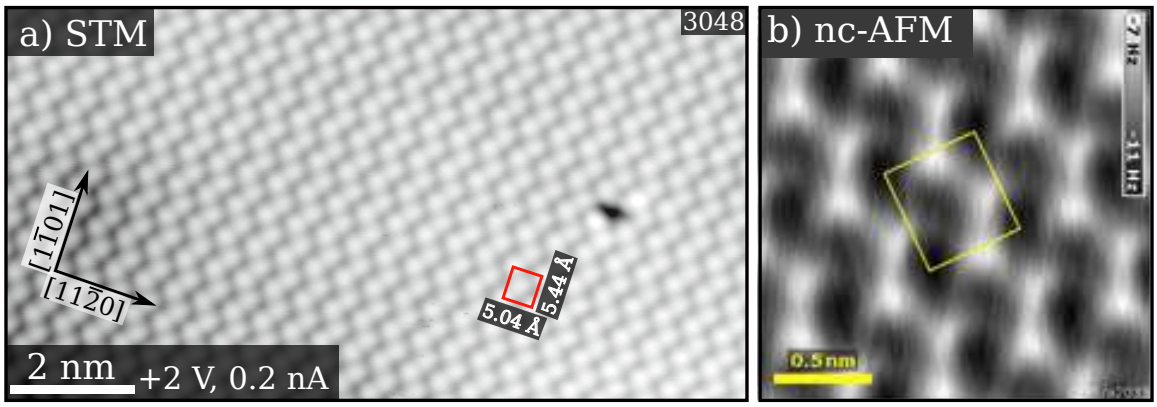

Figure 1.12: Scanning probe images of the bulk truncated α-$Fe_2O_3(1\bar{1}02)$ surface. a) shows a RT-STM image in empty state mode. Bright zig-zag rows running along the $[\bar{1}101]$ direction are believed to be attributed to surface Fe atoms. The surface unit cell is show with a red rectangle. The nc-AFM image in b) shows an inverted contrast; here the dark zig-zag rows are attributed to surface Fe atoms. b) is adapted from [72]

STM imaging is possible after the hematite sample is prepared by several (60-100) cycles of sputtering for 10 min (with 1 keV Ar^+ ions) and annealing in UHV. This process reduces the sample by removing O, which creates O vacancies in the crystal lattice and therefore the conductivity is increased. Another approach to obtain conductive hematite samples, which enable STM imaging, is to grow single-crystalline, atomically flat Ti-doped α-$Fe_2O_3(1\bar{1}02)$ films by pulsed laser deposition (PLD). This approach has the advantage of producing conductive samples with large, clean terraces. [92] Such a sample was utilized in this thesis.

The interaction of the bulk-truncated $Fe_2O_3(1\bar{1}02)$ surface with water is particularly relevant, as this thesis investigates the influence of water on Rh adatoms supported on α-$Fe_2O_3(1\bar{1}02)$.

TPD experiments reveal a major desorption peak at 345 K, saturating at 1.27 molecules/unit cell, and a second peak at 250 K at higher coverages. This corresponds to a total saturation coverage of $\approx$2 H_2O/unit cell for the first monolayer [93, 94], which aligns

Die approbierte gedruckte Originalversion dieser Dissertation ist an der TU Wien Bibliothek verfügbar.
The approved original version of this doctoral thesis is available in print at TU Wien Bibliothek.
TU Bibliothek Your knowledge hub WIEN

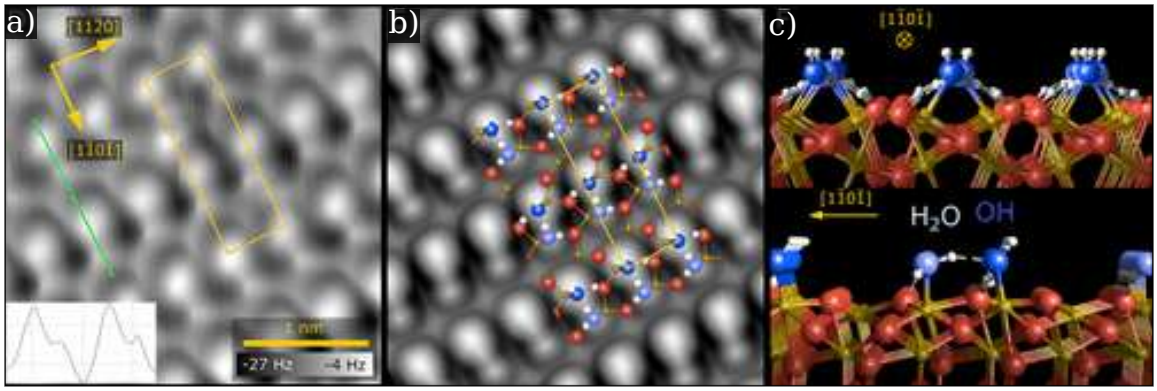

Figure 1.13: Partially dissociated water dimers at the water-hematite interface. a) shows a nc-AFM image of the surface at a saturation of 1.27 water molecules/unit cell. A (1 × 3) phase of adsorbed water is imaged at 4 K using a CO terminated tip. The green line profile indicates the four maxima corresponding to two dimer species. b) shows a simulated nc-AFM image and c) the minimum-energy structure derived by DFT+U based calculations of the low coverage phase. OH and water bind to undercoordinated Fe cations (brown), with one $O_{lattice}H$ formed at a surface O (red). The O atoms of the intact and dissociated water molecules are shown in light and dark blue, respectively. Adapted from [93]

well with the symmetry of the (1 × 1) unit cell where two undercoordinated Fe^{3+} cations can bind water molecules. Most importantly, water dissociates on the surface at room temperature, adsorbing in the form of half-dissociated water dimers, where water molecules and OH groups are coordinated to surface Fe atoms, leaving every third surface Fe atom unoccupied (see Figure 1.13)

To determine the surface stability in liquid water, the sample was exposed to ultrapure water, using a setup described in [95, 96]. LEED patterns and XPS spectra remained indistinguishable from high water doses under UHV conditions, suggesting that the surface is unaffected by liquid water. [93] Thus, the α-$Fe_2O_3(1\bar{1}02)$ surface is a promising candidate for studying model SAC under realistic conditions.

Die approbierte gedruckte Originalversion dieser Dissertation ist an der TU Wien Bibliothek verfügbar.
The approved original version of this doctoral thesis is available in print at TU Wien Bibliothek.
TU Bibliothek Your knowledge hub WIEN

1.5.3 Magnetite

Magnetite belongs to the mineral group known as inverse spinels and crystallize in the cubic system. The general chemical formula of a spinel is $A^{2+}B_2^{3+}X_4^{2-}$. In this structure, the X ions (anions) are arranged in a face-centred close-packed lattice, while the A and B ions (cations) occupy 1/8 of the tetrahedral and 1/2 of the octahedral sites. The distinction between spinels and inverse spinels arises from the occupation of A^{2+} and B^{3+} cations in octahedral and tetrahedral sites. In the case of magnetite, O acts as the X ion and A and B represent Fe atoms, either in tetrahedral sites (Fe_{tet}) or octahedral sites (Fe_{oct}). Fe^{2+} occupy half of the octahedral sites, while Fe^{3+} occupies the other half as well as all tetrahedral sites. (see Figure 1.14)

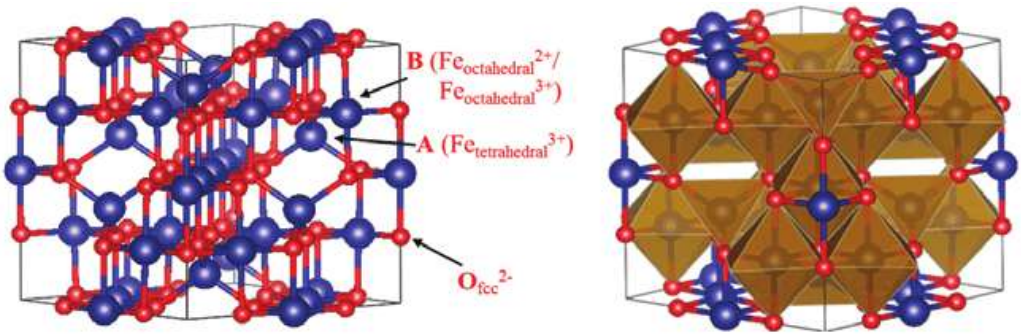

Figure 1.14: Schematic model of the inverse spinel crystal structure of magnetite. Fe atoms are indicated in blue, O atoms in red. a) shows a ball and stick model and b) a polyhedral model of the cubic unit cell. Reprinted from [97]

Due to the occupancy of octahedral sites by both Fe^{2+} and Fe^{3+}, electron transfer between these two oxidation states is facile above 120 K, resulting in electrical conductivity at room temperature. However, at 120 K, a phase transition from cubic to monoclinic occurs, leading to a drop in conductivity by two orders of magnitude—this is known as the Verwey transition. [98]
Magnetite is magnetic at room temperature, as its name already implies. It was used as a prototype to explain the properties of ferrimagnetism, where the magnetic moment arises solely from Fe^{2+} cations, since Fe^{3+} cations in the tetrahedral (A) and octahedral (B) sublattice are antiferromagnetically coupled and cancel each other

Die approbierte gedruckte Originalversion dieser Dissertation ist an der TU Wien Bibliothek verfügbar.
The approved original version of this doctoral thesis is available in print at TU Wien Bibliothek.
TU Bibliothek Your knowledge hub WIEN

out. [99]
Natural magnetite single crystals are commonly octahedrons, exhibiting {111} facets, though the {001} facet is also frequently observed. [100] DFT calculations suggest that the surface energy of the {001} facet is lower than that of the {111} facet. However, some studies suggest otherwise. [101, 102] The {110} facet has been frequently reported in natural crystals; however, recent studies have shown that it undergoes reconstruction, leading to the formation of {111} nanofacets. [103] Both the $Fe_3O_4(001)$ and the (111) surface have been extensively studied in surface science. [104–111] The Pendry R-factors determined from LEED *I(V)* for the assumed structures is about 0.1 for both surfaces. [104, 107]
In this thesis the $Fe_3O_4(001)$ surface has been used as a support material for SAC.

1.5.4 The $Fe_3O_4(001)$ surface

Along the (001) direction, magnetite is composed of alternating layers of Fe_{tet} and $(Fe_{oct})_2O_4$. The $Fe_3O_4(001)$ surface is terminated by the $(Fe_{oct})_2O_4$ layer. Due to the spinel structure, two neighbouring layers are always rotated by 90°. DFT+U based calculations indicate that pairs of surface Fe_{oct} atoms are relaxed in opposite direction, perpendicular to the row [112–114], resulting in a $(\sqrt{2} \times \sqrt{2})R45°$ surface reconstruction, known as the distorted bulk truncation (DBT) model. This structure was supported by STM images, where undulating rows of Fe_{oct} can be observed. [115, 116]. LEED *I(V)* [114] and surface x-ray diffraction (SXRD) measurements [112] confirmed this reconstruction, which made this model widely accepted. However, despite general acceptance, the model shows poor agreement of theoretical and experimental LEED *I(V)* curves. Moreover, it fails to account for the stability of single metal atoms adsorbed at room temperature, which selectively occupy only one of the two possible adsorption sites within the $(\sqrt{2} \times \sqrt{2})R45°$ unit cell. [117] Furthermore, it does not explain the facile incorporation of transition metals into the surface at relatively mild annealing temperatures. [118, 119].
In 2014, a study by Bliem et al. offered a solution to these unresolved issues by introducing the subsurface cation vacancy (SVC) structure. According to this model, the $(\sqrt{2} \times \sqrt{2})R45°$ periodicity arises from the replacement of two Fe_{oct} atoms from the third layer with an interstitial Fe atom (Fe_{int}), tetrahedrally coordinated to the second layer. Overall, one cation in removed per $(\sqrt{2} \times \sqrt{2})R45°$ unit cell. This

Die approbierte gedruckte Originalversion dieser Dissertation ist an der TU Wien Bibliothek verfügbar.
The approved original version of this doctoral thesis is available in print at TU Wien Bibliothek.
TU Bibliothek Your knowledge hub WIEN

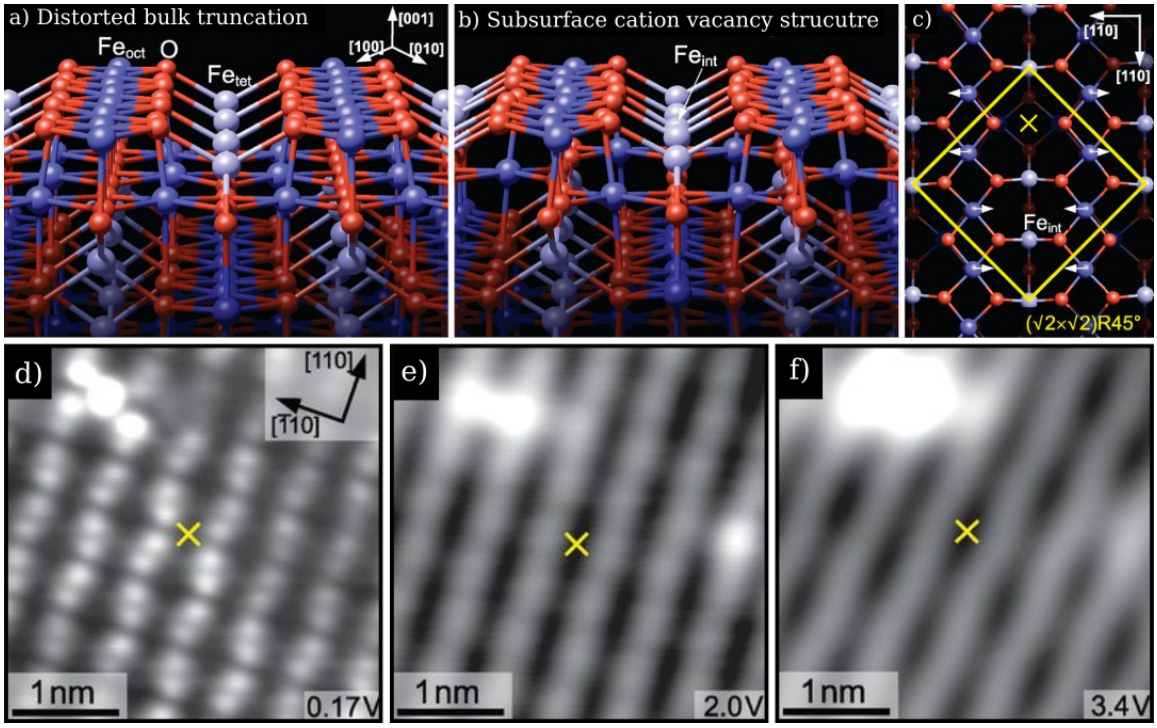

Figure 1.15: The top panel shows surface structure models of $Fe_3O_4(001)$: a) shows the distorted bulk truncation and b) the subsurface cation vacancy structure. c) shows the $(\sqrt{2} \times \sqrt{2})R45°$ unit cell. "×" indicates the so-called narrow site, where metal adatom adsorption is possible. In the lower panel, STM images of the same area demonstrate that the undulation of the Fe_{oct} rows can be reversed by varying the sample bias. Adapted from [104]

subsurface reorganization is responsible for the undulations observed in the Fe_{oct} rows. DFT+U based calculations and spectroscopic data confirm that all cations in the four outermost layers exhibit Fe^{3+} character, meaning the surface is oxidised compared to the bulk. From a thermodynamic perspective, this oxidation is consistent with Fe_2O_3 being the favoured phase under the employed temperature and pressure conditions. Also LEED *I(V)* measurements provide better agreement with this model than with the previous ones. [104]

Figure 1.15 clearly illustrates that the undulation of the Fe_{oct} rows is more distinct in the SCV model (b) than in the DBT model (a). The SCV model also explains

Die approbierte gedruckte Originalversion dieser Dissertation ist an der TU Wien Bibliothek verfügbar.
The approved original version of this doctoral thesis is available in print at TU Wien Bibliothek.
TU Bibliothek Your knowledge hub WIEN

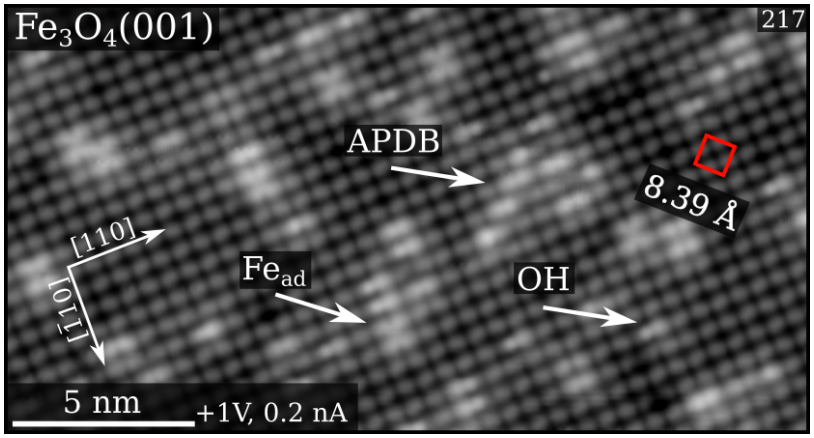

Figure 1.16: RT-STM image of the as-prepared $Fe_3O_4(001)$ surface. Common defects are marked with an arrow. The $(\sqrt{2} \times \sqrt{2})R45°$ unit cell is indicated with a red square.

why metal adatoms consistently occupy only one of the two possible adsorption sites per $(\sqrt{2} \times \sqrt{2})R45°$ unit cell, as Fe_{int} block one of the adsorption sites. In contrast, both sites are equivalent in the DBT model. In Figure 1.15 c), a top view of the unit cell shows "×" marking the only possible adsorption site for metal adatoms. Figure 1.15 d)–f) presents three empty-state STM images, at the same area taken with different sample bias. The undulations in the Fe_{oct} rows are most distinct at 0.17 V sample bias and almost disappear at 2 V sample biases. The undulations reappear inverted at 3.4 V sample bias. This effect can be attributed to the splitting of the surface Fe_{oct} d-states by the crystal field. At a low sample bias of 0.17 eV, electrons can tunnel into a tilted t_{2g} orbital, which is asymmetrically positioned above the atom core. At 3.4 eV, electrons tunnel into the symmetric d_{x^2} and $d_{x^2-y^2}$ e_g orbitals, which better reflect the true surface relaxation. [104] The "×" position is denoted as narrow site and the position next to it (where the Fe_{int} is present in the subsurface) as wide side.

Figure 1.16 shows a typical STM image of the as-prepared $Fe_3O_4(001)$ surface. Since the surface has been extensively studied, commonly occurring defects such as surface hydroxyls (OH) [120], antiphase domain boundaries (APDBs) [121] and iron adatoms (Fe_{ad}) [122] are well understood. The $(\sqrt{2} \times \sqrt{2})R45°$ unit cell, indicated with a red square, has a side length of 8.39 Å.

The SCV surface reconstruction is stable over a wide range of chemical potential.

Die approbierte gedruckte Originalversion dieser Dissertation ist an der TU Wien Bibliothek verfügbar.
The approved original version of this doctoral thesis is available in print at TU Wien Bibliothek.
TU Bibliothek Your knowledge hub WIEN

However, in the presence of liquid water, the reconstruction is lifted by hydroxylation of the surface, resulting in the growth of a Fe(OH) phase. [123]
Even though the surface reconstruction is not stable under realistic conditions, it remains an excellent candidate to study model SAC reactions.

Die approbierte gedruckte Originalversion dieser Dissertation ist an der TU Wien Bibliothek verfügbar.
The approved original version of this doctoral thesis is available in print at TU Wien Bibliothek.

2 Methods

2.1 Scanning Tunneling Microscopy (STM)

Scanning Tunneling Microscopy (STM) belongs to the family of Scanning Probe Microscopy (SPM), in which an atomically sharp tip scans a surface to gain information about the surface topology. STM was invented in 1981 [124], and Gerd Binnig and Heinrich Rohrer were awarded the Nobel Prize for it innovation in 1986. [125] Today, STM is one of the most powerful methods for studying surface topology under UHV conditions.

Depending on the SPM technique used, different types of signals are recorded, which in turn are interpreted to determine the surface topology. In STM, a bias (of one mV to a few V) between the sample and the tip is applied to allow quantum tunneling of electrons, which generates a current of a few pA to 10 nA. Two main modes are used in STM imaging: constant-height mode and constant-current mode, where the tunneling current is either used as the measurement signal or as part of the feedback mechanism. Constant-current mode is most commonly used, allowing the tip to accurately trace the surface topography. The tip is moved by a piezoelectric element, maintaining a surface-tip distance of 0.5–2 nm.

The tunneling process through a potential barrier can be calculated by solving the time-independent Schrödinger´s equation, assuming a rectangular barrier:

$$-\frac{\hbar^2}{2m}\nabla^2\psi(\mathbf{r}) + V(\mathbf{r})\psi(\mathbf{r}) = E\psi(\mathbf{r}) \tag{2.1}$$

where $\hbar$ is the reduced Planck constant, ∇^2 is the Laplacian operator, $V(\mathbf{r})$ represents the rectangular potential barrier, and E represents the particle's energy. The solution to the Schrödinger equation within the barrier region is an exponentially decaying wave, expressed as $e^{-\kappa z}$, where $\kappa = \sqrt{\frac{2m\Phi}{\hbar^2}}$ and z is the coordinate. In simplified terms, the probability amplitude of the decaying wave is proportional to $|\psi(\mathbf{d})|^2$,

Die approbierte gedruckte Originalversion dieser Dissertation ist an der TU Wien Bibliothek verfügbar.
The approved original version of this doctoral thesis is available in print at TU Wien Bibliothek.
TU Bibliothek Your knowledge hub WIEN

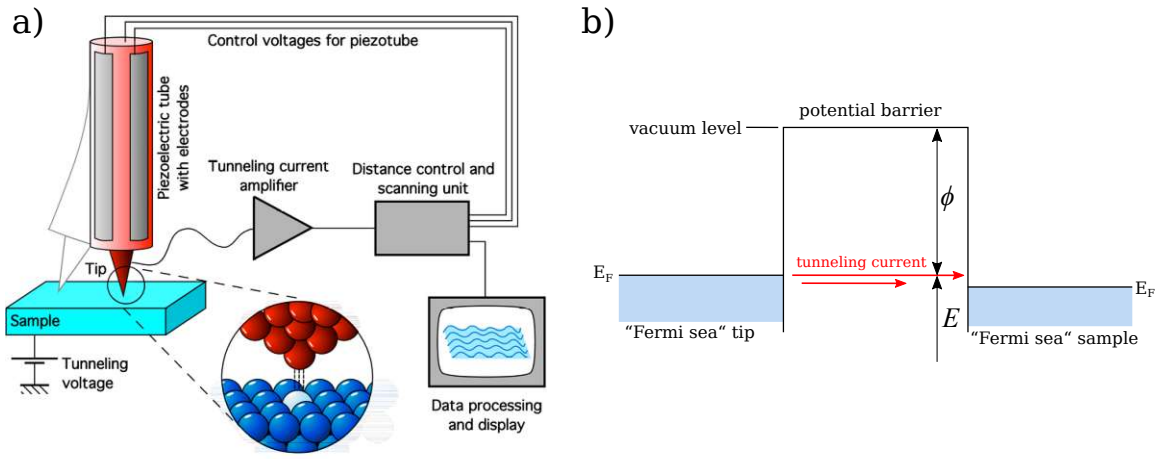

Figure 2.1: In a), a schematic model of the STM setup is shown, while in b), a simplified model illustrates the tunneling process. Tunneling occurs from the Fermi sea of the tip to the Fermi sea of the sample, driven by the higher Fermi level of the tip. The electrical current flows from occupied states in the tip to unoccupied states in the sample. Image a) has been provided by Michael Schmid.

which implies proportionality to $e^{-2\kappa z}$. Thus, the current I is proportional to $e^{-2\kappa d}$, where d is the width of the barrier—in the case of STM, the distance between tip and sample. This relationship implies that even a small change in the tip-sample distance by one Å, causes the current to change by a factor of 5–10, hence, highlighting the tunneling current's high sensitivity to the tip-sample distance.

A more sophisticated model, known as the Tersoff-Hamann model, was later developed to provide a more accurate description. This model considers a spherically symmetric tip and accounts for the local density of states (LDOS) of the surface. [126] The tunneling current in this model is proportional to the LDOS near the Fermi edge (since only small biases are typically used) as well as proportional to the applied bias voltage. Additionally, it incorporates a 3D perspective, hence, in constant-current mode, the center of the spherical tip follows contours of constant LDOS on the surface. This means that STM images do not depict the actual surface geometry or atomic positions but rather the electronic structure. Consequently, features that have a higher apparent height than others do not necessarily protrude further from the surface; they may simply have more unoccupied states in the range

Die approbierte gedruckte Originalversion dieser Dissertation ist an der TU Wien Bibliothek verfügbar.
The approved original version of this doctoral thesis is available in print at TU Wien Bibliothek.

of the applied bias. Hence, the images have to be interpreted carefully.

2.2 Noncontact Atomic Force Microscopy (nc-AFM)

Atomic Force Microscopy (AFM), like STM, belongs to the family of SPM techniques. In AFM, the measurement signal is derived from the forces between the tip and the sample, enabling imaging on insulators—a significant advantage. Typically, the tip is in contact with the surface, reducing the influence of the experimental environment and making AFM versatile and suitable for measurements in various conditions, including air or liquids. However, the resolution does not reach atomic level. In noncontact (nc-)AFM, the tip is mounted on an oscillating catilever and does not touch the surface. The resonance frequency of the cantilever shifts in response to short-range forces between the tip and the surface. By measuring this frequency shift, the surface topology can be imaged. To prevent the tip from making contact with the surface due to long-range forces, and thereby damaging the tip, the catilever must have high stiffness.

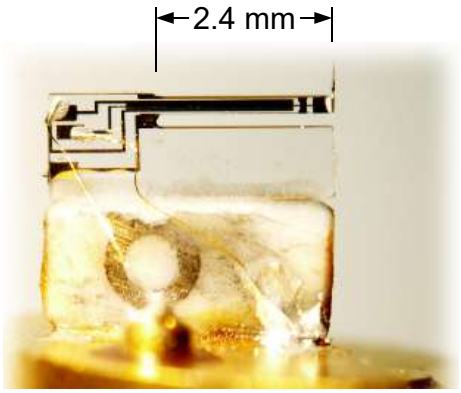

Figure 2.2: Image of a qPlus sensor. The arm of the tuning fork measures 2.4 mm, with the tip positioned on the right side, facing upwards. The signal is recorded by electrodes on the quartz crystal, visible on the left side of the sensor. Photo provided by Martin Setvin.

The widely used qPlus sensor meets these requirements with its quartz-based tuning fork design. Invented by F. Giessible, it surpasses STM in terms of image resolution.

Die approbierte gedruckte Originalversion dieser Dissertation ist an der TU Wien Bibliothek verfügbar.
The approved original version of this doctoral thesis is available in print at TU Wien Bibliothek.
TU Bibliothek Your knowledge hub WIEN

[127] An image of the sensor is shown in Figure 2.2. The cantilever vibrates with a frequency of ≈30–80 kHz, and the frequency change observed is typically ≈3–30 Hz. The imaging contrast in nc-AFM is highly sensitive to the atoms at the tip apex. Therefore, functionalizing the tip with a known atom or molecule is beneficial for achieving reproducible, high-resolution images. A well-established approach is to functionalize the tip with CO, which is chemically stable and has highly localized Pauli repulsion, allowing even for the resolution of small organic molecules. [89]. In this thesis, a CO-terminated tip was used, created by picking up a CO molecule from a Cu surface pre-dosed with CO. To obtain high-resolution images, sample temperatures of 78 K (cooled by liquid N_2) or 4 K (cooled by liquid He) are generally used, along with constant-height mode.

2.3 X-Ray Photoelectron Spectroscopy (XPS)

X-ray Photoelectron Spectroscopy (XPS) is a powerful surface-sensitive technique used to analyse both the elemental composition of a surface as well as the chemical state of the elements present. The technique is based on the photoelectric effect (see Figure 2.3). Electrons are ejected from the core level after receiving energy from incoming photons, which must have an energy greater than the material's work function and the binding energy of the electrons being removed. An X-ray source emits monoenergetic X-rays to irradiate the sample, commonly using Mg Kα and Al Kα radiation. The detected signal is the kinetic energy of the emitted electron, which is described by the equation:

$$E_{\text{kin}} = h\nu - E_B - \Phi_{Analyser} \tag{2.2}$$

where $h\nu$ is the energy of the incoming photon, E_B is the initial binding energy of the emitted electron, and $\Phi_{Analyser}$ is the work function of the analyser. Since both the energy of the incoming photon and the analyser's work function is known, the initial binding energy of the emitted electrons can be calculated.
Each element has a characteristic core-level energy, resulting in distinctive peaks in the XPS spectrum, enabling precise elemental identification. Chemical shifts of the peaks in binding energy can reveal additional details about the oxidation states, bonding environments, and electronic structures of the elements present.

Die approbierte gedruckte Originalversion dieser Dissertation ist an der TU Wien Bibliothek verfügbar.
The approved original version of this doctoral thesis is available in print at TU Wien Bibliothek.
TU Bibliothek Your knowledge hub WIEN

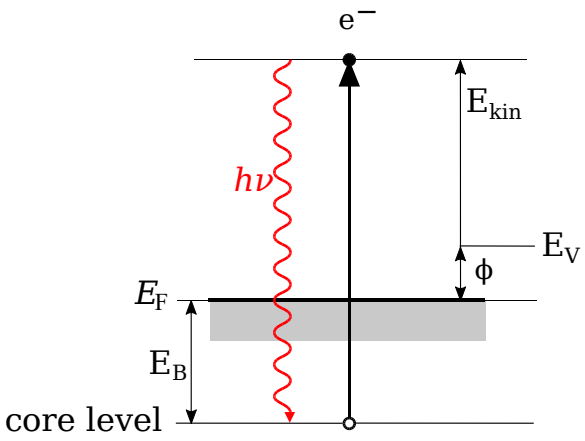

Figure 2.3: Schematic of the photoelectric effect. An electron is emitted from the core level if an incoming photon has an energy greater than the material's work function and the electron's binding energy.

XPS is highly surface-sensitive, typically detecting electrons originating close to the surface, even though the X-rays themselves penetrate several μm into the sample. This sensitivity can be explained by the inelastic mean free path (IMFP) of electrons in solids. XPS utilizes relatively low kinetic energy electrons (typically $\approx$1 keV), resulting in an IMFP of only a few nm. Electrons that undergo inelastic scattering loose some of their original energy, making them unsuitable for precise binding energy analysis. Consequently, only electrons originating within the first few nm of the surface reach the detector without significant energy loss. Additionally, the surface sensitivity can be further enhanced by tilting the sample away from the surface normal. At shallow angles, the signal is dominated by electrons from just the topmost surface layers.

2.4 Low Energy Electron Diffraction (LEED)

Low Energy Electron Diffraction (LEED) is a technique used to analyse the surface structure of single-crystalline surfaces. By bombarding the surface with a beam of low-energy electrons (typically 20–200 eV), a diffraction pattern forms due to scattering of the electron beam by the ordered lattice, which can be observed on a hemispherical fluorescent screen. Similar to XPS, LEED is highly surface sensitive, due to

Die approbierte gedruckte Originalversion dieser Dissertation ist an der TU Wien Bibliothek verfügbar.
The approved original version of this doctoral thesis is available in print at TU Wien Bibliothek.

the IMPF of electrons in solids. Qualitative analysis of the diffraction spots provides information about the periodicity and symmetry of the surface atoms.
Additionally, quantitative structural information can be obtained by varying the electron energy and studying the intensity of diffraction spots as a function of electron energy. The resulting *I(V)* curves, are characteristic of the surface structure and can be compared with surface structure models. This technique is known as LEED *I(V)*.

2.5 Temperature Programmed Desorption (TPD)

Temperature Programmed Desorption (TPD) is a technique used to analyse the interaction of molecules with a surface at specific temperatures and molecular coverages. Through TPD, desorption energies and mechanisms can be determined.
In the utilized TPD setup, the sample is first cooled down to low temperatures before molecules are dosed onto the sample using a calibrated molecular beam directing at a well-defined area. [128] The sample is then heated at a constant rate, while the desorbing molecules (or fractions of molecules) are detected by a Quadrupole Mass Spectrometer (QMS).
The desorption rate is described by the Polanyi-Wigner equation:

$$-\frac{d\theta}{dt} = \nu\theta^n e^{-\frac{E_d}{k_B T}} \tag{2.3}$$

where θ is the coverage, $-\frac{d\theta}{dt}$ is the desorption rate, ν the pre-exponential factor, n is the desorption order, E_d the desorption energy, k_B is the Boltzmann constant, and T is the temperature. To determine E_d, the prefactor ν must be known; however, this value is often difficult to ascertain. It depends on both the temperature and on the entropy difference between the adsorbed state and transition state. While ν is sometimes approximated as a constant value of $10^{13}s^{-1}$, this is not always accurate. It can be determined for a given molecule from transition theory or directly from the TPD data using techniques like inversion analysis [129], although these methods can be complex. For the studies in this thesis, a relatively new approach to determine the desorption energy, based on equilibrium thermodynamics, as described in ref [130], was employed.
The peak shape of a TPD spectrum provides valuable insights into the coverage dependence of the desorption rate. This dependence is described by the desorption

Die approbierte gedruckte Originalversion dieser Dissertation ist an der TU Wien Bibliothek verfügbar.
The approved original version of this doctoral thesis is available in print at TU Wien Bibliothek.
TU Bibliothek Your knowledge hub WIEN

order n, which in surface science is mostly relevant for $n = 0$, 1, or 2. Zero-order desorption usually represents desorption from multilayers, resulting in an exponential dependence on temperature and a sharp signal drop once all species have desorbed. First-order desorption is commonly observed for molecularly bound species, resulting in a desorption peak with a fixed maximum, regardless of the initial coverages. In contrast, second-order desorption shows a peak maximum that decreases in temperature with increasing coverage due to dissociatively adsorbed molecules, which must recombine before desorption can occur.

2.6 Density Functional Theory (DFT)

Several experimental studies of this thesis were supported by Density Functional Theory (DFT) calculations, which were conducted by Panukorn Sombut. DFT is a quantum mechanical modelling method used to determine the ground-state electron density of many-electron systems by solving the Schrödinger equation approximately. DFT is widely applied in fields like material science, chemistry, and physics to study properties such as reaction mechanisms, adsorption behaviour, and material stability. The calculations were performed using the Vienna ab initio simulation package (VASP). [131] Further details on the calculations are provided in the published works referenced in [132–134].

2.7 Experimental setup and sample preparation

The following section describes the experimental chambers used for this thesis, as well as the commonly used procedures for sample preparation.
I conducted experiments in the Low-Temperature STM/nc-AFM chamber and the Room-Temperature STM chamber, while data from the TPD chamber were acquired and analysed by Chunlei Wang.

2.7.1 Low-Temperature STM/nc-AFM chamber

The LT-STM/nc-AFM UHV chamber consists of two compartments: a preparation chamber ($p < 1 \cdot 10^{-10}$ mbar) and an analysis chamber ($p < 2 \cdot 10^{-11}$ mbar).

Die approbierte gedruckte Originalversion dieser Dissertation ist an der TU Wien Bibliothek verfügbar.
The approved original version of this doctoral thesis is available in print at TU Wien Bibliothek.
TU Bibliothek Your knowledge hub WIEN

The preparation chamber is equipped with a commercial XPS, which includes a X-ray source with anodes for nonmonochromatic Mg Kα and Al Kα radiation and a SPECS Phoibos 100 hemispherical analyser. Additional equipment includes a commercial LEED setup, a single-pocket electron beam evaporator (Focus EFM 3), a triple-pocket electron beam evaporator (Focus EFM 3T) and a temperature-stabilized quartz-crystal microbalance to calibrate the deposition rate of the evaporated metals. For sample preparation, the chamber is also equipped with a scanning ion source and an electron beam heating stage. Resistive heating and liquid N_2 cooling, can be performed at the manipulator.
The analysis chamber is equipped with an Omicron LT-STM, featuring a Qplus sensor with an electrochemically etched W tip and an in-vacuum preamplifier [135] inside a cryostat. This setup is typically cooled with liquid N_2, resulting in a sample temperature of 78 K, but can also be cooled with liquid He to reach a sample temperature of 4 K. Both chambers are further equipped with mass spectrometers to analyse the residual gas and with leak-valves for precise gas dosing.

2.7.2 Room-Temperature STM chamber

The RT-STM chamber also consists of two compartments: a preparation chamber ($p < 1 \cdot 10^{-10}$ mbar) and an analysis chamber ($p < 2 \cdot 10^{-11}$ mbar).
The preparation chamber is equipped with a single-pocket electron beam evaporator (Focus EFM 3), a triple-pocket electron beam evaporator (Focus EFM 3T) and a temperature-stabilized quartz-crystal microbalance to calibrate the deposition rate of the evaporated metals. For sample preparation, the chamber is also equipped with a scanning ion source. Electron beam heating can be conducted on the transfer rod.
The analysis chamber is equipped with a commercial XPS, which includes an X-ray source with anodes for nonmonochromatic Al Kα radiation and a SPECS Phoibos 100 hemispherical analyser as well as a commercial LEED set-up. Imaging is performed by an Omicron µ-STM with an electrochemically etched W tip. Both chambers are further equipped with mass spectrometers to analyse the residual gas and with leak-valves for precise gas dosing.

Die approbierte gedruckte Originalversion dieser Dissertation ist an der TU Wien Bibliothek verfügbar.
The approved original version of this doctoral thesis is available in print at TU Wien Bibliothek.
TU Bibliothek Your knowledge hub WIEN

2.7.3 TPD chamber

The TPD chamber was in-house designed specifically for reactivity studies on single-crystalline oxide surfaces and has a base pressure $< 7 \cdot 10^{-11}$ mbar. It is equipped with a flow cryostat cooled by liquid He (Janis ST-400), which allows for a sample temperature below 50 K. Gases are dosed directly at the sample surface using an effusive molecular beam source, leading to a beam spot of ≈3.5 mm containing 99.9% of the dosed molecules. During a heating ramp controlled by a PID control loop, desorbing molecules are analysed by a quadrupole mass spectrometer (Hiden 3F PIC), with the sample positioned directly in front of it. To prevent electrons from the QMS reaching the surface, the sample is biased by −85 V.
Heating is achieved via direct current, with temperature measurements taken from the sample plate using a K-type thermocouple. The chamber is further equipped with a single-pocket e-beam evaporator (FOCUS EFM 3), a triple-pocket e-beam evaporator (FOCUS EFM 3T), a temperature-stabilized quartz-crystal microbalance, several leak-valves and a scanning ion source. For additional surface analysis, a SPECS XR50M X-ray source with a monochromator, a SPECS UVS 10/35 UV source, and a SPECS Phoibos 150 hemispherical analyser are also installed on the chamber. Further details can be found in ref [128, 136, 137] Recently, the chamber has been further equipped with an in-house designed Infrared Reflection Absorption Spectroscopy (IRAS) with angle selection. [138]

2.7.4 Sample preparation

For Fe_2O_3, Fe_3O_4 and anatase TiO_2 natural single crystals were used, while for rutile TiO_2, synthetic single crystals were used. The samples, purchased cut and polished from SurfaceNet GmbH or Crystec, were cleaned in an ultrasonic bath, mounted onto a Ta plate with a gold foil placed between the plate and the sample for a better thermal contact, and then loaded into the UHV chambers. After outgassing, by gradually increasing the temperature, the surfaces were cleaned by sputtering (1 keV Ar^+ or Ne^+) and annealing cycles. Further details on the preparation of each metal oxide surface can be found in chapter 1. The samples were characterised by an XPS survey spectra, to assess cleanliness and by LEED to confirm that each surface displayed its characteristic LEED spots. In the imaging chambers, the as-prepared surfaces were characterised using STM and/or nc-AFM.

Die approbierte gedruckte Originalversion dieser Dissertation ist an der TU Wien Bibliothek verfügbar.
The approved original version of this doctoral thesis is available in print at TU Wien Bibliothek.
TU Bibliothek Your knowledge hub WIEN

3 Adatom stabilization with and without the influence of co-adsorbed water on TiO_2

In this chapter, the stability of various transition metal atoms deposited onto rutile TiO_2(110) and anatase TiO_2(101), both in the presence and absence of co-adsorbed water, has been investigated. The results for the rutile TiO_2(110) surface have been publisehd in ref. [132], and the results for the anatase TiO_2(101) surface have been published in ref. [139]. DFT+U calculations were performed by Panukorn Sombut.

3.1 Introduction

Model SAC on rutile TiO_2(110)

In surface science, the rutile TiO_2(110) facet has been extensively studied as a support material for SAC. [140] A key characteristic of the r-TiO_2(110) surface is the presence of $V_{O_{2c}}$ sites (closely described in section 1.4.1), which can act as active sites for chemical reactions, as adsorption sites for metal adatoms, and as nucleation sites for metal nanoparticles. [38, 39]

Single, immobile Au adatoms can be observed after depositing a very low coverage of Au in UHV. Au adatoms preferentially bind to $V_{O_{2c}}$ sites on the r-TiO_2(110) surface. [141] At higher coverages, Au clusters nucleate at the same sites. [142] DFT+U-based calculations confirm this structure and show that Au_1 at $V_{O_{2c}}$ sites become negatively charged, with an oxidation state of Au^-. [132] Pt similarly forms immobile adatoms in very low concentrations at $V_{O_{2c}}$ sites. Adsorption was only observed at 80 K, with no stability analysis performed for Pt_1 species at higher temperatures. When exposed to CO, Pt adatoms adsorb CO molecules, with the CO molecule leaning towards a

Die approbierte gedruckte Originalversion dieser Dissertation ist an der TU Wien Bibliothek verfügbar.
The approved original version of this doctoral thesis is available in print at TU Wien Bibliothek.

surface Ti atom of the support. [143]
In contrast, Ag and Cu immediately form clusters after evaporation at room temperature. [144, 145] This behaviour is likely due to differences in electronegativity. More electronegative metals, such as Au and Pt, can accept extra charge from $V_{O_{2c}}$ sites, forming stronger bonds at these particular sites.
Ni was found to form 3D clusters on the terraces, even at very low coverages [146], while Pd appears to form dimers. [147].
A study by Dong et al. investigated the photochemical properties of the $Au_1/TiO_2(110)$ system. They observed that at 80 K, after $V_{O_{2c}}$ saturation, Au adatoms also occupy Ti_{5c} sites. Notably, localized metal-induced gap states below E_F, measured via STM, provided a pathway for transferring photoexcited holes from the TiO_2 substrate to adsorbed Au atoms. When UV light (or the influence of the tip) was introduced, hole transfer could be achieved, resulting in weakening of the Au-Ti_{5c} bond, enabling Au adatoms to diffuse across the surface. [148]
A combined experimental and theoretical study on rutile TiO_2 nanoparticles suggest that Rh atoms substitute Ti_{6c} sites under oxidising conditions, while under reducing conditions, Rh adatoms adsorb atop an in-plane O atom coordinated to Ti and O atoms from the surface in reducing conditions. [149]

Model SAC on anatase TiO_2(101)

Relatively little research has been conducted on the adsorption of metals on the anatase $TiO_2(101)$ surface. However, a study by Gong et al. examined the interaction of Au and Pt with this surface. Using STM, they demonstrated that both systems undergo sintering at room temperature, even at low metal coverage, resulting in the formation of nanoparticles on the surface. Computational results revealed that Au adatoms are most stable above Ti_{5c} sites. However, the interaction with the surface is weak (0.25 eV), leading to the formation of large nanoparticles that preferentially adsorb at step edges. Pt, on the other hand, forms clusters on both terraces and step edges. Additionally, adatom-like protrusions were observed after Pt deposition, positioned above O_{2c} sites. However, this location does not align with the computationally predicted adsorption site for Pt adatoms, which is between two O_{2c} sites, near to two Ti_{5c} and two Ti_{6c} surface atoms. [150]

Die approbierte gedruckte Originalversion dieser Dissertation ist an der TU Wien Bibliothek verfügbar.
The approved original version of this doctoral thesis is available in print at TU Wien Bibliothek.

The influence of water

In surface science, model SAC systems are often analysed under UHV conditions. To create a more realistic model one can selectively introduce molecules that might affect the stability of the system and determine their individual impact unambiguously. Previous studies have demonstrated that, for example, water can significantly influence catalytic mechanisms. [151, 152] For systems ultimately utilized in an aqueous environment, water is an obvious candidate for such investigations.

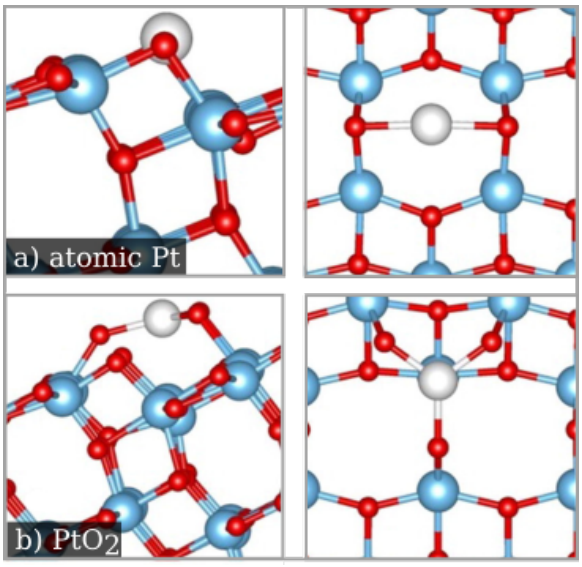

Figure 3.1: DFT+U calculation of a Pt atom adsorbed on the anatase TiO_2(101) surface. a) shows an isolated Pt atom and b) a PtO_2 species. The structure in the lower panel (b) has been shown to be significantly more stable than the structure in the top panel (a). Adapted from [153].

A key motivation factor for the experiments in this section was a recent study by DeRita et al. [154], which demonstrated that thermally stable catalysts consisting of single Pt atoms on 5 nm particles of anatase TiO_2 can be synthesized. By depositing one Pt atom per support particle, this approach effectively overcomes sintering of the precious metal atoms. The study further revealed that the isolated Pt_1 species exhibit a turnover frequency for CO oxidation that is twice as high as that of a catalyst consisting of a 1 nm Pt cluster on the same support material. A follow-up study [153] elucidated the atomic structure of the isolated Pt_1 species on the anatase TiO_2, proposing that the Pt atoms are bound to two excess O atoms (PtO_2) derived from

Die approbierte gedruckte Originalversion dieser Dissertation ist an der TU Wien Bibliothek verfügbar.
The approved original version of this doctoral thesis is available in print at TU Wien Bibliothek.
TU Bibliothek Your knowledge hub WIEN

surface hydroxyl groups. These hydroxyl groups serve as an anchor to the oxide support. Figure 3.1 depicts a DFT+U-calculated model of a Pt atom and a PtO_2 species adsorbed on the anatase $TiO_2(101)$ surface. The PtO_2 species is coordinated to three O atoms—two originating from former hydroxyl groups on the surface and one from the oxide lattice. This configuration renders the structure significantly more stable than that of an isolated Pt atom adsorbed on the same surface. This finding clearly demonstrated that adding ligands can enhance the stability of metal atoms on the anatase $TiO_2(101)$ surface.
In contrast, a surface science study comparing the nucleation of Au and Ag nanoparticles on reduced, hydroxylated and oxidised rutile $TiO_2(110)$ surfaces has found that the presence of surface hydroxyls accelerates the sintering of deposited metal atoms. [155, 156]
This highlights that the stabilization of metal adatoms strongly depends on the metal-support interactions, making it uncertain whether the same approach will stabilize different transition metals on varying metal oxide support materials. Using the surface science approach, we can create models of existing powder catalysts and evaluate the validity of computationally derived models.

To examine how the stability of various transition metals on single-crystalline TiO_2 surfaces is influenced by co-adsorbed water and to identify potential trends, we conducted a screening study of different transition metals on two distinct TiO_2 surfaces, both with and without the presence of co-adsorbed water. Metal deposition in UHV and with a water vapour background was carried out for Rh and Pt on the rutile $TiO_2(110)$ surface and for Pt, Rh, Ni and Ir on the anatase $TiO_2(101)$ surface.

Die approbierte gedruckte Originalversion dieser Dissertation ist an der TU Wien Bibliothek verfügbar.
The approved original version of this doctoral thesis is available in print at TU Wien Bibliothek.

3.2 Rh and Pt adatoms on rutile TiO_2(110)

Rh on rutile TiO_2(110)

The experiments in this section were carried out at the LT-STM, with imaging performed at 78 K, using liquid nitrogen as a cryogen.

A coverage of 0.04 ML Rh was deposited onto r-TiO_2(110) at 100 K, and the sample was subsequently annealed stepwise to 873 K. Figure 3.2 shows XPS spectra of the Rh 3d region alongside STM images of the temperature series. After Rh deposition at 100 K, STM images reveal atomically dispersed Rh adatoms. Annealing to 150 K leads to the formation of small clusters, which are clearly visible in the STM images. The corresponding XPS spectra show a core-level shift of the Rh 3d peak from 308 eV to a higher binding energy of 308.5 eV (light blue and dark blue curves). This shift is likely due to a final state effect associated with the small size of the Rh clusters. Further annealing results in increasingly larger clusters, observed in the STM images. At approximately 300 K, the Rh 3d peak begins to shift back to lower binding energy, eventually shifting to 307.4 eV at 873 K.

Typical surface defects and adsorbates resulting from surface preparation and residual gas in the preparation chamber are marked with arrows in Figure 3.3 a). $V_{O_{2c}}$ and OH_b are described in section 1.4.1. Features on the Ti^{4+} rows with an apparent height of 90–100 pm relative to the surface, can be attributed to molecular water. [49] Molecular water typically adsorbs below room temperature on the r-TiO_2(110) surface. Given the low sample temperature during Rh deposition, it is not surprising that a few water molecules remain on the surface.

Taking a closer look at the as-deposited Rh at 100 K reveals that the vast majority of Rh is atomically dispersed and occupy the same adsorption site on the r-TiO_2(110) surface: atop Ti^{4+} rows, slightly offset towards the O_{br} row (marked with a circle in Figure 3.3 b) and c)). The slight offset and the apparent height of 140–180 pm clearly distinguish Rh adatoms from molecular water. No interaction between Rh adatoms and $V_{O_{2c}}$ sites is suggested, as the density of $V_{O_{2c}}$ remains unchanged before and after Rh deposition. The experimentally observed adsorption site of Rh adatoms aligns well with DFT+U calculations. Figure 3.3 d) shows the three energetically favoured configurations for Rh adsorption on the r-TiO_2(110) surface. As already observed in the STM images, adsorption of Rh_1 at $V_{O_{2c}}$ sites is not preferred ($E_{ads} = -2.82$ eV, bottom panel). In the most stable configuration ($E_{ads} = -3.24$ eV, top panel) Rh^0

Die approbierte gedruckte Originalversion dieser Dissertation ist an der TU Wien Bibliothek verfügbar.
The approved original version of this doctoral thesis is available in print at TU Wien Bibliothek.
TU Bibliothek Your knowledge hub WIEN

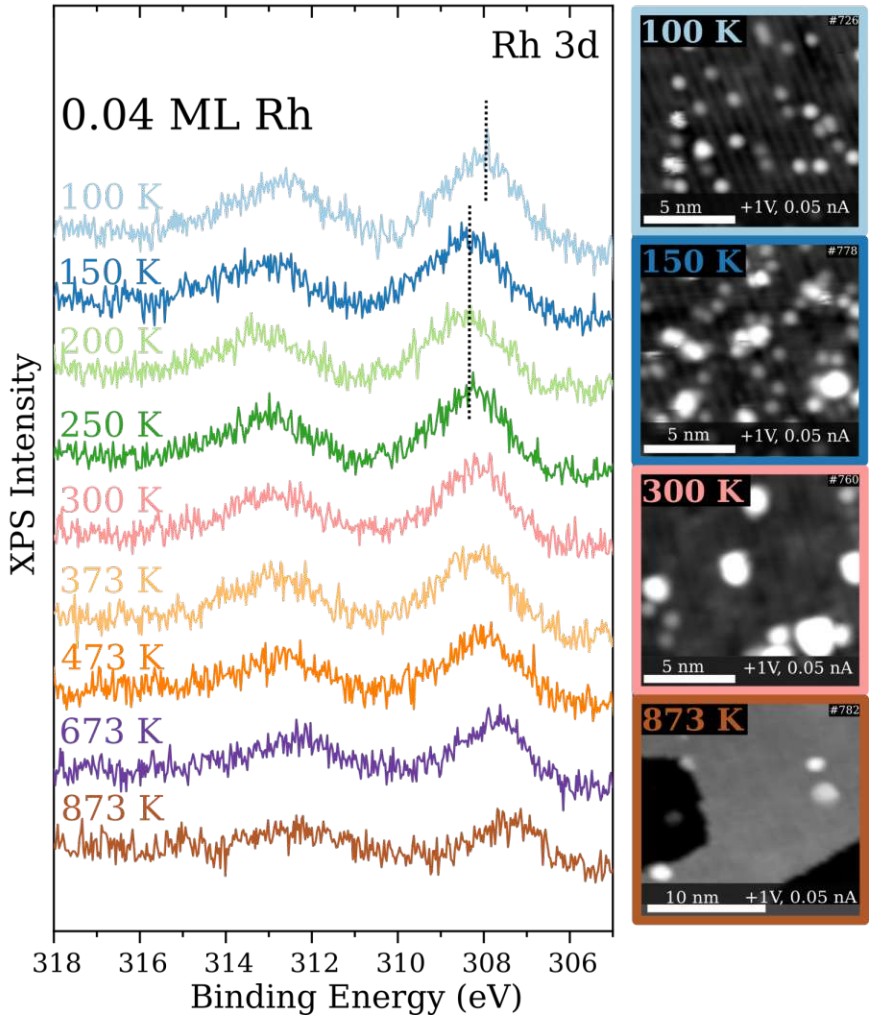

Figure 3.2: XPS spectra of the Rh 3d region and corresponding LT-STM images following deposition of 0.04 ML Rh onto r-TiO_2(110) and subsequent annealing from 100 K to 873 K. Initially dispersed Rh adatoms form clusters at 150 K, which become larger with further annealing. The Rh 3d peak shifts to higher binding energy at 150 K and then shifts back to lower binding energy at higher annealing temperatures.

binds to O_{3c} and O_{2c}. In the second most stable configuration ($E_{ads} = -3.05$ eV, middle panel) Rh^- binds exclusively to O_{3c}. The oxidation state of the Rh adatoms depends on their coordination with neighbouring oxygen atoms.
Previous studies have suggested that Rh adsorption is favoured at 3-fold coordinated

Die approbierte gedruckte Originalversion dieser Dissertation ist an der TU Wien Bibliothek verfügbar.
The approved original version of this doctoral thesis is available in print at TU Wien Bibliothek.
TU Bibliothek Your knowledge hub WIEN

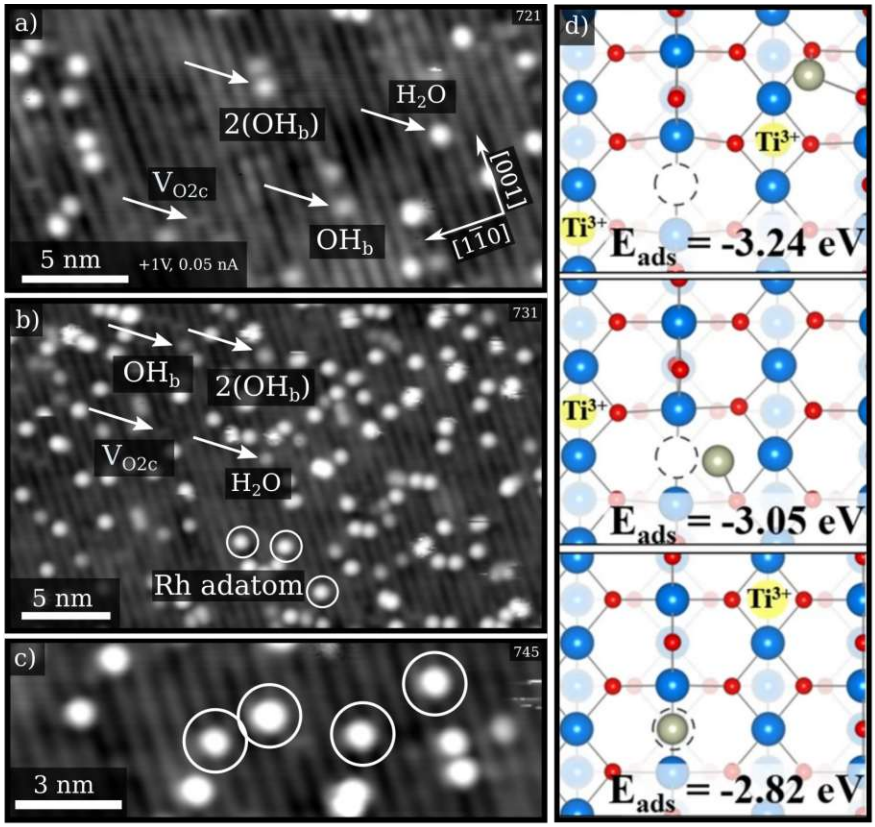

Figure 3.3: LT-STM images of the r-TiO_2(110) surface before a) and after deposition of 0.04 ML Rh b) and c). a) shows typical surface defects and adsorbates on the r-TiO_2(110) surface. Dispersed Rh adatoms, located atop Ti^{4+} rows and slightly offset towards the O_{br} rows, are marked with a white circles in b) and c). d) shows DFT+U-based calculations of Rh adatoms on the r-TiO_2(110) surface. The energetically most favoured configuration (top panel) is consistent with the adsorption site determined from STM images.

oxygen vacancies ($V_{O_{3c}}$). [149] To investigate this further, the interaction of Rh_1 at $V_{O_{3c}}$ sites was analysed by DFT+U-based calculation, which indeed identified this configuration as thermodynamically most stable. However, other studies argue that adsorption at this site is unlikely due to the energetically unfavourable formation of $V_{O_{3c}}$ on the rutile TiO_2(110) surface. [157, 158] Our calculations revealed that O migration from $V_{O_{2c}}$ to $V_{O_{3c}}$ has an energy barrier of 0.62 eV, which is significantly

Die approbierte gedruckte Originalversion dieser Dissertation ist an der TU Wien Bibliothek verfügbar.
The approved original version of this doctoral thesis is available in print at TU Wien Bibliothek.
TU Bibliothek Your knowledge hub WIEN

higher than the diffusion barrier of Rh adatoms (0.28 eV) on the rutile TiO_2(110) surface. This indicates that before Rh adatoms can adsorb at $V_{O_{3c}}$ sites, they are more likely to sinter into clusters. Therefore, the most plausible adsorption site remains the configuration described above, where Rh adatoms are coordinated to O_{3c} and O_{2c} atoms from the substrate lattice (Figure 3.3 d), top panel). This is consistent with the features in the STM images that have been identified as Rh adatoms.

The influence of co-adsorbed water

On the bare stoichiometric surface, molecular water adsorbs at temperatures lower than 275 K. [49] However, dissociation of water at $V_{O_{2c}}$ sites has been observed even at room temperature. [51] The details of water adsorption and interaction with the r-TiO_2(110) surface are explained in chapter 1.4.1.

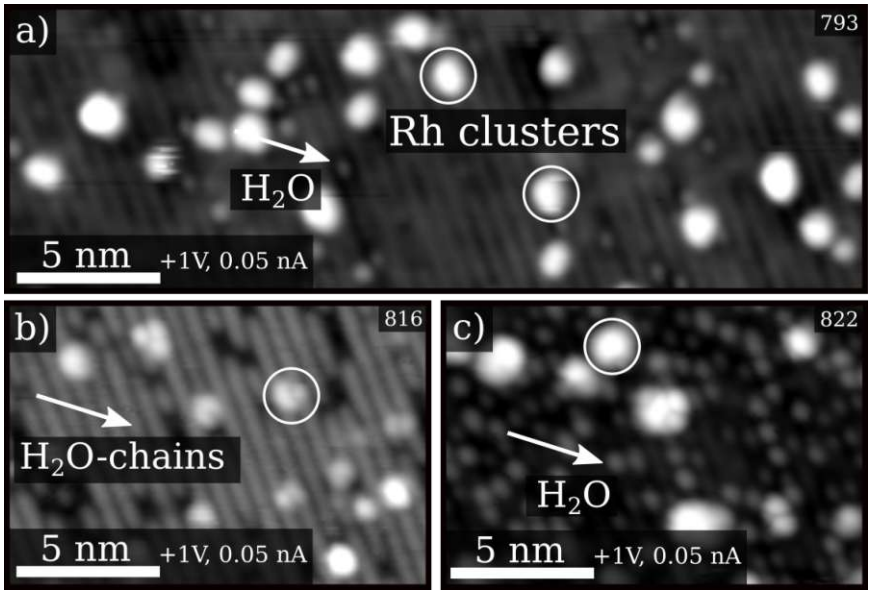

Figure 3.4: LT-STM images of the r-TiO_2(110) surface after deposition of 0.04 ML Rh in a water vapour background of $2 \cdot 10^{-8}$ mbar. Deposition at room temperature a) as well as deposition at 100 K followed by annealing to 200 K b) and 250 K c) results in clusters formation (marked with white circles). White arrows in a) and c) indicate molecular water adsorbed at Ti^{4+} sites. In b), the formation of water chains on the Ti^{4+} rows is highlighted.

Die approbierte gedruckte Originalversion dieser Dissertation ist an der TU Wien Bibliothek verfügbar.
The approved original version of this doctoral thesis is available in print at TU Wien Bibliothek.

Figure 3.4 a) shows the r-TiO_2(110) surface after deposition of 0.04 ML Rh with a water vapour background of $2 \cdot 10^{-8}$ mbar at room temperature. The formation of clusters is clearly visible on the surface (marked with white circles). This result is similar to Rh deposition at room temperature without water in the background, indicating that water does not exert a stabilizing effect on Rh adatoms on the r-TiO_2(110) surface. To eliminate the possibility that Rh undergoes sintering before forming a water-stabilized structure, an alternative approach was employed. Water vapour was dosed onto the cold surface (100 K) prior to Rh deposition. To enable STM imaging, the surface needs to be free from multilayers of water. Thus, the sample was annealed to 200 K after deposition of 0.04 ML Rh. At this temperature, chains of water molecules remain on the surface. Upon further annealing to 250 K, the water chains begin to break apart, leaving only a few water molecules on the surface. However, even with this approach, Rh sinters into small clusters already at 200 K. (see Figure 3.4 b) and c)).

Pt on rutile TiO_2(110)

The experiments in this section were carried out at the RT-STM. Figure 3.5 a), b) and c) show the r-TiO_2(110) surface after deposition of 0.007 ML Pt at room temperature. At low coverages, Pt adatoms are stabilized on the reduced surface. However, as the coverage increases, clusters become more dominant than single atoms. Even at very low coverages, a few clusters can be observed (marked with a dotted circle in Figure 3.5 a)). The Pt adatoms (marked with a white circle) preferentially adsorb at the $V_{O_{2c}}$ sites and subsequently act as nucleation sites for small clusters. The adsorption site of Pt can be identified directly through rare diffusion events of small Pt clusters from one $V_{O_{2c}}$ to another. An example of such an event is shown in Figure 3.5 b) and c), where STM images of the same area were captured a few minutes apart. The white circle highlights the small Pt cluster which hopped from one $V_{O_{2c}}$ to another. An arrow indicates the unoccupied $V_{O_{2c}}$ sites before and after the diffusion process.

Figure 3.5 d) shows the three energetically most favoured configurations for Pt adsorption on the r-TiO_2(110) surface, determined by DFT+U-based calculations. The most stable adsorption site is Pt_1 located at a $V_{O_{2c}}$ site ($E_{ads} = -3.22$ eV, top panel), which is consistent with the experimental observation. In this configuration, charge transfer from the two excess electrons associated with the $V_{O_{2c}}$ site on the reduced

Die approbierte gedruckte Originalversion dieser Dissertation ist an der TU Wien Bibliothek verfügbar.
The approved original version of this doctoral thesis is available in print at TU Wien Bibliothek.
TU Bibliothek Your knowledge hub WIEN

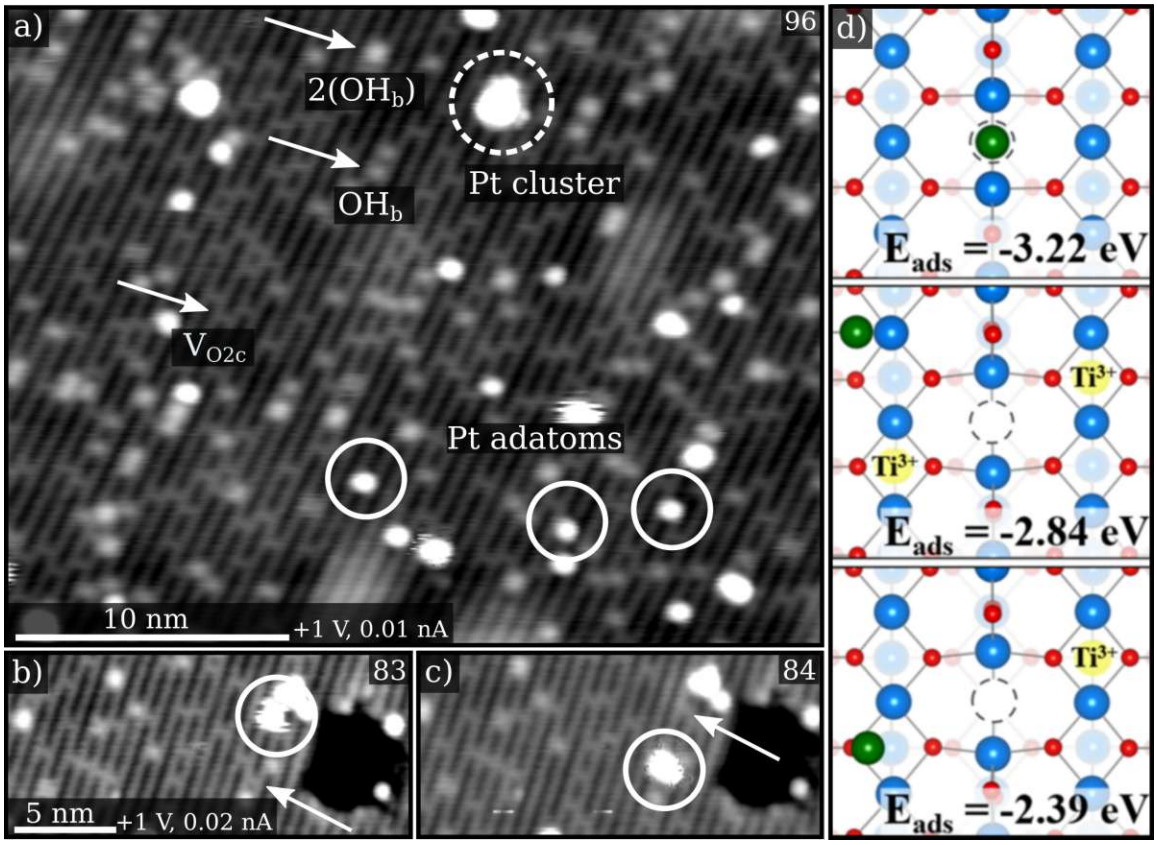

Figure 3.5: RT-STM images of the r-TiO_2(110) surface after deposition of 0.007 ML Pt at room temperature is shown in a), b) and c). In a) typical surface adsorbates and defects are marked with arrows. Pt adatoms adsorbed at $V_{O_{2c}}$ sites are marked with a circle, Pt clusters are marked with a dotted circle. b) and c) show the hopping motion of a small Pt cluster from one $V_{O_{2c}}$ site to another. d) shows the three most stable configurations of Pt adatoms on the r-TiO_2(110) surface, determined by DFT+U-based calculations. The energetically favoured configuration, atop a $V_{O_{2c}}$ site (top panel) aligns with the experimentally observed adsorption site in the STM images.

surface results in an oxidation state of Pt^{2-} for the Pt adatom. The second most stable configuration is Pt_1 bound to O_{3c} and O_{2c} ($E_{ads} = -2.84$ eV, middle panel), with Pt^0 as the most stable oxidation state. In this case, no charge transfer occurs. The third possible adsorption site, with a relatively high adsorption energy, has Pt_1

Die approbierte gedruckte Originalversion dieser Dissertation ist an der TU Wien Bibliothek verfügbar.
The approved original version of this doctoral thesis is available in print at TU Wien Bibliothek.
TU Bibliothek Your knowledge hub WIEN

adsorbed atop a O_{3c} ($E_{ads} = -2.39$ eV, bottom panel). In this configuration, Pt^{-} is the most stable oxidation state. To account for dynamic effects, the diffusion barrier of an adsorbed Pt adatom along the [001] direction was calculated. The energy barrier was determined to be relatively low (0.59 eV), enabling Pt adatoms to diffuse at room temperature and occupy the most favourable adsorption site, at a $V_{O_{2c}}$ site.

The influence of co-adsorbed water and O_2

Similar to the experiments with Rh, 0.01 ML Pt was deposited with a water vapour background of $2 \cdot 10^{-8}$ mbar at room temperature (shown in Figure 3.6 a)). Since water molecules dissociate at the $V_{O_{2c}}$ sites, forming OH_b (marked with a white arrow), Pt is unable to adsorb at these sites, resulting in rapid sintering and the formation of small Pt clusters (marked with a dashed circle).

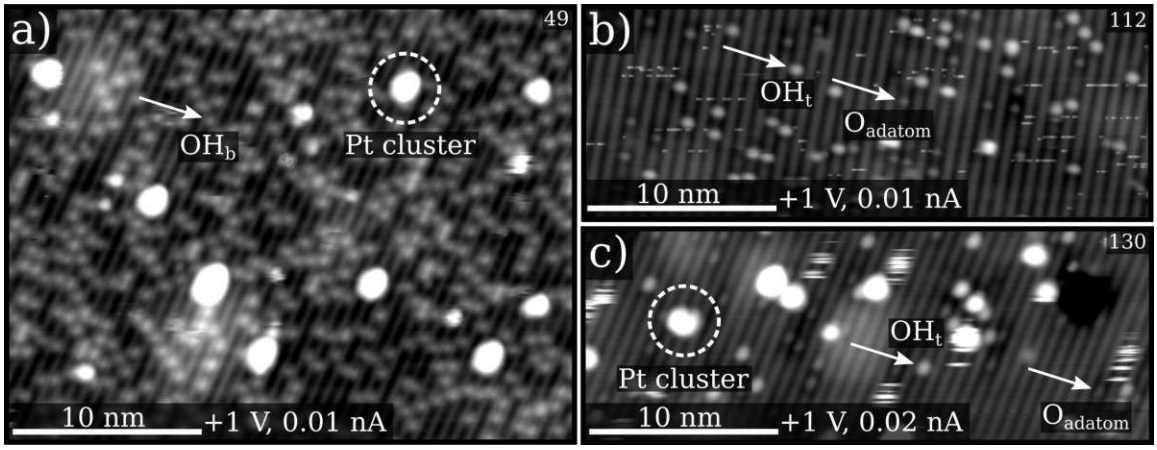

Figure 3.6: RT-STM images of 0.01 ML Pt on the r-TiO_2(110) surface. In a) hydroxylation of the surface results in rapid sintering of Pt and the formation of Pt clusters (marked with a white dashed circle), due to adsorption of hydroxyl groups at $V_{O_{2c}}$ sites. The oxidized surface is shown before b) and after c) deposition of 0.01 ML Pt. Also here, Pt exclusively forms clusters (marked with a white dashed circle in c)), because $V_{O_{2c}}$ sites are no longer present. Additionally O adatoms and hydroxyl groups adsorb at Ti_{5c} atoms (marked with a white arrow).

The introduction of O_2 has a similar effect on the dispersion of Pt (shown in Figure 3.6 c)). O_2 dissociates at the $V_{O_{2c}}$ sites, effectively "healing" the vacancy (Figure

Die approbierte gedruckte Originalversion dieser Dissertation ist an der TU Wien Bibliothek verfügbar.
The approved original version of this doctoral thesis is available in print at TU Wien Bibliothek.
TU Bibliothek Your knowledge hub WIEN

3.6 b)). This results in the formation of small Pt clusters (marked with a dashed circle). Details of the interaction of O_2 with the r-TiO_2(110) surface are explained in section 1.4.1.

Discussion

This study shows that both Rh and Pt form clusters on the r-TiO_2(110) surface at room temperature in UHV. However, Rh adatoms can be stabilized when the metal is deposited at low temperatures ($<$ 150 K). STM images show that after annealing the sample to 150 K, Rh adatoms sinter into small clusters, leading to a shift of the Rh 3d peak in the XPS spectra towards higher binding energy. Typically, a shift to lower binding energies would be expected when metal adatoms bound to O atoms transform to clusters. The observed shift to higher binding energy is likely related to a final state effect associated with the small size of Rh clusters at 150 K. A similar effect has been observed in the Au/r-TiO_2(110) system, where the behaviour of Au_1 and Au_3 differs from that of Au nanoclusters. The binding energy of Au 4f, when only Au_1 and Au_3 are present, is comparable to the binding energy observed at higher coverage corresponding to larger clusters. This phenomenon can be explained by cancellation of initial and final state effects for Au_1 and Au_3. With increasing cluster size, the binding energy initially decreases before ultimately increasing again. [157]

At 100 K, isolated Rh adatoms are located atop Ti^{4+} rows, slightly offset towards the bridging O^{2-} rows. DFT+U-based calculations are consistent with the experimentally determined adsorption site, showing that Rh adatoms are coordinated to an O_{3c} and an O_{2c} atom, with an oxidation state of Rh^0. A study by Mellor et al. analysed the adsorption site of Au adatoms on the r-TiO_2(110) surface and found that Au adatoms preferentially adsorb at $V_{O_{2c}}$ sites. [141] This behaviour differs from that of Rh adatoms, likely due to the higher electronegativity of Au compared to Rh. The higher electronegativity of Au promotes charge transfer from the $V_{O_{2c}}$ sites to Au orbitals, resulting in the reduction of the Au adatom. In contrast, Rh adatoms exhibit weaker interactions with the excess charge, making $V_{O_{2c}}$ sites less favourable for adsorption.

For Pt, a mixture of clusters and isolated single atoms is observed at room temperature. Like Au, Pt adatoms adsorb at $V_{O_{2c}}$ sites. DFT+U calculations show that excess charge from the $V_{O_{2c}}$ is transferred to the adatoms, resulting in an oxidation

Die approbierte gedruckte Originalversion dieser Dissertation ist an der TU Wien Bibliothek verfügbar.
The approved original version of this doctoral thesis is available in print at TU Wien Bibliothek.
TU Bibliothek Your knowledge hub WIEN

state of Pt^-, consistent with the behaviour of Au adatoms on r-TiO_2(110).
The influence of water on the dispersion of Rh and Pt adatoms on the r-TiO_2(110) surface was also investigated. For Rh, water has a significantly different effect compared to the Rh/α-$Fe_2O_3(1\bar{1}02)$ system. [159] On r-TiO_2(110), water has no discernible effect on the dispersion of Rh adatoms, whereas on α-$Fe_2O_3(1\bar{1}02)$ Rh exclusively forms clusters upon deposition at room temperature. However, if water vapour is present during deposition, Rh dispersion is promoted through stabilization of single Rh adatoms by OH ligands (for more details see section 4.2). Both surfaces are able to dissociate water at room temperature. [51, 93] Thus, the formation of hydroxyls on the surface cannot be the limiting factor. The different behaviour is likely due to differences in surface geometry. On α-$Fe_2O_3(1\bar{1}02)$, a square planar environment for the Rh complex is created through coordination with two surface O atoms and two hydroxyl groups, which also adsorb to the nearest surface Fe cations. On r-TiO_2(110) a Rh complex with hydroxyl groups coordinated to surface Ti atoms likely cannot form a square planar structure, which would be the favoured structure.
For Pt, the presence of water and O_2 promotes the formation of Pt clusters. Both water and O_2 dissociate at the $V_{O_{2c}}$ sites, subsequently occupy them and thereby blocking the preferred adsorption sites for Pt adatoms.

Die approbierte gedruckte Originalversion dieser Dissertation ist an der TU Wien Bibliothek verfügbar.
The approved original version of this doctoral thesis is available in print at TU Wien Bibliothek.

3.3 Pt, Rh, Ni and Ir on anatase TiO_2(101)

The experiments in this section were carried out at the RT-STM.

Interaction of water and O_2 with dark defects on anatase TiO_2(101)
To rule out the possibility of misidentifying adsorbates as metal adatoms, the anatase TiO_2(101) surface was exposed to the residual gas in the preparation chamber for two hours at room temperature and subsequently imaged by STM. Two new features appear on the surface compared to the as-prepared state. (see Figure 3.7) Given the extensive studies on molecular interactions with the anatase TiO_2(101) surface [58, 160, 161], we attribute one of these features to molecular water. [162] (marked with a cycle in Figure 3.7) However, since water is known to desorb from the anatase TiO_2(101) surface below 250 K [61], these water molecules are likely adsorbed at surface defects. The concentration of dark defects (explained in section 1.4.2 and shown in Figure 1.8) matches the concentration of the water molecules.
The second feature appears in a much lower concentration than the water molecules. We attribute them to molecular O_2 [163] (marked with a cycle and labelled as $(O_2)_{extr}$ in Figure 3.7, consistent with the labelling in the literature). The presence of O_2 molecules in the residual gas is likely a result of the oxidation process during sample preparation.

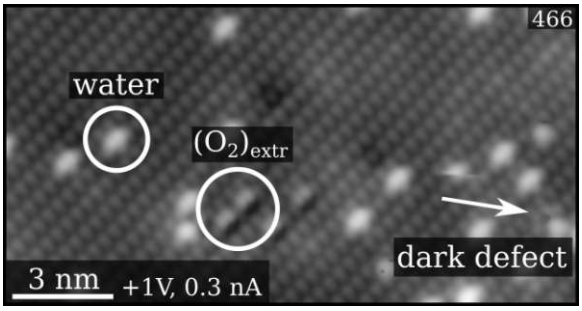

Figure 3.7: RT-STM image of the anatase TiO_2(101) surface after exposure to the residual gas in the preparation chamber for two hours. Molecular water and molecular O_2 are adsorb at the surface at room temperature, likely at surface defects. Both features are marked with a circle.

Figure 3.8 shows a series of RT-STM images captured over a time span of approximately 30 minutes, with each image acquisition taking three minutes. Notably, water

Die approbierte gedruckte Originalversion dieser Dissertation ist an der TU Wien Bibliothek verfügbar.
The approved original version of this doctoral thesis is available in print at TU Wien Bibliothek.
TU Bibliothek Your knowledge hub WIEN

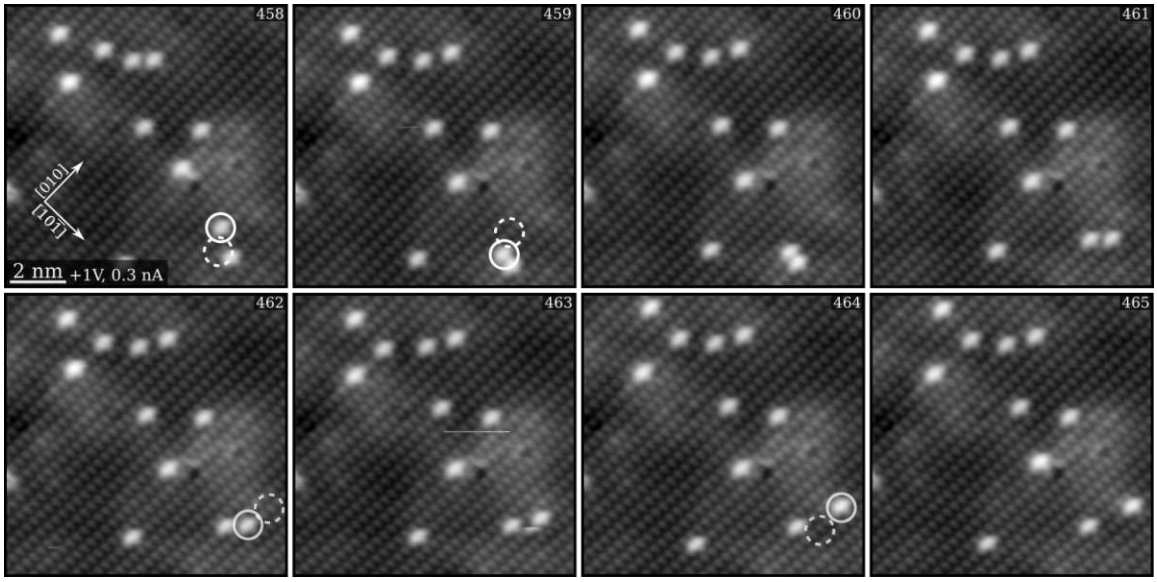

Figure 3.8: A series of RT-STM images showing the diffusion of water molecules on the anatase TiO_2(101) surface. Over a period of two hours, the sample was exposed to the residual gas in the preparation chamber at room temperature, resulting in molecule adsorption on the surface. A sequence of STM images, acquired at the same position over approximately 30 minutes, demonstrates that adsorbed water molecules can move both along and across the [010] direction. Image 458 and 459 show movement across the [010] direction, while image 462 and 464 show movement along the [010] direction. The full circles mark the position of the water molecule, and the dashed circle indicate the position before or after the movement.

molecules are observed to diffuse across the surface at room temperature. However, their diffusion does not leave behind a dark defect, suggesting that the water molecules move together with the dark defects. This observation challenges the assumption in literature that the dark defects are cations substituting Ti in the lattice. [58] Instead, these defects may be interstitial lattice species or surface sites above a subsurface defect such as an oxygen vacancy.

Moreover, molecular O_2 also adsorbs in low concentration on the anatase TiO_2(101) surface after exposure to the residual gas and exhibits mobility on the surface. (see Figure 3.9) In a rare event, O_2 molecules have been observed to move atop dark defects, without leaving any defects behind. This behaviour implies the existence of

Die approbierte gedruckte Originalversion dieser Dissertation ist an der TU Wien Bibliothek verfügbar.
The approved original version of this doctoral thesis is available in print at TU Wien Bibliothek.
TU Bibliothek Your knowledge hub WIEN

other defect sites on the surface, which are not visible in the STM images but may bind adsorbates more strongly than regular lattice sites.

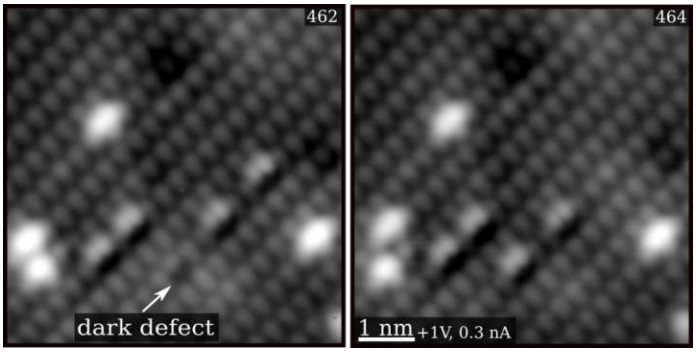

Figure 3.9: A series of RT-STM images showing the diffusion of O_2 molecules on the anatase TiO_2(101) surface. Over a period of two hours, the sample was exposed to the residual gas in the preparation chamber at room temperature, resulting in molecule adsorption on the surface. In the second image, an adsorbed O_2 molecule has moved to occupy a dark defect (marked with an arrow in the first image), leaving behind an apparently regular lattice site.

Overall, these results indicate that regular lattice sites on the anatase TiO_2(101) surface are inert at room temperature, while defects present on the surface can act as binding sites for molecules. This finding is particularly significant for the next sections, where I demonstrate that such defect sites can bind not only small molecules but also metal adatoms.

Pt on anatase TiO_2(101)

Figure 3.10 shows the anatase TiO_2(101) surface after Pt deposition with and without a water vapour background of $2 \cdot 10^{-8}$ mbar at room temperature. First, a coverage of 0.05 ML Pt was deposited in UHV (see Figure 3.10 a)).

At this coverage a coexistence of large clusters and smaller features with a uniform apparent height of 150–160 pm is observed. These features are predominantly visible at the terraces rather than on the step edges, consistent with results previously reported in the literature. [150] When a lower coverage of 0.01 ML Pt was deposited (see Figure 3.10 b)), a mixture of clusters and single features is visible, but the density and average cluster size was reduced compared to the higher coverage. At a coverage

Die approbierte gedruckte Originalversion dieser Dissertation ist an der TU Wien Bibliothek verfügbar.
The approved original version of this doctoral thesis is available in print at TU Wien Bibliothek.

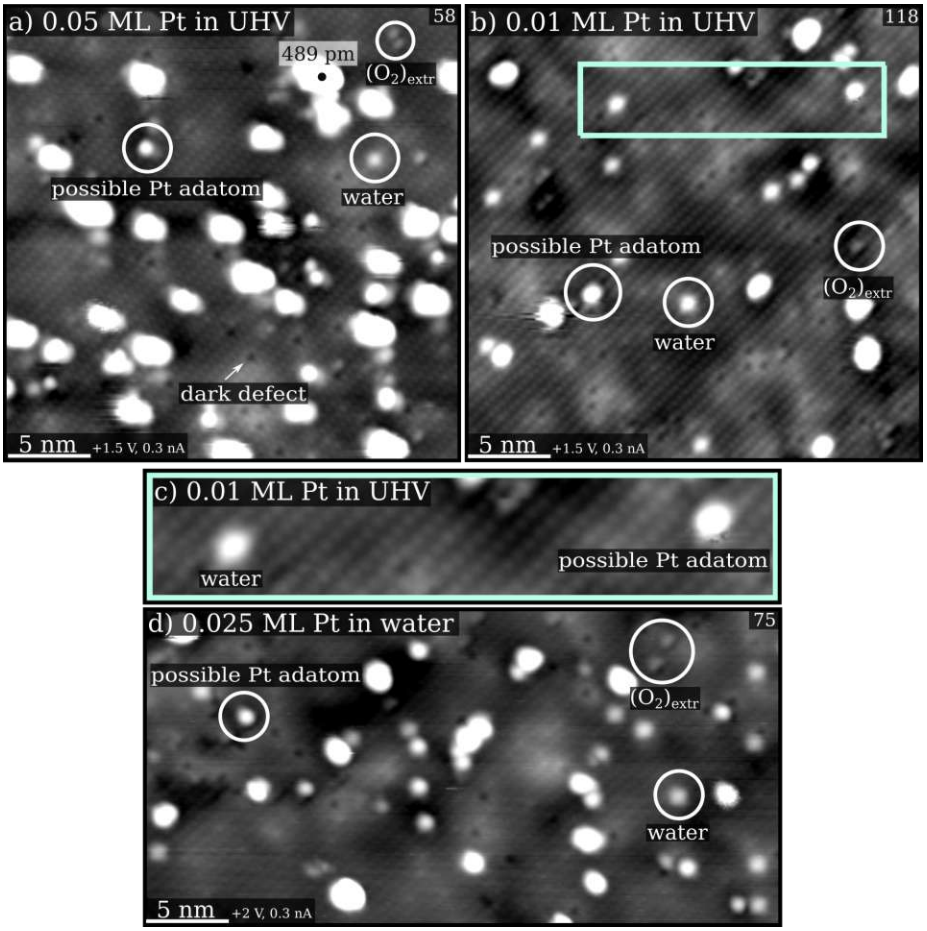

Figure 3.10: RT-STM images of Pt with and without the influence of water on the anatase $TiO_2(101)$ surface. a) and b) show the surface after deposition of 0.05 and 0.01 ML Pt in UHV at room temperature. A black dot marks the cluster with the highest apparent height, measuring 489 pm. c) shows an enlarged section of b), highlighting the different appearances of a water molecule and a possible Pt_1 species. Although they adsorb at the same site on the surface, they differ in apparent height. d) shows the surface after deposition of 0.025 ML Pt in a water vapour background of $2 \cdot 10^{-8}$ mbar at room temperature. In all images, a mixture of clusters and possible Pt_1 species can be observed. White circles mark the possible Pt_1 species as well as the adsorbed molecules, dark defects are marked with an arrow.

Die approbierte gedruckte Originalversion dieser Dissertation ist an der TU Wien Bibliothek verfügbar.
The approved original version of this doctoral thesis is available in print at TU Wien Bibliothek.

of 0.05 ML Pt, ≈7 % of the deposited Pt could be attributed to small Pt features, while at 0.01 ML Pt coverage, this number increases to ≈17 %. The smallest Pt features appear to adsorb at the same sites on the surface as water molecules but can be easily distinguished due to their significant greater apparent height. Water molecules typically exhibit an average apparent height of 60–80 pm. Figure 3.10 c) shows an enlarged section of Figure 3.10 b), comparing the distinct appearances of small Pt features and water molecules. Furthermore, their mobility differs: Pt features remain immobile at room temperature, whereas water molecules diffuse across the surface. Because of their small and uniform appearance, we tentatively assign the smallest Pt features to Pt_1 species. However, we cannot exclude the possibility that these features represent dimers or trimers, if these are significantly more stable on the anatase $TiO_2(101)$ surface.

The influence of co-adsorbed water

Figure 3.10 d) shows the anatase $TiO_2(101)$ surface after deposition of 0.025 ML Pt in a water vapour background of $2 \cdot 10^{-8}$ mbar at room temperature. Similar to the images of Pt adsorption in UHV, a mixture of clusters and possible single atoms is observed. This suggests that water, in this low-pressure regime, does not have a significant effect on the Pt/anatase $TiO_2(101)$ system.

Rh on anatase $TiO_2(101)$

Figure 3.11 a) shows the anatase $TiO_2(101)$ surface after deposition of 0.02 ML Rh at room temperature in UHV. In contrast to Pt, Rh forms only small clusters on the terraces. No species that could be attributed to possible Rh_1 species can be observed, leading to the conclusion that these species are not stable on the anatase $TiO_2(101)$ surface at room temperature. This behaviour closely resembles that of Rh on rutile $TiO_2(110)$, where Rh adatoms begin to sinter as early as 150 K. (see section 3.2) [132]

The influence of co-adsorbed water

Figure 3.11 b) shows the anatase $TiO_2(101)$ surface after deposition of 0.02 ML Rh at room temperature in a water vapour background of $2 \cdot 10^{-8}$ mbar. Similar to the observation in UHV, only small clusters are visible, and no features corresponding to possible Rh_1 species are detected. This behaviour mirrors the Rh/rutile $TiO_2(110)$ system after introducing water.

Die approbierte gedruckte Originalversion dieser Dissertation ist an der TU Wien Bibliothek verfügbar.
The approved original version of this doctoral thesis is available in print at TU Wien Bibliothek.
TU Bibliothek Your knowledge hub WIEN

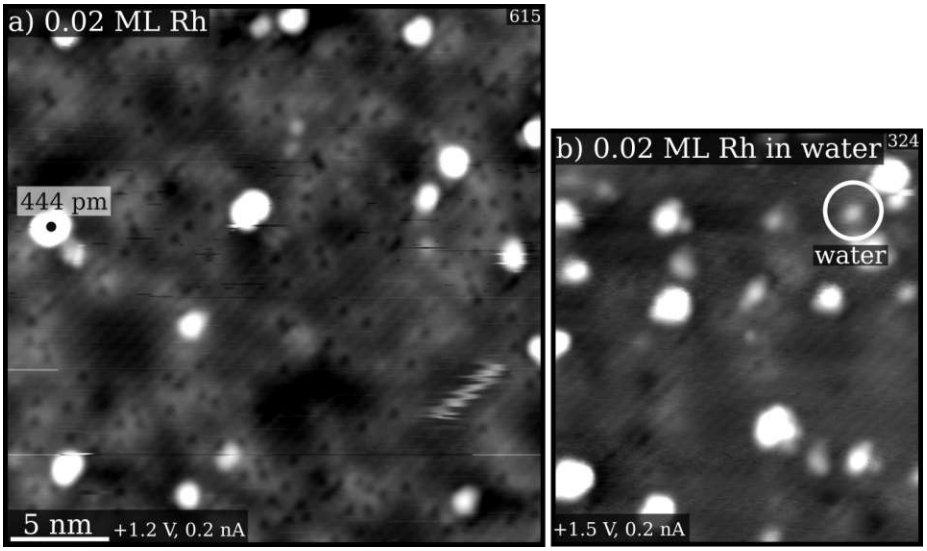

Figure 3.11: RT-STM images of Rh with and without the influence of water on the anatase $TiO_2(101)$ surface. a) shows the surface after deposition of 0.02 ML Rh in UHV at room temperature. A black dot marks the cluster with the highest apparent height, measuring 444 pm. b) shows the surface after deposition of 0.02 ML Rh in a water vapour background of $2 \cdot 10^{-8}$ mbar at room temperature. In both images, small clusters are visible. A white circle marks an adsorbed water molecule.

Ni on anatase $TiO_2(101)$

Figure 3.12 a) shows the anatase $TiO_2(101)$ surface after deposition of 0.02 ML Ni at room temperature in UHV. This system resembles the Pt/anatase $TiO_2(101)$ system, forming a mixture of clusters and small uniform features with an apparent height of 150–170 pm. These features are tentatively assigned to Ni_1 species. Similar to the Pt/anatase $TiO_2(101)$ system, the possible Ni_1 species can be distinguished from adsorbed water molecules on the surface by two key differences: apparent height and mobility (possible Ni_1 species are immobile at room temperature in contrast to the water molecules). The concentration of the possible Ni_1 species is ≈20 % of the deposited Ni, which is significantly higher than the concentration of the possible Pt_1 species observed in the analogous Pt system.

Die approbierte gedruckte Originalversion dieser Dissertation ist an der TU Wien Bibliothek verfügbar.
The approved original version of this doctoral thesis is available in print at TU Wien Bibliothek.
TU Bibliothek Your knowledge hub WIEN

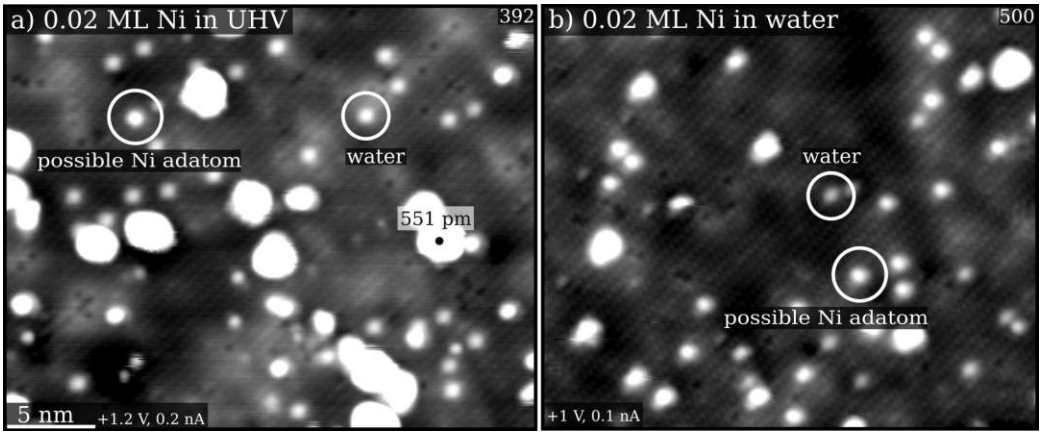

Figure 3.12: RT-STM images of Ni with and without the influence of water on the anatase $TiO_2(101)$ surface. a) shows the surface after deposition of 0.02 ML Ni in UHV at room temperature. A black dot marks the cluster with the highest apparent height, measuring 551 pm. b) shows the surface after deposition of 0.02 ML Ni in a water vapour background of $2 \cdot 10^{-8}$ mbar at room temperature. In both images, a mixture of clusters and possible Ni_1 species is visible. However, the amount of possible Ni_1 species increases significantly upon the introduction of water. White circles mark the possible Ni_1 species and the adsorbed water molecules.

The influence of co-adsorbed water

Figure 3.12 b) shows the anatase $TiO_2(101)$ surface after deposition of 0.02 ML Ni at room temperature in a water vapour background of $2 \cdot 10^{-8}$ mbar. Interestingly, the proportion of possible Ni_1 species doubles, increasing from ≈20 % of the deposited Ni in UHV to ≈40 % when deposited in the presence of water vapour. These possible Ni_1 species retain the same appearance and position on the lattice, suggesting that water plays a crucial role in the dispersion and stabilization of Ni adatoms on the anatase $TiO_2(101)$ surface.

Ir on anatase $TiO_2(101)$

Figure 3.13 a) shows the anatase $TiO_2(101)$ surface after deposition of 0.02 ML Ir at room temperature. At this coverage, Ir forms small, nearly uniform features with an apparent height of 130–170 pm, which are tentatively assigned to Ir_1 species.

Die approbierte gedruckte Originalversion dieser Dissertation ist an der TU Wien Bibliothek verfügbar.
The approved original version of this doctoral thesis is available in print at TU Wien Bibliothek.

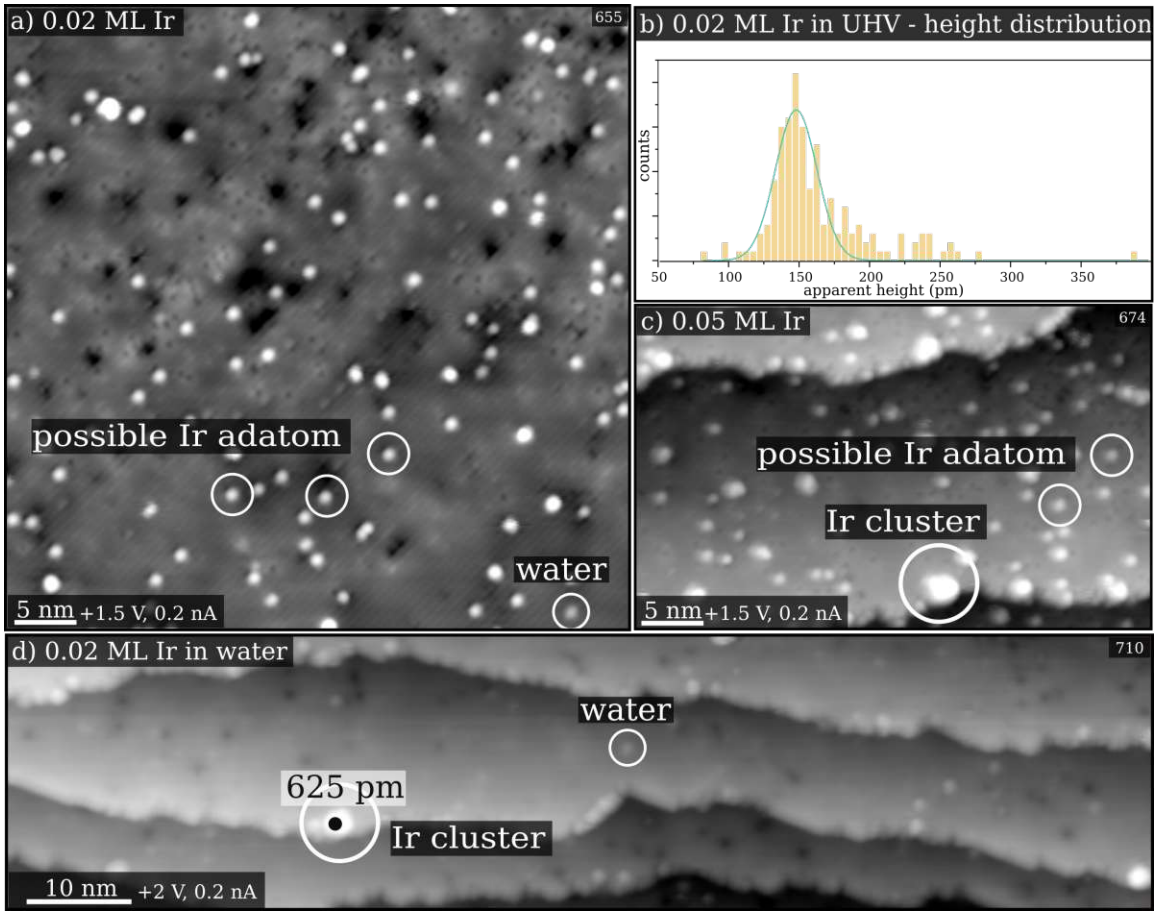

Figure 3.13: RT-STM images of Ir with and without the influence of water on the anatase $TiO_2(101)$ surface. a) shows the surface after deposition of 0.02 ML Ir in UHV at room temperature, where Ir forms uniform single-dispersed features that can be assigned to Ir_1 species. b) shows a histogram of the apparent height of all features on the surface. c) shows the surface after deposition of 0.05 ML Ir in UHV at room temperature, resulting in an increased cluster density. d) shows the surface after the deposition of 0.02 ML Ir in a water vapour background of $2 \cdot 10^{-8}$ mbar at room temperature. In this case, water leads to the formation of large cluster, stabilized at step edges. A black dot marks the cluster with the highest apparent height, measuring 625 pm.

Die approbierte gedruckte Originalversion dieser Dissertation ist an der TU Wien Bibliothek verfügbar.
The approved original version of this doctoral thesis is available in print at TU Wien Bibliothek.

These features appear at a coverage of 0.011 ML and are easily distinguishable from water molecules by their apparent height and immobility. In addition to the possible single atoms, a few small clusters are also visible. In Figure 3.13 b) a histogram shows the apparent heights of all features on the surface. A clear peak emerges at around 150 pm, which can be attributed to single Ir adatoms. A shoulder at larger apparent heights originates from small clusters. Assuming each cluster consists of multiple Ir atoms, the coverage of the small uniform Ir features aligns well with their assignment to Ir_1 species. If the features at 150 pm were considered to be dimers, the QCM calibration of the experimental setup would significantly underestimate the amount of Ir deposited, which is unlikely. Thus, the formation of dimers can be ruled out. In Figure 3.13 c) the Ir coverage was increased to 0.05 ML, resulting in a higher density of clusters. However, the density of Ir adatoms remains unaffected.

The influence of co-adsorbed water

Figure 3.13 d) shows the anatase $TiO_2(101)$ surface after deposition of 0.02 ML Ir at room temperature in a water vapour background of $2 \cdot 10^{-8}$ mbar. The presence of water leads to rapid sintering of the Ir_1 species, resulting in the formation of large clusters that stabilize at the step edges of the surface. This behaviour contrasts sharply with the effect of water on the other metals studied on the anatase $TiO_2(101)$ surface.

Adsorption site of Pt, Ni and Ir adatoms on the anatase $TiO_2(101)$ surface and XPS spectra of all deposited metals

Figure 3.14 shows high-resolution STM images of all metal adatoms studied, along with a model of the predicted adsorption site for Pt and Rh adatoms on the anatase $TiO_2(101)$ surface, as determined by DFT+U calculation. Previous studies have shown that adatoms preferentially adsorb between two O_{2c} sites along the [010] direction. [150, 153, 164, 165] In Figure 3.14 a) this adsorption site is highlighted with a grey circle.

To determine the exact adsorption sites of Pt, Ni, and Ir adatoms from the experimental data, orange dots mark the approximate position of surface Ti_{5c} atoms on the lattice. For Pt and Ir adatoms deposited in UHV, as well as Pt adatoms deposited in a water vapour background, the possible Pt_1 (Figure 3.14 b) and c)) and Ir_1 species (Figure 3.14 f)) appear to adsorb between two O_{2c} atoms, assuming that the substrate maxima observed in the STM images are closer to the Ti_{5c} surface atoms than

Die approbierte gedruckte Originalversion dieser Dissertation ist an der TU Wien Bibliothek verfügbar.
The approved original version of this doctoral thesis is available in print at TU Wien Bibliothek.
TU Bibliothek Your knowledge hub WIEN

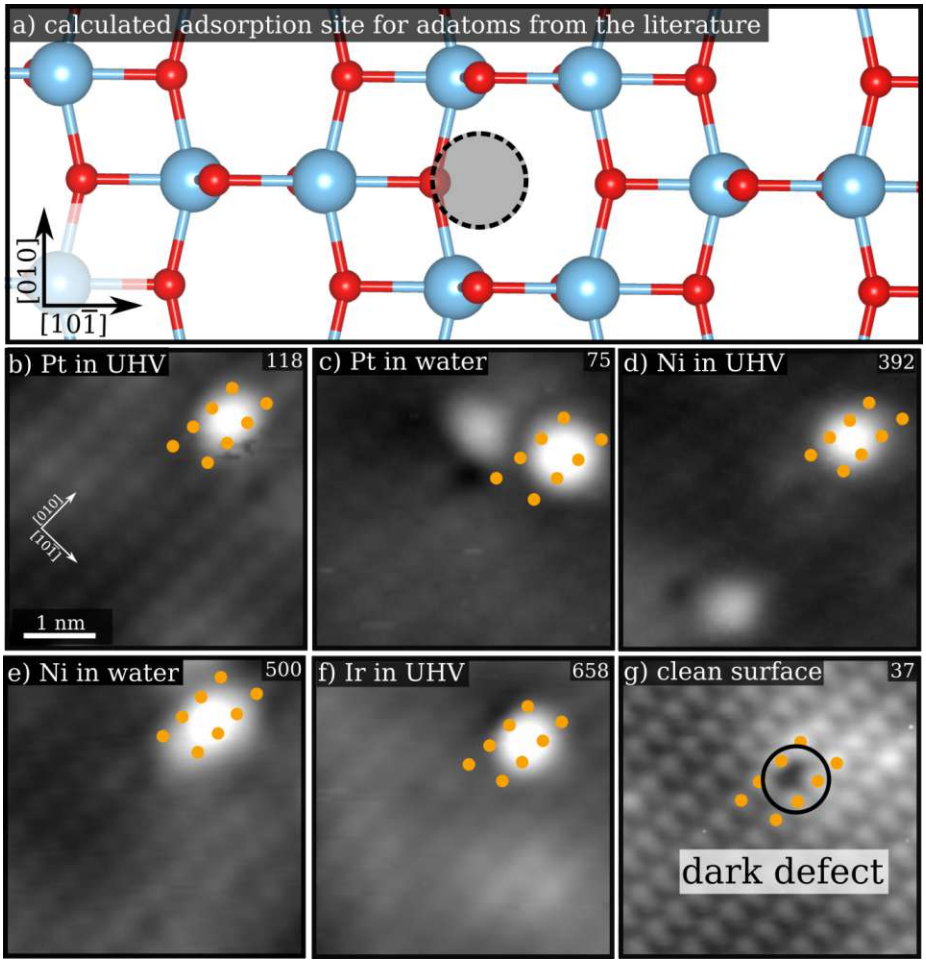

Figure 3.14: Enlarged RT-STM images of Pt_1, Ni_1 and Ir_1 species on the anatase TiO_2(101) surface. a) shows the most stable adsorption site of Pt and Rh adatoms, determined by DFT+U calculations, [150, 153, 164, 165] located between two surface O_{2c} atoms (marked by a grey circle). In b)–g), orange dots indicate the approximate positions of surface Ti_{5c} atoms, aiding in determining the extract adsorption site of all metal atoms deposited in UHV (b, d, f) and in a water vapour background of $2 \cdot 10^{-8}$ mbar (c, e), as well as the position of a dark defect (g).

to the O_{2c} surface atoms. This adsorption site aligns well with the computational predictions. However, the position of the dark defects (Figure 3.14 g)) coincides with the adsorption site of possible Pt_1 and Ir_1 species, suggesting that these defects sta-

Die approbierte gedruckte Originalversion dieser Dissertation ist an der TU Wien Bibliothek verfügbar.
The approved original version of this doctoral thesis is available in print at TU Wien Bibliothek.
TU Bibliothek Your knowledge hub WIEN

bilize the metal adatoms on the surface.

For Ni adatoms deposited in UHV and in water, the possible Ni_1 species occupy a slightly different adsorption site, shifted half a unit cell upwards along the Ti_{5c} row (Figure 3.14 d) and e)). Despite this difference, it is presumed that Ni adatoms, similar to Pt and Ir adatoms, are likely trapped at surface defect sites.

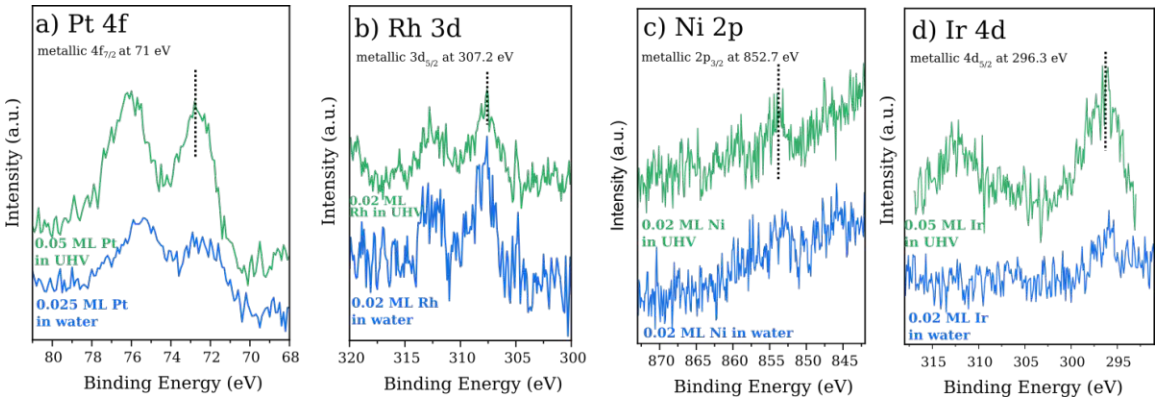

Figure 3.15: XPS spectra of Pt, Rh, Ni and Ir deposited in UHV and in a water vapour background of $2 \cdot 10^{-8}$ mbar. The dotted lines mark the peak maxima of the individual metals deposited on the anatase $TiO_2(101)$ surface. Deposition in water has no significant effect on the peak shift, only the intensity varies due to sintering or dispersion of the metals. For comparison, the peak maxima of the respective pure metals in the bulk are noted on the top left side of each spectrum.

In addition to the STM data, XPS measurements were conducted on all four metals deposited in UHV and in a water vapor background (see Figure 3.15). For Pt, Rh, and Ni, the XPS peaks are shifted towards higher binding energy compared to those of the corresponding pure metals in the bulk. The presence of water vapour does not significantly impact the peak positions; the main observable effect is on the peak intensity, which varies depending on the extent of sintering or dispersion of the deposited metals caused by the water vapour.

Discussion

This study demonstrates that Pt, Rh, and Ni tend to sinter and form clusters when deposited in UHV at room temperature on the anatase $TiO_2(101)$ surface. Among the four metals analysed, Rh exhibits the least stability, forming exclusively clusters. In

Die approbierte gedruckte Originalversion dieser Dissertation ist an der TU Wien Bibliothek verfügbar.
The approved original version of this doctoral thesis is available in print at TU Wien Bibliothek.
TU Bibliothek Your knowledge hub WIEN

contrast, Pt and Ni form a mixture of clusters and small uniform features, which are attributed to adatoms based on their consistent apparent height, uniform appearance, and defined adsorption sites on the lattice. Interestingly, Ir behaves differently from the other three metals. At low metal coverage, Ir forms highly dispersed, uniform features, which are also attributed to adatoms based on their uniform appearance and quantitative analysis of the STM images. As the coverage is increased, small clusters begin to form.

Considering that the metal adatoms are coordinated to surface O atoms, the oxygen affinity of each metal clearly plays a crucial role in their stability and behaviour. A recent study by Campbell and co-workers [166] investigated the adsorption of various transition metals on MgO(110) and CeO_{2-x}(111) surfaces, identifying an oxygen affinity trend of Ir > Ni > Rh > Pt. Except for Pt, this trend aligns well with the experimental findings on the dispersion of Pt, Rh, Ni, and Ir on the anatase TiO_2(101) surface under UHV conditions.

The XPS spectra of all four metals after deposition in UHV show a shift to higher binding energies compared to those of the corresponding pure metals in the bulk. This shift can be attributed to a combination of initial and final state effects associated with small clusters and metal adatoms, as well as charge transfer between the clusters or adatoms on the oxide surface. The magnitude of the shift varies among the metals. For instance, the Ir 4d peak exhibits the smallest shift. The variations in binding energy shifts can depend on the specific core level being probed and its sensitivity to changes in the chemical environment. Higher-energy core levels, such as Ir 4d, typically exhibit smaller relative shifts compared to lower-energy core levels. [167] This difference in sensitivity underscores the complexity of interpreting XPS binding energy shifts in metal-oxide systems.

A recent study determined the diffusion barrier for Pt adatoms along the [010] direction on the anatase TiO_2(101) surface to be 0.86 eV [168]. This value suggests that at room temperature, Pt adatom are likely to diffuse across the surface and form clusters unless stabilized by defect sites. DFT+U calculations predict that Pt adatoms are stabilized at $V_{O_{2c}}$ sites with an adsorption energy of 4.71 eV, compared to 2.20 eV on regular lattice sites. [150] However, as discussed in section 1.4.2, $V_{O_{2c}}$ sites are thermodynamically unstable on the anatase TiO_2(101) surface and tend to diffuse into the subsurface region, stabilizing as subsurface defects. Despite this instability, it is possible that the presence of Pt adatoms could drive $V_{O_{2c}}$ to diffuse to

Die approbierte gedruckte Originalversion dieser Dissertation ist an der TU Wien Bibliothek verfügbar.
The approved original version of this doctoral thesis is available in print at TU Wien Bibliothek.
TU Bibliothek Your knowledge hub WIEN

the surface, where the defects might stabilize the adatoms. [169]
The adsorption site of Pt and Ir adatoms on the anatase $TiO_2(101)$ surface is located between two adjacent surface O_{2c} atoms, consistent with computational studies on Pt adatoms on the anatase $TiO_2(101)$ surface. [150, 165, 168]. However, this location differs from the position of the $V_{O_{2c}}$ sites, where adatoms would be adsorbed directly above an O_{2c} site. This discrepancy suggests that the immobile Pt_1 and Ir_1 species are stabilized by another type of defect. Interestingly, the adsorption site of Ni adatoms is slightly offset from those of Pt_1 and Ir_1 species, raising the possibility that Ni adatoms might indeed be stabilized at $V_{O_{2c}}$ sites.
Dark defects observed in STM images are located between two O_{2c} atoms (Figure 3.14 g)), making them strong candidates for stabilizing Pt and Ir adatoms. However, their inhomogeneous distribution prevents quantitative analysis of how many defects are occupied by other species. Consequently, we cannot exclude that other types of defects contribute to metal adatom stabilization.
The chemical nature of the dark defects remains unclear, though several potential explanations have been ruled out. A previous study suggests they are substitutional Nb dopant. [58] However, the observed diffusion of the dark defects after adsorption of water molecules makes this unlikely. While XPS survey spectra indicate a small peak in the Fe 2p region, suggesting the presence of Fe impurities, substitutional Fe cations can also be excluded, as Fe typically forms patches on the surface with a distinct appearance unlike the dark defects. [57] Additionally, the appearance of common adsorbates present in the residual gas, such as O_2, water, CO, and OH on the anatase $TiO_2(101)$ surface is well-established, allowing these molecules to be ruled out as potential explanations for the dark defects. [58, 162]
A study by Hebenstreit et al. proposed that these defects could be a Ti interstitial. [170] While the precise chemical nature of the dark defects remains uncertain, our findings suggest that extrinsic doping of the oxide could provide a strategy to create stronger binding sites, potentially stabilizing expensive metal adatoms on the anatase $TiO_2(101)$ surface.
Next, we take a look at the effect of water on the dispersion of the four metals analysed in this study. A recent study has reported that hydroxyl groups on the anatase $TiO_2(101)$ surface can stabilize Pt adatoms through the formation of PtO_2 species. [153] Unfortunately, this effect was not observed under the experimental conditions employed in this study. Both deposition in UHV and in a water vapour background

Die approbierte gedruckte Originalversion dieser Dissertation ist an der TU Wien Bibliothek verfügbar.
The approved original version of this doctoral thesis is available in print at TU Wien Bibliothek.
TU Bibliothek Your knowledge hub WIEN

resulted in a mixture of Pt_1 species and clusters. For Rh, the behaviour on the anatase $TiO_2(101)$ surface mirrors that observed on r-$TiO_2(110)$. On both surfaces, Rh exclusively forms clusters upon deposition in water, differing significantly from its behaviour on α-$Fe_2O_3(1\bar{1}02)$, where Rh forms single dispersed adatoms stabilized by OH ligands (see section 4.2 [159]). This difference may be attributed to the molecular adsorption of water on the anatase $TiO_2(101)$ surface, whereas on α-$Fe_2O_3(1\bar{1}02)$, water partially dissociates even at room temperature. [93] Another contributing factor, similar to r-$TiO_2(110)$, could be the differing surface geometries. As discussed in section 4.2, the α-$Fe_2O_3(1\bar{1}02)$ surface enables a square planar coordination environment for the Rh complex, which is energetically favourable. [159] On the anatase $TiO_2(101)$ surface a Rh complex with hydroxyl groups coordinated to surface Ti atoms, can at best form a threefold coordination, which is less favourable.
Ni is the only metal in this study that shows significantly higher dispersion when deposited in a water vapour background. The concentration of single Ni adatoms doubles from ≈20 % when deposited in UHV to ≈40 % when deposited in the presence of water. The apparent height and adsorption site remains consistent in both conditions, suggesting that the Ni adatoms may already be partially stabilized by the water present in the residual gas of the UHV chamber. Ir exhibits a very different behaviour compared to the other metals. Water promotes sintering of the dispersed Ir adatoms, leading to the formation of clusters that are likely mobile and eventually get trapped at step edges.
The XPS spectra of the metals deposited in UHV and in a water vapour background do not differ significantly in binding energy. For Pt and Rh, this result is unsurprising, as no changes in dispersion or clustering were observed upon introducing water. For Ni and Ir, one might expect a shift, due to the increased dispersion of Ni and the clustering of Ir. However, the sensitivity of the XPS-setup appears insufficient to detect such a small shift. Only the intensity of the peaks changes, reflecting the extent of sintering or dispersion of the metals.

For both rutile $TiO_2(110)$ and anatase $TiO_2(101)$ surfaces, the effect of water is difficult to predict. Given that water and hydroxyl groups are ubiquitous on metal-oxide surfaces, omitting water in computational studies of SAC systems likely oversimplifies the reality. Additionally, water can significantly impact reaction mechanisms, with evidence indicating its role in influencing SAC reaction pathways. [151, 152]

Die approbierte gedruckte Originalversion dieser Dissertation ist an der TU Wien Bibliothek verfügbar.
The approved original version of this doctoral thesis is available in print at TU Wien Bibliothek.
TU Bibliothek Your knowledge hub WIEN

One of the goals of this study was to identify any metal/support systems that could serve as reliable models for surface science investigations of SAC mechanisms. While metals that form adatoms could potentially allow for adsorption studies using STM and nc-AFM, the uncertainty over the nature of the defect sites stabilizing the adatoms on anatase $TiO_2(101)$ complicates reliable modelling of the system. Furthermore, for both TiO_2 surfaces, the presence of clusters hinders the ability to differentiate the reactivity of single atoms from that of clusters. Therefore, none of the studied systems currently qualifies as a suitable model system for SAC studies.

Die approbierte gedruckte Originalversion dieser Dissertation ist an der TU Wien Bibliothek verfügbar.
The approved original version of this doctoral thesis is available in print at TU Wien Bibliothek.

4 Adatom stabilization with the influence of co-adsorbed water on α-$Fe_2O_3(1\bar{1}02)$

In this chapter, the influence of co-adsorbed water on the stability of Rh adatoms supported on the α-$Fe_2O_3(1\bar{1}02)$ surface is investigated. The results have been published in ref. [159]. RT-STM images and XPS spectra were conducted and interpreted by Florian Kraushofer, and are essential for the completeness and full understanding of the study.

4.1 Introduction

Commonly, in computational studies, the α-$Fe_2O_3(0001)$ surface is used to represent the FeO_x catalyst. [11, 171, 172] However, since the surface termination is not fully understood under UHV conditions [79], the α-$Fe_2O_3(1\bar{1}02)$ surface serves as a much better model system due to a well-defined and stable bulk-truncated termination. Moreover, the interaction of water with the surface is well-characterized, and it has been established that the surface remains stable even after exposure to liquid water. [93] (for more details, see section 1.5.2)
Despite the advantages of the α-$Fe_2O_3(1\bar{1}02)$ surface limited studies on model SAC have been conducted using this system. Current research primarily explores the interaction with Pt and Rh. Pt atoms were found to significantly alter the support lattice, enabling a pseudolinear coordination with surface O atoms. [173] A study by Kraushofer et. al [174] demonstrated that when Rh is deposited in a UHV environment at room temperature, small clusters form on the surface. Interestingly, these clusters can redispers and incorporate into the immediate subsurface layer upon

Die approbierte gedruckte Originalversion dieser Dissertation ist an der TU Wien Bibliothek verfügbar.
The approved original version of this doctoral thesis is available in print at TU Wien Bibliothek.

annealing the sample. However, this process implies that the Rh adatoms are inaccessible to reactants, making it unlikely for the system to function as an active SAC.

4.2 Rh adatoms stabilized on α-$Fe_2O_3(1\bar{1}02)$ by co-adsorbed water

STM and XPS

Figure 4.1 a) and b) show RT-STM images of the α-$Fe_2O_3(1\bar{1}02)$ surface after deposition of Rh with (a) and without (b) a water vapour background of $2 \cdot 10^{-8}$ mbar at room temperature. As expected, deposition in UHV leads to the formation of Rh clusters on the terraces. However, when Rh is deposited in the presence of water vapour, uniform isolated features appear on the surface.

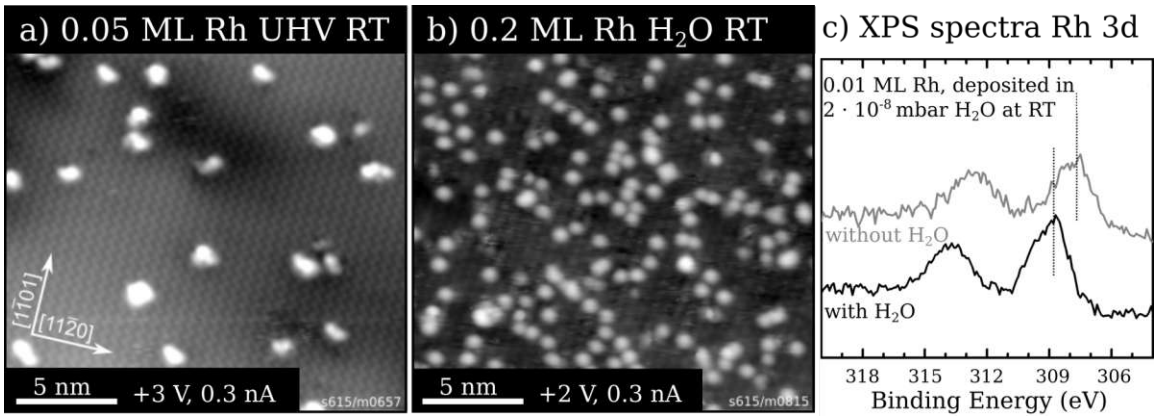

Figure 4.1: RT-STM images of the α-$Fe_2O_3(1\bar{1}02)$ surface after Rh deposition with (a) and without (b) a water vapour background of $2 \cdot 10^{-8}$ mbar at room temperature. In a), Rh nanoclusters can be observed, while in b), single isolated features appear on the surface. c) shows XPS spectra of the Rh 3d region. A shift in binding energy from 307.6 eV to 308.9 eV is observed when comparing Rh clusters to isolated Rh adatoms. Data acquisition and interpretation done by Florian Kraushofer.

To determine whether the features in Figure 4.1 b) correspond to Rh adatoms and not dimers or trimers, the sample was annealed to 520 °C in O_2 and the number of

Die approbierte gedruckte Originalversion dieser Dissertation ist an der TU Wien Bibliothek verfügbar.
The approved original version of this doctoral thesis is available in print at TU Wien Bibliothek.
TU Bibliothek Your knowledge hub WIEN

isolated features before and after annealing were compared. From a previous study [174] it is known that, after the annealing step, Rh incorporates into the first subsurface layer as single Rh adatoms, which are visible in STM images. Since the number of isolated features remain approximately the same, the Rh features observed after deposition in a water vapor background are attributed to single Rh adatoms. Some of the Rh_1 species appear brighter in STM images, exhibiting an apparent height ≈115 pm greater than most other features. These features alternate between the two apparent heights from one frame to the next. Possible explanations are provided in the discussion.

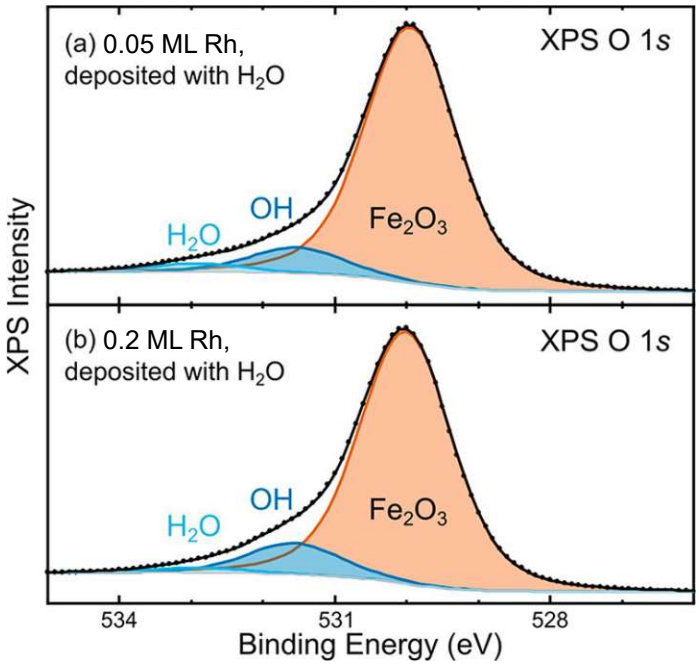

Figure 4.2: XPS spectra of the O 1s region for 0.05 ML Rh (a) and 0.2 ML Rh (b) deposited in a water vapour background of $2 \cdot 10^{-8}$ mbar at room temperature. The data was fitted (solid lines) with the main component correlating to lattice O at 529.9 eV and contributions from molecular H_2O (532.9 eV) and OH (531.5 eV) [93]. Data acquisition and interpretation done by Florian Kraushofer. Reprinted from [159]

XPS spectra were recorded for the Rh 3d region under both UHV and water vapour conditions (Figure 4.1 c)) A core level shift from 307.6 eV for Rh deposition in UHV

Die approbierte gedruckte Originalversion dieser Dissertation ist an der TU Wien Bibliothek verfügbar.
The approved original version of this doctoral thesis is available in print at TU Wien Bibliothek.
TU Bibliothek Your knowledge hub WIEN

to 308.9 eV for Rh deposition in the presence of water vapour was observed. Core level shifts to higher binding energies in XPS are commonly associated with transition from nanoparticles to oxidized metal atoms.
Figure 4.2 shows XPS spectra of the O 1s region for two different Rh coverages deposited in water vapour. The main contribution at 529.9 eV can be attributed to lattice O from the α-$Fe_2O_3(1\bar{1}02)$ surface, with additional contributions from molecular H_2O (532.9 eV) and OH groups (531.5 eV). The H_2O/OH ratio on the as-prepared surface is 0.40 for submonolayer coverages, indicating that 45 % of H_2O is adsorbed molecularly. (For more details see section 1.5.2) [93] Depositing Rh in the presence of water decreases the H_2O/OH ratio to values of 0.32 for 0.05 ML Rh and 0.17 for 0.2 ML Rh. This corresponds to 39 % and 26 % molecular water adsorption, respectively, which is significantly lower than on the as-prepared surface. We conclude that the additional OH groups are adsorbed on the Rh adatoms and stabilize these.

nc-AFM

STM and XPS experiments sufficiently demonstrated that Rh deposited in water leads to isolated Rh adatoms, which are stabilized by OH ligands. However, STM and XPS alone cannot determine the exact number of OH ligands adsorbed on the Rh adatoms or the precise configuration of the $Rh(OH)_x$ species on the α-$Fe_2O_3(1\bar{1}02)$ surface. To gain further insights, nc-AFM experiments were performed due to the superior image resolution compared to STM.
Nc-AFM imaging was conducted at 4 K, using liquid helium as a cryogen. At this temperature, even the Ti doped film loses conductivity, making STM imaging prior to nc-AFM imaging impossible. A CO-functionalised tip was employed.
In the first set of experiments, 0.1 ML Rh was deposited in UHV at 95 K. Isolated dark features between the Fe rows were observed and attributed to Rh adatoms frozen out due to the low temperature during deposition (see Figure 4.3). Given the CO-functionalised tip, the bright rows were assigned to surface O atoms, while the dark rows correspond to surface Fe atoms.
Subsequently, 0.1 ML Rh was deposited in a water vapour background of $2 \cdot 10^{-8}$ mbar at room temperature, and the sample was annealed to 80 °C to desorb any remaining water from the surface (see Figure 4.4 a)). Characteristic zig-zag rows of the α-$Fe_2O_3(1\bar{1}02)$ lattice, highlighted by a blue zig-zag line, are visible. Round dark features with two or three bright protrusions on top are seen on the surface. The

Die approbierte gedruckte Originalversion dieser Dissertation ist an der TU Wien Bibliothek verfügbar.
The approved original version of this doctoral thesis is available in print at TU Wien Bibliothek.
TU Bibliothek Your knowledge hub WIEN

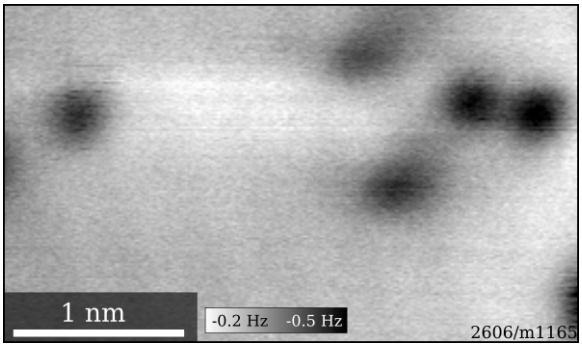

Figure 4.3: Nc-AFM image of the α-$Fe_2O_3(1\bar{1}02)$ surface after deposition of 0.1 ML Rh at 95 K. Dark protrusions between the Fe rows are attributed to Rh_1 species.

dark features are attributed to Rh adatoms, confirmed by the earlier experiment.

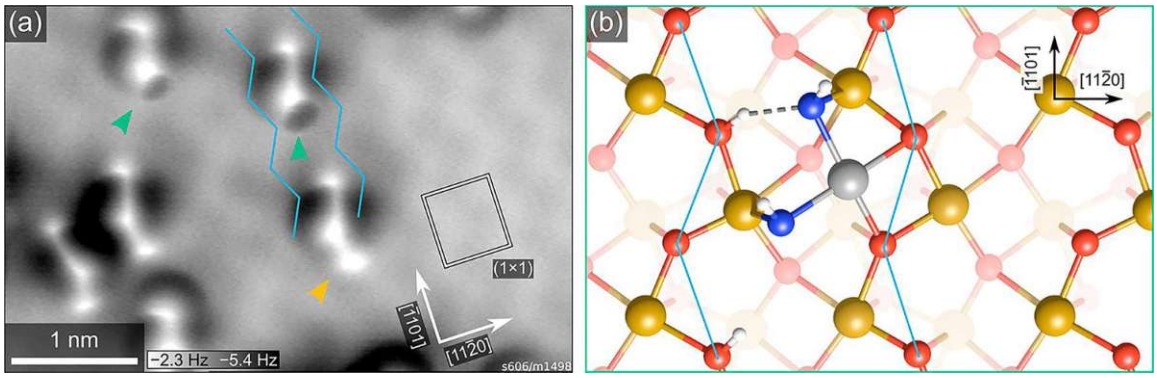

Figure 4.4: Nc-AFM image a) and a schematic model b) of Rh adatoms stabilized by two hydroxyls on the α-$Fe_2O_3(1\bar{1}02)$ surface. O zig-zag rows are marked in blue, both in the nc-AFM image and the schematic model. Some of the Rh adatoms, stabilized by two hydroxyl groups (green arrow), additionally adsorb a water molecule (orange arrow). In the model the Rh adatom is coloured grey and the $O_{hydroxyl}$ blue. Reprinted from [159]

Based on the XPS and nc-AFM results, we conclude that Rh adatoms with two bright features ontop correspond to Rh adatoms stabilized by two hydroxyl groups (indicated by a green arrow in Figure 4.4 a)). A schematic model of the $Rh(OH)_2$ species, derived from the feature positions observed in the nc-AFM image and relaxed by DFT+U, is presented in Figure 4.4 b). We propose that the Rh atom exhibits a

Die approbierte gedruckte Originalversion dieser Dissertation ist an der TU Wien Bibliothek verfügbar.
The approved original version of this doctoral thesis is available in print at TU Wien Bibliothek.
TU Bibliothek Your knowledge hub WIEN

square planar coordination, bound to two O atoms from the surface and to two OH ligand. The OH groups are also bound to the nearest surface Fe atoms. Furthermore, OH adsorbed at surface Fe atoms can form a hydrogen-bond with the O atom of one of the OH groups atop the Rh adatom. These two OH ligands stabilize the Rh adatom in locations where water molecules adsorb at the surface. [93] Therefore, at room temperature, the water molecules on the surface do not have to rearrange in order to accommodate the Rh adatoms.
Occasionally a third bright protrusions (orange arrow in Figure 4.4 a)) appears next to the Rh adatom. We attribute this to an additional water molecule coordinated to a surface Fe atom and hydrogen-bonded to one of the hydroxyl groups.
In the bottom left corner of Figure 4.4 a), two adjacent Rh adatoms each exhibit three bright features on top but appear as mirrored counterparts. The third bright feature, attributed to an additional water molecule, is always positioned below the Rh adatom along the $(\bar{1}101)$ direction. This aligns with the surface structure of α-$Fe_2O_3(1\bar{1}02)$, which has a mirror plane parallel to the $(\bar{1}101)$ direction but not perpendicular to it. Thus, the positions above and below the Rh adatoms along the $(\bar{1}101)$ direction are not equivalent.

Discussion

Overall, the stabilization of Rh adatoms on the α-$Fe_2O_3(1\bar{1}02)$ surface was achieved by introducing water vapour during metal deposition. STM and XPS experiments allowed us to determine the formation of $Rh(OH)_x$ species; however, the exact number of OH ligands responsible for stabilizing the Rh adatoms remained unclear. By using nc-AFM with a CO-terminated tip, it has been demonstrated that two OH ligands are sufficient to stabilize the Rh adatoms. Furthermore, we identified the structure of the $Rh(OH)_2$ species, which adopts a square planar coordination geometry. This geometry has also been observed for CO adsorption on Rh and Ir on the $Fe_3O_4(001)$ surface. [175, 176] The square planar configuration is the preferred geometry for Rh(I) coordination complexes, making this outcome unsurprising.
Two distinct species were identified with nc-AFM: $Rh(OH)_2$ species and $Rh(OH)_2$ species with an additional bright feature adsorbed below the Rh adatom. The additional feature likely corresponds to the presence of molecular water adsorbed at a surface Fe atom, forming a hydrogen-bond with one of the OH ligands on the Rh adatom. RT-STM images show that the apparent height of the Rh adatoms can

Die approbierte gedruckte Originalversion dieser Dissertation ist an der TU Wien Bibliothek verfügbar.
The approved original version of this doctoral thesis is available in print at TU Wien Bibliothek.
TU Bibliothek Your knowledge hub WIEN

switch between two distinct heights, likely due to the adsorption and desorption of molecular water. This dynamic process is suppressed at the low measurement temperature used for nc-AFM, effectively freezing out the adsorption-desorption events. At room temperature, the Rh adatoms may potentially act as a reaction center, unlike the incorporated Rh adatoms formed by annealing in O_2. [174] Analogous to the Wilkinson‘s catalyst, we suggest that binding another ligand while forming a bond to the surface oxygen beneath the Rh adatom could lead to the formation of an octahedral coordination. Switching between square planar and octahedral coordination is a key step in homogeneous Rh-catalysed reactions, such as the hydrogenation of olefins.

In any case, the presence of water plays a crucial role in this system and should not be neglected in model reaction pathways of SACs.

Die approbierte gedruckte Originalversion dieser Dissertation ist an der TU Wien Bibliothek verfügbar.
The approved original version of this doctoral thesis is available in print at TU Wien Bibliothek.
TU Bibliothek Your knowledge hub WIEN

5 Fundamental adsorption studies on the Rh/Fe_3O_4(001) system to gain insight into the model hydroformylation reaction

The ultimate goal of this study was to improve the understanding of the hydroformylation reaction at an atomic level. To achieve this, we utilized a well characterized SAC model system: Rh adatoms on the Fe_3O_4(001) surface.
Several steps were considered prior to the actual reaction. First, we investigated the interaction of the individual reactants (CO, H_2 and an alkene) with the as-prepared Fe_3O_4(001) surface. To simplify the model reaction we utilized C_2H_4. Since the interaction of CO and H_2 with the surface is well-documented in the literature [177–179], we focused on the interaction of C_2H_4 with the surface. Next, the interaction of the individual molecules with Rh adatoms on the Fe_3O_4(001) surface was analysed. Finally, we attempted to achieve co-adsorption of CO and C_2H_4 on the Rh/Fe_3O_4(001) system. Parts of the results of these studies have been published in ref. [133, 134, 180].
The following sections present studies that integrate multiple surface science techniques as well as DFT+U-based calculations. Combining the results from several methods and analysing them together is essential for a complete understanding of the system. XPS and TPD experiments were conducted by Chunlei Wang, and DFT+U-based calculations were performed by Panukorn Sombut.

Die approbierte gedruckte Originalversion dieser Dissertation ist an der TU Wien Bibliothek verfügbar.
The approved original version of this doctoral thesis is available in print at TU Wien Bibliothek.

5.1 Introduction

Model SAC on Fe_3O_4(001)

Fe_3O_4(001) is an ideal model system for studying fundamental processes in SAC due to its ability to stabilize a variety of metal adatoms in an ordered array. [79] In 2012, the stabilization of adatoms on this surface was reported for the first time for Au. It was found that Au forms single dispersed adatoms that are stable against sintering at room temperature, remaining stationary until annealed to 700 K. These adatoms adsorb in a 2-fold coordination to surface O atoms, consistent with the "×" position in Figure 1.15 b) and c) [117] (for more details, see section 1.5.4).

Experiments with Ag and Cu show similar results, though Cu can be stabilized to higher coverages than Au and Ag. At elevated temperatures or high metal coverages, all three metals form clusters on the surface. [181, 182]. DFT+U calculations suggest that Ag and Cu adatoms adopt a 1+ oxidation state, consistent with their oxidation state in Cu_2O and Ag_2O, where the metals bind linearly to O^{2-} anions. [182] Experimental investigations on Ti, Mn, Co and Ni have shown that 3d transition metals also adsorb at the same site as Au but are unstable against incorporation into the lattice. The temperature required for incorporation increases from left to right across the periodic table, with Ti incorporating partially already at room temperature. Above 700 K, none of these metals remain detectable by XPS. [118, 183] For the investigated 4d and 5d transition metals Rh, Pd, Ir, and Pt, 2-fold coordination is also observed, but Rh and Ir prefer to incorporate into octahedral coordination within the lattice. The transition from 2-fold coordination to 5-fold and eventually 6-fold coordination occurs at slightly elevated temperatures, as 6-fold coordination is energetically favourable for Rh and Ir. A few Rh adatoms incorporate into the lattice even at room temperature, indicating that the surface is not perfectly homogeneous. Upon annealing to elevated temperatures, Rh diffuses into the Fe_3O_4 bulk, while Ir forms clusters on the surface. This difference in behaviour is due to the higher oxophilicity and lower cohesive energy of Rh compared to Ir. Pt and Pd remain stable up to a relatively high temperature (700 K) and coverages but are destabilized by CO, leading to mobile PdCO and PtCO species that eventually agglomerate. Figure 5.1 a) shows STM images of eight different metal adatoms on the Fe_3O_4(001) surface. A study on CO adsorption on various metal adatoms on the Fe_3O_4(001) surface shows that CO can either destabilize or strengthen the coordination of the adatom

Die approbierte gedruckte Originalversion dieser Dissertation ist an der TU Wien Bibliothek verfügbar.
The approved original version of this doctoral thesis is available in print at TU Wien Bibliothek.
TU Bibliothek Your knowledge hub WIEN

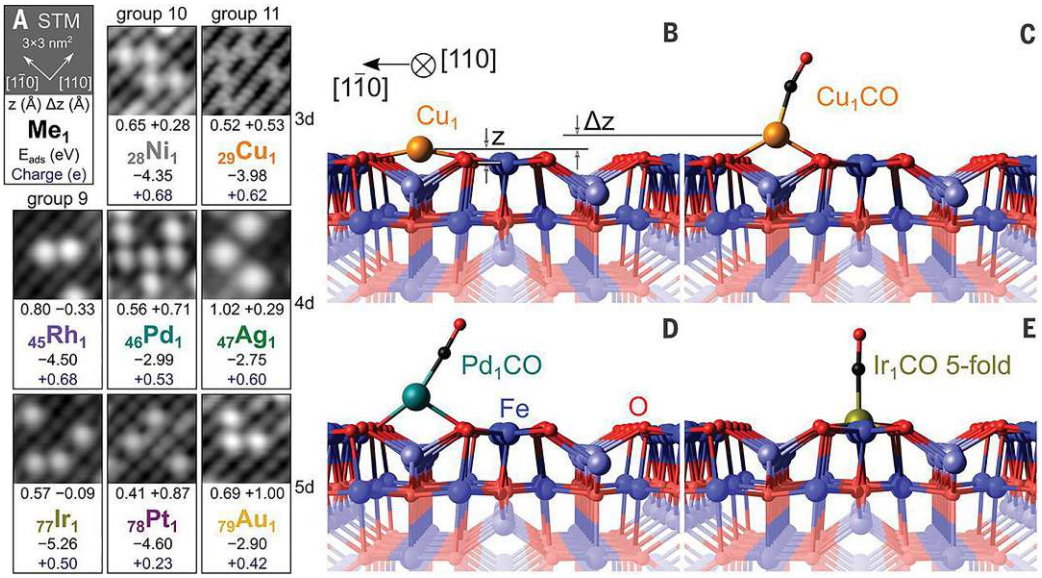

Figure 5.1: a) shows STM images of several metal adatoms adsorbed at the $Fe_3O_4(001)$ surface. In b)–d) DFT+U-based calculations show the minimum energy structure of the 2-fold coordinated metal adatoms with and without adsorbed CO. Cu and Pd adatoms are lifted from the surface after adsorption of CO and are thus destabilized. e) Ir, however, replaces a 5-fold coordinated surface Fe atom at elevated temperatures, meaning that CO desorbs ultimately from a 5-fold coordinated Ir_1 species. Reprinted from [184]

with the lattice. CO competes with the oxide to bind the metal adatom, and strong CO binding can destabilize the adatom on the surface. However, in the case of Rh and Ir, which prefer a square-planar and octahedral structure, CO modifies the 2-fold coordination, thereby stabilizing the adatoms. (see Figure 5.1) Overall, this study demonstrates that the adsorption properties of SACs resemble those of coordination complexes more than those of metal nanoparticles. [184]

The $Rh/Fe_3O_4(001)$ system

Now, I will focus on the $Rh/Fe_3O_4(001)$ system, which was employed in this study on the model hydroformylation reaction.

As mentioned earlier, Rh adatoms are initially 2-fold coordinated to O between the Fe_{oct} rows after deposition at room temperature (Figure 5.2 a) red circle). In addition,

Die approbierte gedruckte Originalversion dieser Dissertation ist an der TU Wien Bibliothek verfügbar.
The approved original version of this doctoral thesis is available in print at TU Wien Bibliothek.
TU Bibliothek Your knowledge hub WIEN

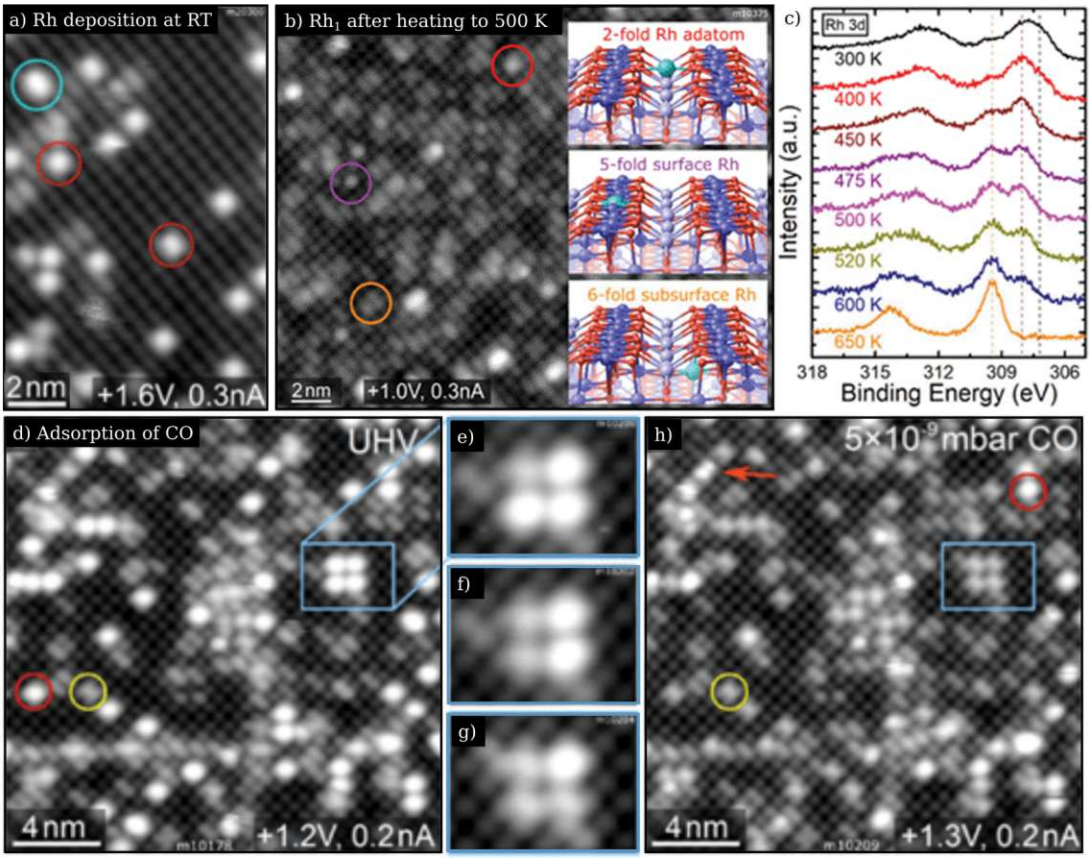

Figure 5.2: STM images and XPS measurements of the $Rh/Fe_3O_4(001)$ system. a) shows the surface after Rh deposition at room temperature, and b) after annealing the sample to 500 K. Red, purple, and orange circles mark the 2-fold, 5-fold and 6-fold coordinated Rh adatoms, whereas 5-fold and 6-fold coordination only occurs after annealing above 450 K. Models of the three different adsorption environments are shown in the inset of b). c) displays XPS spectra of the Rh 3d region recorded over a temperature series. Due to incorporation of Rh, a peak shift to higher binding energy is observed from 307.7 eV to 308.0 eV at 450 K and finally to 309.5 eV at 650 K. d)–h) show the interaction of Rh_1 species with CO. During exposure to $5{\cdot}10^{-9}$ mbar CO, the apparent height of Rh_1 species decreases from ≈180 pm (red circle) to 95–125 pm (yellow circle). A small amount of $Rh(CO)_2$ can also be observed (red arrow). Adapted from [176]

Die approbierte gedruckte Originalversion dieser Dissertation ist an der TU Wien Bibliothek verfügbar.
The approved original version of this doctoral thesis is available in print at TU Wien Bibliothek.
TU Bibliothek Your knowledge hub WIEN

elongated larger features are visible between the Fe_{oct} rows, assigned to metastable Rh_2 dimers (cyan circle), which exhibit a hopping motion at the adsorption site. These can be split into two Rh adatoms by bias pulsing. No further mobility of the Rh species is observed at room temperature. [176]
Figure 5.2 b) shows the surface after annealing to 500 K. Rh adatoms substitute a 5-fold coordinated surface Fe_{oct} (purple circle) and eventually incorporate into the subsurface 6-fold coordinated (orange circle). Models of the three different adsorption sites are shown in the inset of Figure 5.2 b). The XPS data confirm this incorporation process, as indicated by the shift of the Rh 3d peak to higher binding energies; from initially 307.7 eV to 308.0 eV at 450 K, and finally to 309.5 eV at 650 K (Figure 5.1 c)). After annealing to higher temperatures, the Rh signal diminishes, indicating Rh diffusion into the Fe_3O_4 bulk.

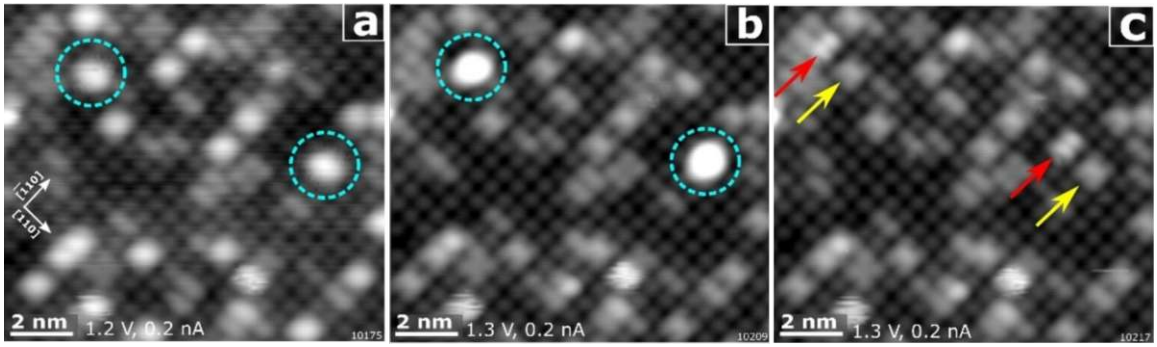

Figure 5.3: STM images of the CO-induced breakup of Rh_2 dimers into Rh monocarbonly Rh_1CO and Rh gem di-carbonly $Rh_1(CO)_2$. Over the course of the whole STM movie 17 L CO was dosed into the UHV chamber. Dashed cyan circles highlight the Rh_2 dimers in a) before, and the $Rh_2(CO)_x$ species after CO adsorption b). The resulting $Rh_1(CO)_2$ is highlighted with red arrows and the Rh_1CO species with a yellow arrow. Adapted from [180]

Figure 5.2 d)–h) displays a sequence of STM images recorded under a CO pressure of $5 \cdot 10^{-9}$ mbar. Adsorption of CO can be observed by an abrupt decrease in apparent height of the Rh_1 species from ≈180 pm (red circle) to 95–125 pm (yellow circle). The reduction in apparent height is due to the modification of unoccupied Rh states near the Fermi level, caused by interaction with CO. The features in the yellow circle are attributed to monocarbonyl RhCO species. A red arrow marks a rarely occurring

Die approbierte gedruckte Originalversion dieser Dissertation ist an der TU Wien Bibliothek verfügbar.
The approved original version of this doctoral thesis is available in print at TU Wien Bibliothek.
TU Bibliothek Your knowledge hub WIEN

double feature, which is assigned to a $Rh(CO)_2$ di-carbonyl. [176]
A very recent study showed that these Rh gem di-carbonyl species do not form directly on the 2-fold coordinated Rh adatoms, but rather due to a CO-induced breakup of a Rh_2 dimer. [180] Figure 5.3 shows the gem di-carbonyl formation process. In a), two dimers are shown (dashed cyan circle), which adsorb CO to form $Rh_2(CO)_x$ species as shown in b) (dashed cyan circle). Subsequently a Rh_1CO (yellow arrow) and a $Rh_1(CO)_2$ gem di-carbonyl is formed (red arrow).

Hydroformylation

Hydroformylation is an industrial process that synthesizes aldehydes (R-CH=O) from alkenes ($R_2C{=}CR_2$) and syngas, a mixture of CO and H_2 (see Figure 5.4). This reaction involves the addition of a formyl group (-CHO) and a hydrogen atom to a carbon-carbon double bond. A mixture of isomeric products is typically formed, except when C_2H_4 is used as the reactant. Even a single terminal olefin can produce various branched aldehydes, making regioselectivity an important aspect. Figure 5.5 outlines the reaction pathways when C_2H_4 is used as a reactant.

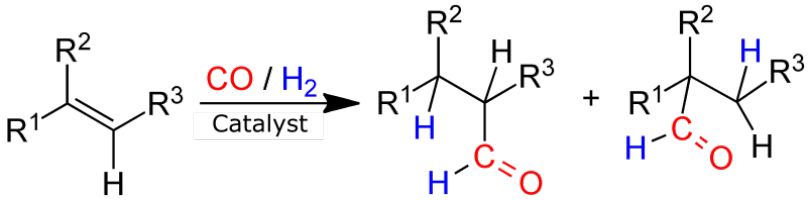

Figure 5.4: The hydroformylation reaction. Alkenes ($R_2C{=}CR_2$) and syngas (CO and H_2) are catalytically converted into aldehydes (R-CH=O). Reprinted from [185]

Hydroformylation was discovered in 1938 and is one of the key achievements in 20^{th}-century catalysis. Today, it remains one of the largest homogeneously catalysed industrial reactions. [187–190] Aldehydes are important products and intermediates in the synthesis of chemicals such as alcohols, esters, and amines. Various transition metals can catalyse the hydroformylation reaction, but only Rh and Co are industrially relevant. Phosphine-and phosphite-modified Rh complexes are predominantly used, due to their high activity and mild reaction conditions. However, Rh's high price presents a significant challenge.
In the field of SAC, numerous studies have focused on the hydroformylation reaction

Die approbierte gedruckte Originalversion dieser Dissertation ist an der TU Wien Bibliothek verfügbar.
The approved original version of this doctoral thesis is available in print at TU Wien Bibliothek.
TU Bibliothek Your knowledge hub WIEN

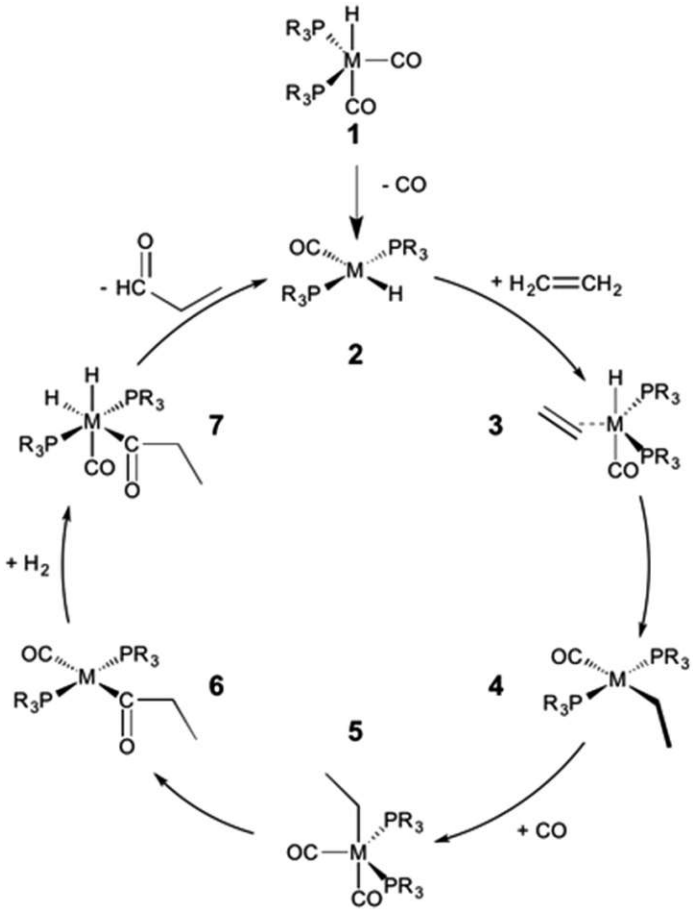

Figure 5.5: Mechanism for the Rh-catalyzed hydroformylation of an olefin. M = Rh, R = Ph. Reprinted from [186]

using single Rh atoms supported on various materials. In 2016 Lang et al. demonstrated that Rh SACs on ZnO nanowires show a similar efficiency compared to that of homogeneous Wilkinson's catalyst and are one to two orders of magnitude more active than most of the reported heterogeneous catalysts, while being reusable up to four times without significant loss of selectivity and reactivity. [191] Amsler et al. found that Rh_1/CeO_2 exhibited high activity in the hydroformylation reaction, similar to a $HRh(PPh_3)_3CO$ molecular catalyst, without significant Rh leaching. [192] Gao et al. showed that Rh_1 supported on nanodiamond exhibit excellent activity and regioselectivity in hydroformylation of arylethylenes, with the synthesis of Ibuprofen and Fendiline being achieved with high yields and efficiency. [193] Recent studies

Die approbierte gedruckte Originalversion dieser Dissertation ist an der TU Wien Bibliothek verfügbar.
The approved original version of this doctoral thesis is available in print at TU Wien Bibliothek.

in 2023 have demonstrated further advancements with the Rh_1/CeO_2 system [194, 195], with research also expanding to new systems such as Rh_1/SnO_2 [196] and single Rh atoms dispersed over graphitic carbon nitride [197]. The growing number of publications highlights the increasing significance of this topic.

Die approbierte gedruckte Originalversion dieser Dissertation ist an der TU Wien Bibliothek verfügbar.
The approved original version of this doctoral thesis is available in print at TU Wien Bibliothek.

5.2 C_2H_4 adsorption on Fe_3O_4(001)

In this section I present a multi-technique study focusing on the interaction of C_2H_4 with the Fe_3O_4(001) surface.

STM

Imaging was performed at the LT-STM with liquid nitrogen as a cryogen, maintaining a sample temperature of 78 K during imaging. C_2H_4 was dosed into the analysis chamber through an open door in the thermal shield of the liquid-nitrogen-cooled STM head. Different pressures were used, with a maximum of $5 \cdot 10^{-9}$ mbar.

Figure 5.6 a) shows a representative STM image of the Fe_3O_4(001) surface, displaying the most common surface defects (for more details of the as-prepared surface, see section 1.5.4). Figure 5.6 b)–d) show the Fe_3O_4(001) surface with different coverages of adsorbed C_2H_4 molecules. In Figure 5.6 b), the sample was exposed to 0.5 L C_2H_4 at 78 K. Due to dosing C_2H_4 through a small window, the actual exposure is likely less than the nominal dose. In the top-left of the STM image, a line of protrusions is visible, attributed to C_2H_4 adsorption on an APDB. This behaviour is not surprising, as APDB have previously been shown to be active for CH_3OH adsorption at room temperature. [122] Additionally, adsorption at two distinct sites on the surface is observed. Isolated bright features (highlighted with a cyan circle) are positioned above the Fe rows, corresponding to adsorption atop a 5-fold coordinated surface Fe atom in a regular lattice position. A potential adsorption mechanism at this site could involve C_2H_4 adsorbing near an OH group [198], but since many OH groups remain visible after dosing C_2H_4, it is likely that C_2H_4 adsorption occurs at another defect, likely an unreconstructed unit cell. [122] This defect occurs when an additional Fe atom is accommodated in the subsurface. Isolated bright features (orange circle) are positioned between the surface Fe rows, corresponding to adsorption at a 2-fold coordinated Fe adatom defect. The streakiness in the image suggests that C_2H_4 is diffusing across the Fe_3O_4(001) surface at this temperature, during the STM measurements.

In Figure 5.6 c), after exposure to 5 L C_2H_4, bright protrusions similar to those in Figure 5.6 b), are visible at the Fe rows. Patches of protrusions, with a nearest-neighbour distance of 6 Å, cover the surface. The nearest-neighbour distance of surface Fe atoms along the Fe rows is 3 Å, indicating that every other Fe surface

Die approbierte gedruckte Originalversion dieser Dissertation ist an der TU Wien Bibliothek verfügbar.
The approved original version of this doctoral thesis is available in print at TU Wien Bibliothek.
TU Bibliothek Your knowledge hub WIEN

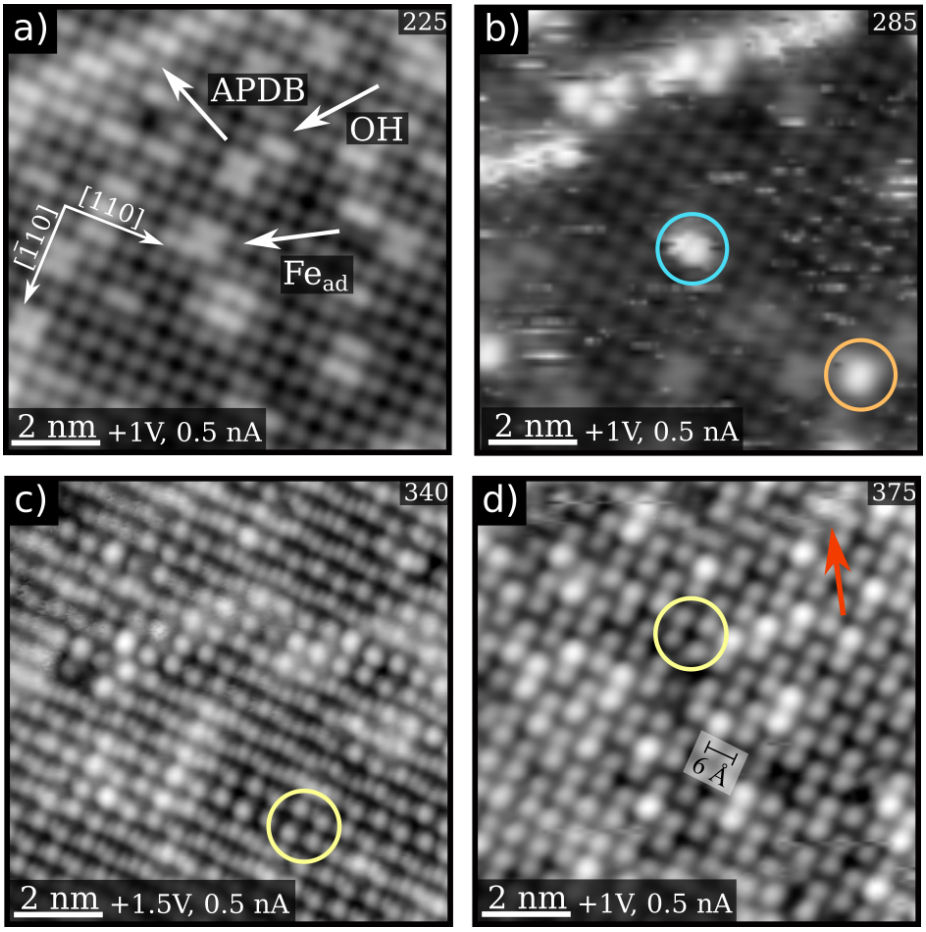

Figure 5.6: LT-STM images of the $Fe_3O_4(001)$ surface before and after exposure to C_2H_4. In a)–c) imaging was conducted at 78 K, in d) at 68 K. a) shows the as-prepared surface and its typical surface defects. b) After exposure to 0.5 L C_2H_4 at 78 K only surface defects are occupied by C_2H_4. c) After exposure to 5 L C_2H_4. The surface consists of patches of C_2H_4, that are ordered locally with a nearest-neighbour distance of 6 Å, and patches of visible Fe rows. d) After lowering the sample temperature and exposing the surface to further 2.3 L of C_2H_4. A full coverage of bright protrusions with a nearest-neighbour distance of 6 Å is visible along the [110] direction.

atom is occupied by a C_2H_4 molecule. In some areas, the underlying Fe rows remain visible. Adsorption of a C_2H_4 molecule on the STM tip likely enhances resolution,

Die approbierte gedruckte Originalversion dieser Dissertation ist an der TU Wien Bibliothek verfügbar.
The approved original version of this doctoral thesis is available in print at TU Wien Bibliothek.
TU Bibliothek Your knowledge hub WIEN

allowing for the clear visualization of individual surface Fe atoms. Under standard resolution conditions, only pairs of Fe atoms along the Fe row direction are typically observed. A gradual transition between the patches of adsorbed C_2H_4 molecules and regions of unoccupied Fe rows is observed. The C_2H_4 molecules are strongest adsorbed on surface defects, as seen in b), and the mobility of the species increases with distance from the defects. The timescale of molecule diffusion is shorter than the STM imaging, resulting in a smeared appearance at the edges of the C_2H_4 patches. Even at a high dose of 5 L, the surface is not fully covered by C_2H_4 molecules, indicating that the surface temperature is too high to stabilize a full coverage of C_2H_4 molecules with a nearest-neighbour distance of 6 Å, at the given pressure regime. Therefore, the temperature was reduced by pumping the cryogen out of the cryostat, lowering the sample temperature to ≈68 K. After dosing an additional 2.3 L of C_2H_4 at this lower temperature, the surface Fe rows are no longer visible and a complete layer of circular protrusion with a next nearest-neighbour distance of 6 Å is observed (see Figure 5.6 d)). Even though the molecules are as closely packed as possible occasional mobility is still visible (marked with a red arrow).

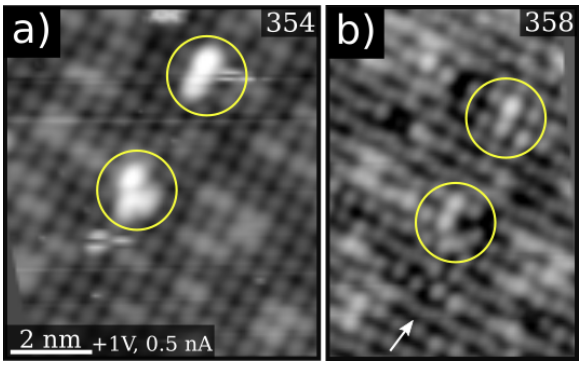

Figure 5.7: LT-STM images of the $Fe_3O_4(001)$ surface during exposure to C_2H_4 at 78 K. In a) solely defect sites are occupied by C_2H_4 (marked with a yellow circle), while in b), also Fe^{3+} sites start to adsorb C_2H_4. C_2H_4 adsorbed at regular lattice sites appear less bright than C_2H_4 adsorbed at defect sites. Some surface Fe atoms remain visible, which are thus not occupied by C_2H_4 molecules (marked with an arrow).

Some C_2H_4 molecules appear brighter than others. To determine the difference between the two species, STM imaging during exposure to C_2H_4 was conducted. Fig-

Die approbierte gedruckte Originalversion dieser Dissertation ist an der TU Wien Bibliothek verfügbar.
The approved original version of this doctoral thesis is available in print at TU Wien Bibliothek.
TU Bibliothek Your knowledge hub WIEN

ure 5.7 shows two STM images of the same area, where in a) C_2H_4 are only adsorbed at defect sites (highlighted with a yellow circle) while in b) C_2H_4 adsorption can also be observed at regular lattice sites (after a larger amount of C_2H_4 was dosed onto the surface). The C_2H_4 molecules at the defect sites (yellow circle) appear brighter than the C_2H_4 molecules on the regular lattice sites. Additionally, a quantitative analysis of the concentration of surface defects before C_2H_4 exposure, as well as the number of brighter features after exposure, was conducted. This analysis confirms the earlier assumption that C_2H_4 adsorbed on defect sites appear brighter in STM images at the given imaging conditions.
Stabilization of higher coverages would require further cooling the sample. While this could be achieved by using liquid helium as a cryogen, at a temperature as low as 4 K, the Fe_3O_4 sample is not sufficiently conductive for STM measurements.

TPD

Figure 5.8 shows a series of TPD spectra for different initial C_2H_4 coverages (0.3–12.7 molecules per $(\sqrt{2}\times\sqrt{2})$R45° unit cell), revealing a total of 7 desorption features corresponding to molecular desorption of C_2H_4 from the Fe_3O_4(001) surface. Peaks labelled α and β (in the range of 70–75 K) are attributed to C_2H_4 multilayer desorption, while the higher temperature peaks, γ–η, are attributed to the first monolayer. Another peak at 215 K can also be recognized but was attributed to desorption from the Ta backplate. Similar TPD results have been reported by Lee et al. [199], though their study did not observe the α, β, γ peaks or the shoulder of ζ, due to a higher sample temperature during C_2H_4 exposure.
At the lowest exposure (0.3 molecules per unit cell, corresponding to 0.075 molecules per surface Fe atom), the η peak at ≈160 K and the onset of the ζ shoulder are observed. These are attributed to desorption from defects. Typically for a strong binding defect site, the η peak saturates at a low coverage and remains at this intensity with increasing coverage, while the ζ shoulder at ≈130 K exhibits an unusual behaviour. It varies in intensity between samples (it is almost invisible with a completely new sample), and does not fully saturate before the onset of the ε peak. This behaviour will be discussed in more detail in the discussion section. Exclusive titration of defect sites at a low coverage in the STM images (seen in Figure 5.6 b)), as well as the facile diffusion at 78 K, is consistent with results from the TPD experiments. At 115–120 K the ε peak arises, shifting to lower temperatures with increasing cov-

Die approbierte gedruckte Originalversion dieser Dissertation ist an der TU Wien Bibliothek verfügbar.
The approved original version of this doctoral thesis is available in print at TU Wien Bibliothek.
TU Bibliothek Your knowledge hub WIEN

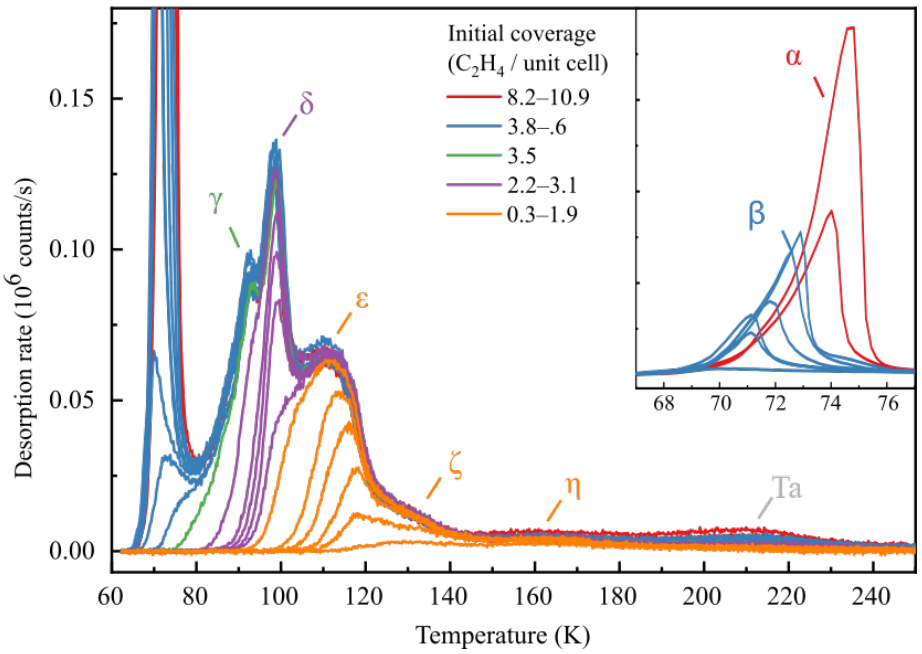

Figure 5.8: TPD spectra for C_2H_4 coverages from 0–12.7 molecules per $Fe_3O_4(001)$ surface unit cell were obtained using a molecular beam to dose C_2H_4 at 60 K. A temperature ramp of 1 K/s was used to acquire the spectra. Seven desorption peaks, labelled α–η arise from desorption of C_2H_4. Additionally, a feature at 215 K is attributed to C_2H_4 desorption from the Ta sample plate. The ζ and η peaks are caused by adsorption on surface defects, while peaks γ–ε emerge from the first monolayer, and α and β from multilayer desorption.

erage and saturating at 110–115 K with a coverage of 2.2 ($\pm$ 0.2) C_2H_4 per unit cell. The sharp δ and γ peaks saturate close to 3.0 ($\pm$ 0.3) and 4.1 ($\pm$ 0.4) C_2H_4 per unit cell, respectively. The full coverage of two C_2H_4 per unit cell observed in STM (Figure 5.6 d)) corresponds to the ε peak. The sample temperature of 78 K in the STM experiments is near the onset of the desorption peak, explaining why full coverage of two C_2H_4 molecules per unit cell is not achieved, since the timescale of the STM measurements is significantly longer compared to that of the TPD measurements.
The multilayer region consists of the α and β peaks. (inset in Figure 5.8). The

Die approbierte gedruckte Originalversion dieser Dissertation ist an der TU Wien Bibliothek verfügbar.
The approved original version of this doctoral thesis is available in print at TU Wien Bibliothek.

β peak saturates at a coverage of 8.4 ($\pm$ 0.8) C_2H_4 per unit cell, equivalent to $\approx$2 layers of C_2H_4. At higher coverages, the β peak is replaced by the α peak, which increases in intensity with increasing coverage, exhibiting a zero-order profile, typical for multilayer desorption. A new analysis program [130] was utilized to further analyse the TPD data and determine the adsorption energies (more details can be found in [133]). The results are summarized in Table 5.1. There is good agreement between the experimental data and simulation for the ε peak, while for the γ, δ and ζ peaks, a slight deviation between experimental and simulation is observed. This effect will be addressed in the discussion.

XPS

Figure 5.9 shows XPS spectra of the C 1s area. First, the as-prepared Fe_3O_4(001) surface was measured (red curve), and no detectable C 1s peak was observed. After exposure to 12.7 C_2H_4 molecules per unit cell at 61 K, a peak at 284.8 eV appears due to multilayer adsorption of C_2H_4 (blue curve). A second peak, shifted by 8.3 eV to higher binding energies, is attributed to a π-3p Rydberg shake-up process. [200–203] (see Figure 5.10 a))

Subsequently, the sample was heated stepwise to 500 K. After annealing to 80 K (green curve), the intensity of the C 1s peak decreases, and the area of the peak is reduced by 50 %. Further annealing results in desorption of C_2H_4 molecules from the first monolayer, and after annealing to 100 K (orange curve), the C 1s peak corresponds to half a monolayer, i.e. two C_2H_4 molecules per unit cell, consistent with the experimental results from TPD and STM. After annealing to 145 K (yellow curve), only C_2H_4 molecules adsorbed at defect sites remain on the surface. At 500 K (brown curve), no detectable C 1s peak is observed, confirming complete desorption. Throughout the temperature series, the C 1s binding energy remains almost constant, indicating that C_2H_4 is adsorbed molecularly. Only a slight shift in binding energy occurs from the peak at two C_2H_4 molecules per unit cell (100 K, orange curve) to the full monolayer peak (80 K and 90 K, green and purple curve) as well as to the defect related peak (145 K, yellow curve).

Figure 5.10 b) and c) show the Fe 2p and O 1s region, respectively. After C_2H_4 adsorption, the intensity of both peaks decreases slightly, otherwise the signal remains identical to that of the as-prepared Fe_3O_4(001) surface.

Die approbierte gedruckte Originalversion dieser Dissertation ist an der TU Wien Bibliothek verfügbar.
The approved original version of this doctoral thesis is available in print at TU Wien Bibliothek.
TU Bibliothek Your knowledge hub WIEN

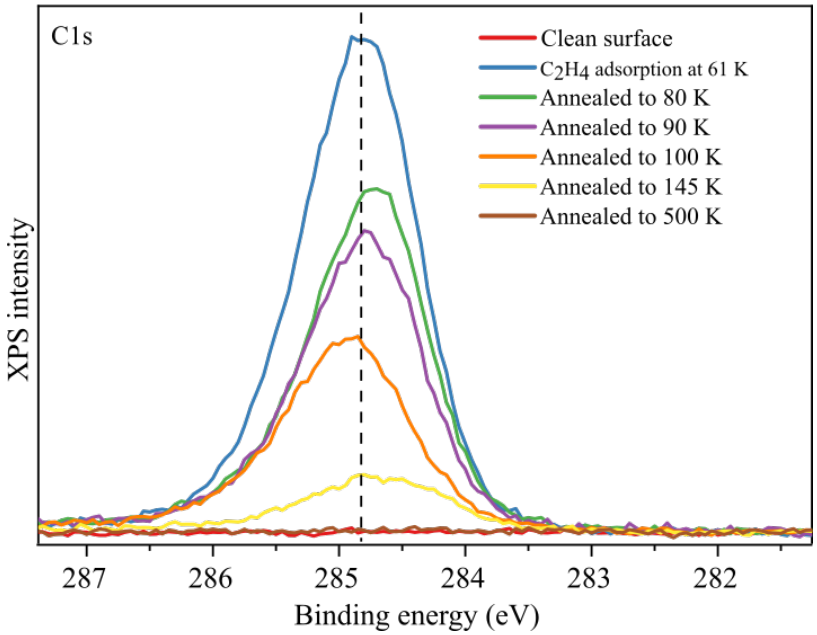

Figure 5.9: XPS spectra of the C 1s region before and after C_2H_4 adsorption on $Fe_3O_4(001)$ measured at 61 K with Al Kα radiation in grazing emission (12° from normal). No C 1s peak can be detected on the as-prepared surface (red curve). Adsorbing 12.7 C_2H_4 per unit cell exhibits a C 1s peak at 284.4 eV, which is a typical binding energy for a C = C double bond (blue curve). The green, purple, orange, and yellow curve show that the intensity of the C 1s peak decrease with increasing temperature i.e. decreasing C_2H_4 coverage. A shift to lower binding energy (248.7 eV) is observed between multilayer (blue curve) and monolayer coverage (green curve). At 500 K (brown curve) no C 1s signal is detectable anymore.

DFT+U

Different configurations of one to four C_2H_4 per unit cell as well as adsorption on three common surface defects on a $(2\sqrt{2}\times2\sqrt{2})R45°$ supercell of the $Fe_3O_4(001)$ surface were analysed and the lowest-energy configuration of C_2H_4 for each coverage was determined. The strongly constrained and appropriately normed meta-generalized gradient approximation (SCAN) with the inclusion of van der Waals interactions (rVV10) was utilized, due to its good performance on molecular and solid-state test sets [204, 205], as well as a balanced accuracy and computational efficiency. [206]

Die approbierte gedruckte Originalversion dieser Dissertation ist an der TU Wien Bibliothek verfügbar.
The approved original version of this doctoral thesis is available in print at TU Wien Bibliothek.

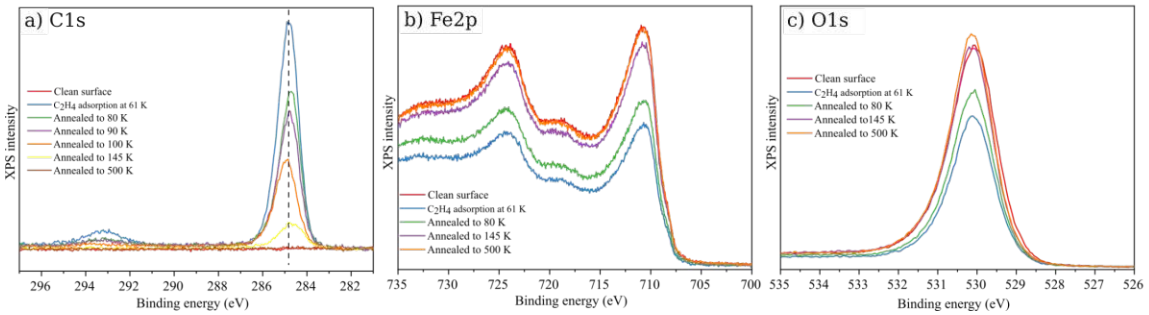

Figure 5.10: XPS spectra of the $Fe_3O_4(001)$ surface before and after adsorption of C_2H_4, and subsequent annealing to 500 K. a) shows the C 1s region with an additional peak due to a π-3p Rydberg shake-up process, b) the Fe 2p region and c) the O 1s region.

For coverages exceeding one molecule per unit cell, the calculated adsorption energy corresponds to the average adsorption energy per C_2H_4 molecule.

Figure 5.11 shows low-coverage adsorption configurations. Similar to previous calculations for C_2H_4 on $RuO_2(110)$ [207] and rutile $TiO_2(110)$ [208], where bonding via the π orbital takes place, isolated C_2H_4 molecules adsorb molecularly on the defect-free $Fe_3O_4(001)$ surface, atop a Fe_{oct} site in a flat geometry. The C = C bond can be oriented either along ($E_{ads} = -0.48$ eV) or perpendicular ($E_{ads} = -0.47$ eV) to the Fe rows. With increasing coverage (one C_2H_4/unit cell), van der Waals interaction arise between neighbouring molecules, leading to slightly stronger adsorption energies for both the parallel ($E_{ads} = -0.51$ eV) and perpendicular ($E_{ads} = -0.49$ eV) orientations.

Figure 5.12 shows configurations for two C_2H_4/unit cell. The strongest occurs when the C = C double bond is oriented perpendicular to the Fe row ($E_{ads} = -0.49$ eV; Figure 5.12 a) and b)). Orientation parallel to the Fe row results in a weaker adsorption energy ($E_{ads} = -0.46$ eV; Figure 5.12 c)).

Figure 5.13 shows configurations of three C_2H_4/unit cell. When three C_2H_4 molecules are placed onto the Fe rows, repulsive interactions arise, and the molecules tilt away form the Fe_{oct}, leading to a significantly weaker adsorption. ($E_{ads} = -0.39$ eV; Figure 5.13 b) and c)). However, when the Fe rows are half occupied and the additional C_2H_4 molecule is placed in between the Fe rows, adsorption is stronger ($E_{ads} = -0.47$ eV; Figure 5.13 a)).

Die approbierte gedruckte Originalversion dieser Dissertation ist an der TU Wien Bibliothek verfügbar.
The approved original version of this doctoral thesis is available in print at TU Wien Bibliothek.
TU Bibliothek Your knowledge hub WIEN

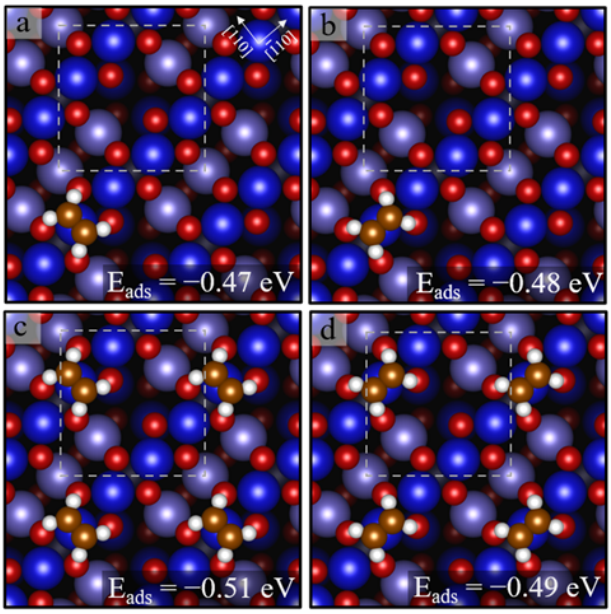

Figure 5.11: DFT+U-based calculations for low coverage adsorption of C_2H_4 on the defect-free $Fe_3O_4(001)$ surface. a) and b) show configuration for isolated C_2H_4 molecules, c) and d) for one C_2H_4/unit cell. Fe_{oct} are displayed in dark blue, Fe_{tet} in light blue and O atoms in red, the dashed square shows the unit cell.

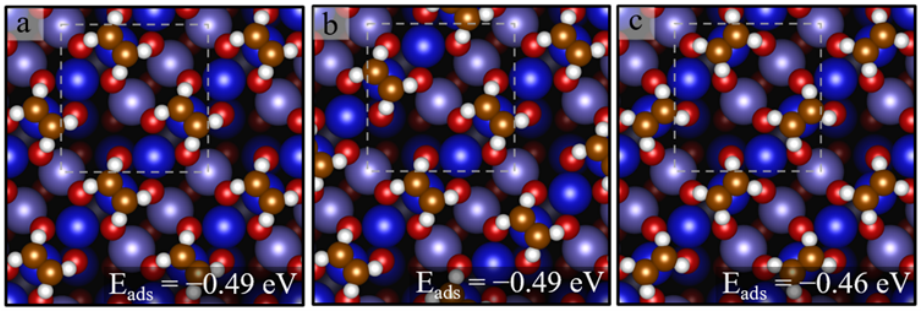

Figure 5.12: DFT+U-based calculations for two C_2H_4/unit cell on the defect-free $Fe_3O_4(001)$ surface. Configurations in a) and b) are oriented perpendicular to the Fe row, in c) parallel to the Fe row.

Due to the large number of possible configurations of four C_2H_4/unit cell, finding the optimal structure was challenging. However, the calculations showed that when two molecules adsorb atop a Fe_{oct} and two molecules adsorb weakly between the Fe

Die approbierte gedruckte Originalversion dieser Dissertation ist an der TU Wien Bibliothek verfügbar.
The approved original version of this doctoral thesis is available in print at TU Wien Bibliothek.
TU Bibliothek Your knowledge hub WIEN

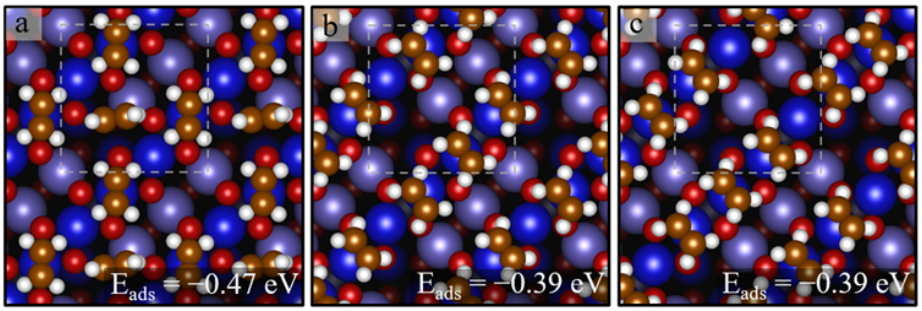

Figure 5.13: DFT+U-based calculations for three C_2H_4/unit cell on the defect-free $Fe_3O_4(001)$ surface. In a) two molecules are adsorbed on the Fe rows, the third one is placed between the rows. In b) and c) three molecules are placed on the Fe rows.

rows, a stable configuration can be achieved. Figure 5.14 a) and b) show two possible structures. Placing all four molecules atop Fe_{oct} sites results in a weaker adsorbed structure (Figure 5.14 c). Thus, it becomes clear that two C_2H_4/unit cell create a threshold and that adding more molecules leads to weakly bound configurations between the Fe rows.

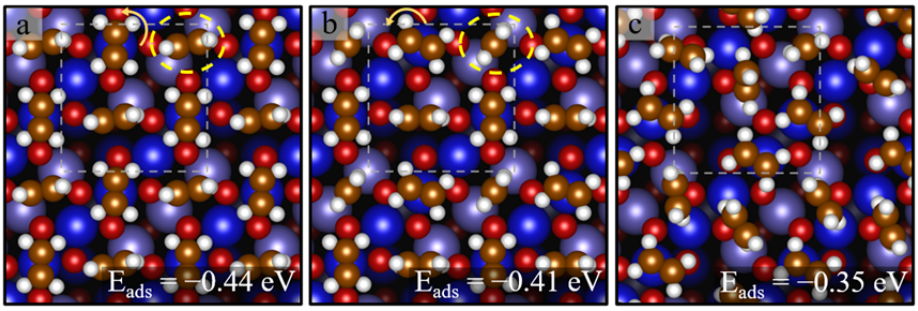

Figure 5.14: DFT+U-based calculations for four C_2H_4/unit cell on the defect-free $Fe_3O_4(001)$ surface. a) and b) shows configurations with two C_2H_4 molecules adsorbed atop Fe_{oct} sites and the two other molecules adsorbed between the Fe rows. In c) all four molecules were initially placed atop Fe_{oct} sites, but moved away due to repulsive interactions.

In addition to calculating adsorption energies, the C 1s core-level binding energy in the final state was approximated. A shift of 0.3 eV was found between C_2H_4 molecules adsorbed atop a Fe_{oct} and C_2H_4 adsorbed between the Fe rows, quantitatively con-

Die approbierte gedruckte Originalversion dieser Dissertation ist an der TU Wien Bibliothek verfügbar.
The approved original version of this doctoral thesis is available in print at TU Wien Bibliothek.
TU Bibliothek Your knowledge hub WIEN

sistent with experimental data, though the sensitivity on the calculations is limited. The final configurations calculated were C_2H_4 molecules adsorbed at common surface defect. (Common surface defects are shown in Figure 5.6 a)) The strongest adsorption energy was found for C_2H_4 adsorbed atop a Fe adatom defect ($E_{ads} = -0.84$ eV), with the C = C double bond parallel to the Fe rows (Figure 5.15 a)). Adsorption at an "unreconstructed unit cell", where a local recovery of the bulk spinel structure occurs by replacing a Fe_{int} atom in the second layer with two Fe_{oct} atoms in the third layer, is shown in Figure 5.15 b). ($E_{ads} = -0.66$ eV) This defect is locally similar to an APDB, thus it was concluded that the adsorption energy at the APDB is likely similar to the adsorption energy at the "unreconstructed unit cell". Figure 5.15 c) shows a C_2H_4 molecule adsorbed adjacent to a hydroxyl group. The adsorption energy was found to be relatively weak ($E_{ads} = -0.47$ eV).

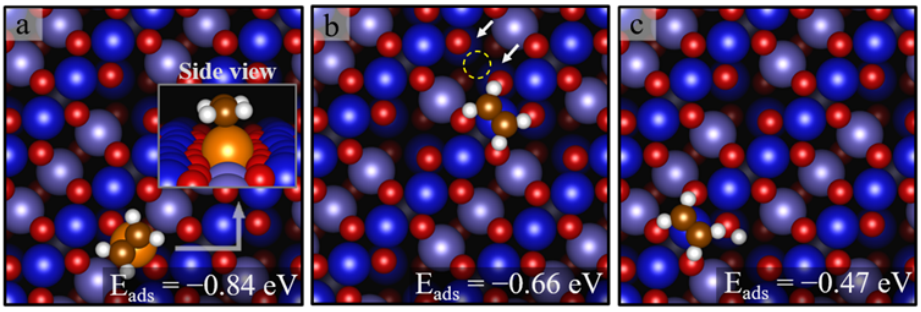

Figure 5.15: DFT+U-based calculations for C_2H_4 adsorption on common defects on the $Fe_3O_4(001)$ surface. In a) C_2H_4 adsorption on a Fe adatom, in b) in an "unreconstructed unit cell" and in c) adjacent to a hydroxyl group is shown. The arrows in b) mark the position of the additional two Fe_{oct} atoms from the third layer.

Table 5.1 summarizes the experimental data from TPD, the adsorption energies determined from the TPD anaylsis, and the adsorption energies calculated by DFT+U. The DFT+U calculations (SCAN + rVV10) yield adsorption energies ≈0.1–0.15 eV stronger than those from the TPD analysis, likely due to the limited accuracy of the vdW functionals. The last column shows adsorption energies from a previous TPD study [199] using the inversion analysis. The desorption temperatures and energies for the δ and ε peak agree well between both TPD analysis methods, though there are some differences for the η peak, likely due to the large error bars, resulting from

Die approbierte gedruckte Originalversion dieser Dissertation ist an der TU Wien Bibliothek verfügbar.
The approved original version of this doctoral thesis is available in print at TU Wien Bibliothek.
TU Bibliothek Your knowledge hub WIEN

the not so well defined peak.

TPD peaks	description	C_2H_4/unit cell saturation	desorption temperature (K)	TPD-Analysis $E_{ads,d}$ (eV)	$E_{ads,d}$ from DFT (SCAN + rVV10) (eV)	inversion analysis in [199] $E_{des,d}$ (eV)
α	multilayer	12.7 (±1.2)	73–76			
β	multilayer	8.9 (±0.8)	70–73			
γ	saturated monolayer	4.1 (±0.4)	90	-0.23	-0.35	
δ	3/4 monolaye	3.0 (±0.3)	100	-0.32	-0.43	0.34
ε	1/2 / 1/4 monolayer	2.2 (±0.2)	110–115	-0.36/-0.40	-0.47/-0.51	0.37/0.42
η	defects	≈0.3	160	-0.54/≈-0.6	-0.66/-0.84	≈0.51

Table 5.1: Summary of experimental and computational data of all desorption peaks arising from C_2H_4 desorption from the Fe_3O_4(001) surface.

Discussion

Overall, combining all experimental and computational results from this multi-technique study successfully elucidates the interaction of C_2H_4 with the Fe_3O_4(001) surface. We have shown that C_2H_4 binds strongly at surface defects such as Fe adatoms, "unreconstructed unit cells", and APDB´s, as clearly observed in the STM images (Figure 5.6 b)). In TPD, the η peak and part of the ζ correspond to C_2H_4 desorption from defects, while DFT+U-based calculations confirm strong adsorption at Fe adatoms and in "unreconstructed unit cells". Adsorption at APDBs was not explicitly calculated but is likely comparable to that of an "unreconstructed unit cell" due to their locally similar structure. Adsorption adjacent to a hydroxyl group is not favoured from DFT+U calculation. Quantitative analysis of hydroxyl groups on the Fe rows in STM images, before and after C_2H_4 adsorption, shows no significant difference, further suggesting that C_2H_4 is not preferentially adsorbed next to a hydroxyl group. I want to take a closer look at the unusual behaviour of the ζ peak, which was also addressed by Lee et al. [199]. The ζ peak continues to grow even after the onset of the ε peak, indicating no diffusion between the sites responsible for these peaks. The intensity of the ζ peak varies from sample to sample and is almost absent in completely new samples but pronounced in heavily used samples. This suggests a correlation with Fe_2O_3 inclusions that slowly form due to repeated cleaning and oxidation cycles. [209] Thus, this peak may not represent the Fe_3O_4(001) surface. The

Die approbierte gedruckte Originalversion dieser Dissertation ist an der TU Wien Bibliothek verfügbar.
The approved original version of this doctoral thesis is available in print at TU Wien Bibliothek.
TU Bibliothek Your knowledge hub WIEN

discrepancy between experimental and theoretical desorption temperatures around the ζ peak supports this explanation. Since the simulation relies on equilibrium thermodynamics, it fails to accurately represent scenarios where widely separated regions on the surface cannot equilibrate rapidly through diffusion. Additionally, the Verwey transition, which alters the electronic structure of magnetite at 120 K by a metal-insulator phase transition, may influence molecular adsorption around this temperature (see section 1.5.3).

Below the saturation coverage of two C_2H_4/unit cell, the molecules can diffuse across the surface (even at the STM imaging temperature of 78 K), but are pinned at the surface defects (Figure 5.6 c)). The STM image represents a time-averaged view of the molecule positions on the surface, which explains why the apparent height of the molecules gradually decreases away from the defect. Lowering the temperature to 68 K leads to the formation of an ordered array of two C_2H_4/unit cell along the Fe rows (Figure 5.6 d)). However, STM alone cannot confirm whether the molecules are only adsorbed on the Fe rows or also between them at the given temperature and are therefore not visible in the images. The corresponding TPD peak, ε, saturates at about two C_2H_4/unit cell at 110-115 K, but emerges already at 0.3 C_2H_4/unit cell. Repulsion between the C_2H_4 molecules causes the peak to shift to lower temperatures with increasing coverage. DFT+U calculations also show a slight weakening of adsorption with increasing coverage from one to two C_2H_4/unit cell due to repulsion. Combing all experimental and computational results, we conclude that at a coverage of two C_2H_4/unit cell, the molecules adsorb along the Fe rows occupying every other Fe_{oct} surface atom with a next-nearest neighbour distance of 6 Å.

As mentioned above, further lowering the STM measurement temperature is not practical for magnetite, so we must rely on TPD and DFT+U data to model the full monolayer coverage of ≈four C_2H_4/unit cell. DFT+U calculations suggest that the original configuration of two C_2H_4/unit cell adsorbed along the Fe rows occupying every other Fe_{oct} surface atom remains intact when additional molecules are adsorbed between the rows. In this manner, a coverage of four C_2H_4/unit cell can be achieved. The TPD peaks δ and γ correspond to two C_2H_4/unit cell and saturate at about four C_2H_4/unit cell.

Above the saturation point of a full monolayer at four C_2H_4/unit cell, two multilayer peaks, α and β appear. As the coverage reaches approximately eight C_2H_4/unit cell, the peak shifts to higher temperatures, suggesting an abrupt structural change after

Die approbierte gedruckte Originalversion dieser Dissertation ist an der TU Wien Bibliothek verfügbar.
The approved original version of this doctoral thesis is available in print at TU Wien Bibliothek.
TU Bibliothek Your knowledge hub WIEN

the completion of the second layer.

Overall, the weak, non-dissociative binding of C_2H_4 to the Fe_3O_4(001) surface makes this system ideal for investigating the model hydroformylation reaction.

Die approbierte gedruckte Originalversion dieser Dissertation ist an der TU Wien Bibliothek verfügbar.
The approved original version of this doctoral thesis is available in print at TU Wien Bibliothek.

5.3 C_2H_4 adsorption on $Rh/Fe_3O_4(001)$

In this section I present a multitechnique study focusing on the interaction of C_2H_4 with Rh adatoms adsorbed on the $Fe_3O_4(001)$ surface.

STM imaging was carried out at the RT-STM. Figure 5.16 a) and b) show the $Fe_3O_4(001)$ surface after deposition of 0.2 ML Rh, before and after exposure to 3.4 L C_2H_4 at room temperature. In a) typical protrusions associated with Rh adsorption are visible on the surface. (for more details see section 5.1) ≈86 % of the Rh adatoms are 2-fold coordinated (blue circle), ≈3 % are 5-fold coordinated (blue dotted circle) and ≈12 % of the 2-fold coordinated adatoms form dimers along the [110] direction (blue arrow). With the imaging setting used, 2-fold coordinated Rh adatoms have an apparent height of 120–130 pm, while 5-fold coordinated Rh adatoms have an apparent height of 90–100 pm, relative to the apparent height of the Fe surface atoms. Additionally, a few clusters are visible, likely due to sintering caused by residual O_2 from sample preparation. [176]
After exposure to C_2H_4, the appearance and apparent height of both 2-fold and 5-fold coordinated Rh adatoms remain the same. However, XPS data confirm that C_2H_4 adsorbs at the Rh adatoms (see Figure 5.16 c)). The C 1s region shows a clear peak at ≈284 eV after exposure to C_2H_4, consistent with C_2H_4 adsorption. No C_2H_4 adsorption occurs at the $Fe_3O_4(001)$ surface at room temperature, implying that the signal must originate from C_2H_4 adsorption on Rh adatoms. The area of this peak is approximately double the area of the peak observed after CO adsorption on the $Rh/Fe_3O_4(001)$ system [176, 180, 184], suggesting that each Rh adatom adsorbs one C_2H_4 molecule. Moreover, the Rh 3d peak becomes sharper after C_2H_4 adsorption.
A quantitative analysis of the STM images before and after C_2H_4 exposure reveals a 12–15 % increase in the number of 5-fold coordinated Rh adatoms following C_2H_4 adsorption. No Rh dimer species are observed after C_2H_4 adsorption, suggesting that C_2H_4 facilitates the redispersion of dimers. The redispersion of small Rh clusters is likely also caused by C_2H_4 adsorption, as the overall coverage of Rh_1 species slightly increases. Splitting of Rh dimers by molecule adsorption has been previously observed upon exposure of the $Rh/Fe_3O_4(001)$ system to CO. (see section 5.1) [180]
DFT+U calculations for the minimum energy configuration of 2-fold and 5-fold coordinated Rh adatoms on $Fe_3O_4(001)$ with adsorbed C_2H_4 molecules are shown in

Die approbierte gedruckte Originalversion dieser Dissertation ist an der TU Wien Bibliothek verfügbar.
The approved original version of this doctoral thesis is available in print at TU Wien Bibliothek.
TU Bibliothek Your knowledge hub WIEN

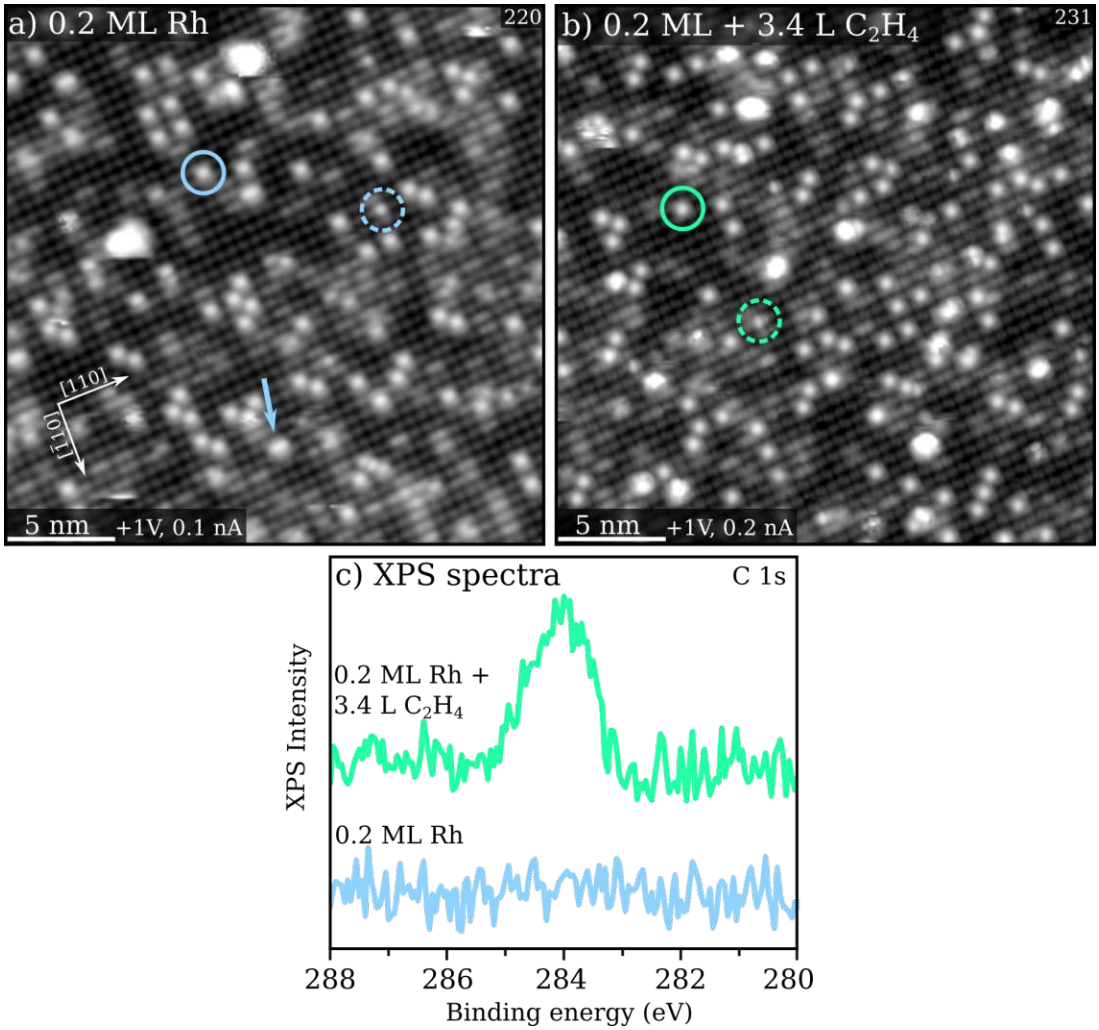

Figure 5.16: RT-STM images and XPS spectra of C_2H_4 adsorption on the $Rh/Fe_3O_4(001)$ system. STM images of the surface after deposition of 0.2 ML Rh, before a) and after b) exposure to 3.4 L C_2H_4 at room temperature. 2-fold and 5-fold coordinated Rh atoms are marked with a circle respectively a dotted circle. Rh dimers are marked with an arrow. XPS measurements in c) were conducted with Al Kα radiation in grazing emission (12° from normal). XPS spectra of the C 1s region show that C_2H_4 adsorption occurs at room temperature at the Rh adatoms. A peak at $\approx$ 184 eV emerges after C_2H_4 exposure.

Die approbierte gedruckte Originalversion dieser Dissertation ist an der TU Wien Bibliothek verfügbar.
The approved original version of this doctoral thesis is available in print at TU Wien Bibliothek.

Figure 5.17. For 2-fold coordinated Rh (Figure 5.17 a)), the C = C double bond is oriented parallel to the Fe row and the adsorption energy of the C_2H_4 molecule is calculated to be −2.26 eV. C_2H_4 adsorption causes the Rh atom to sink towards the Fe_3O_4(001) surface by 0.4 Å, allowing the formation of a weak bond (≈2.36 Å) between the Rh adatom and an O atom from the subsurface.
If the Rh-π interaction is considered as a single ligand, the resulting structure for the Rh adatoms is pseudo-square planar, which is generally favoured for Rh. Adsorbing CO on 2-fold coordinated Rh adatoms on Fe_3O_4(001) leads to the same behaviour. [180, 184]
For C_2H_4 adsorbed on 5-fold coordinated Rh adatoms, the C = C double bond is oriented perpendicular to the Fe row, with an adsorption energy of −1.49 eV.

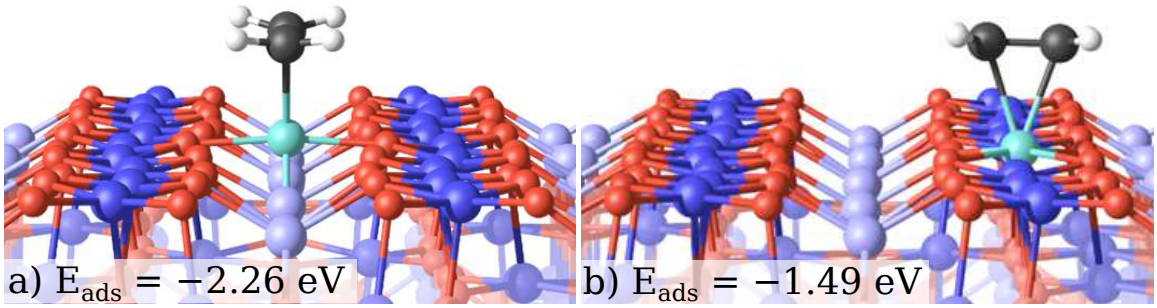

Figure 5.17: DFT+U-based calculations for C_2H_4 adsorption on 2-fold a) and 5-fold b) coordinated Rh adatoms on the Fe_3O_4(001) surface.

Next, the stability of Rh_1 species with adsorbed C_2H_4 at elevated temperatures was investigated. Figure 5.18 shows STM images after annealing the sample to 400 K a), 500 K b), and 600 K c) for 5 min. No significant changes in the STM images are observed after annealing to 400 K. Annealing to 500 K results in disappearance of almost all 2-fold coordinated Rh adatoms, although several features on the Fe rows appear that resemble those of 5-fold coordinated Rh adatoms (dotted green circle). These are likely formed by 2-fold coordinated Rh adatoms incorporating into the lattice. Additionally, a few small clusters form on the surface. Finally, when annealing to 600 K, both 2-fold and 5-fold coordinated Rh adatoms, as well as the small clusters, disappear, and the surface looks similar to an as-prepared surface, suggesting that all Rh species have incorporated into the subsurface.
To further understand the adsorption and desorption behaviour of C_2H_4 at elevated

Die approbierte gedruckte Originalversion dieser Dissertation ist an der TU Wien Bibliothek verfügbar.
The approved original version of this doctoral thesis is available in print at TU Wien Bibliothek.
TU Bibliothek Your knowledge hub WIEN

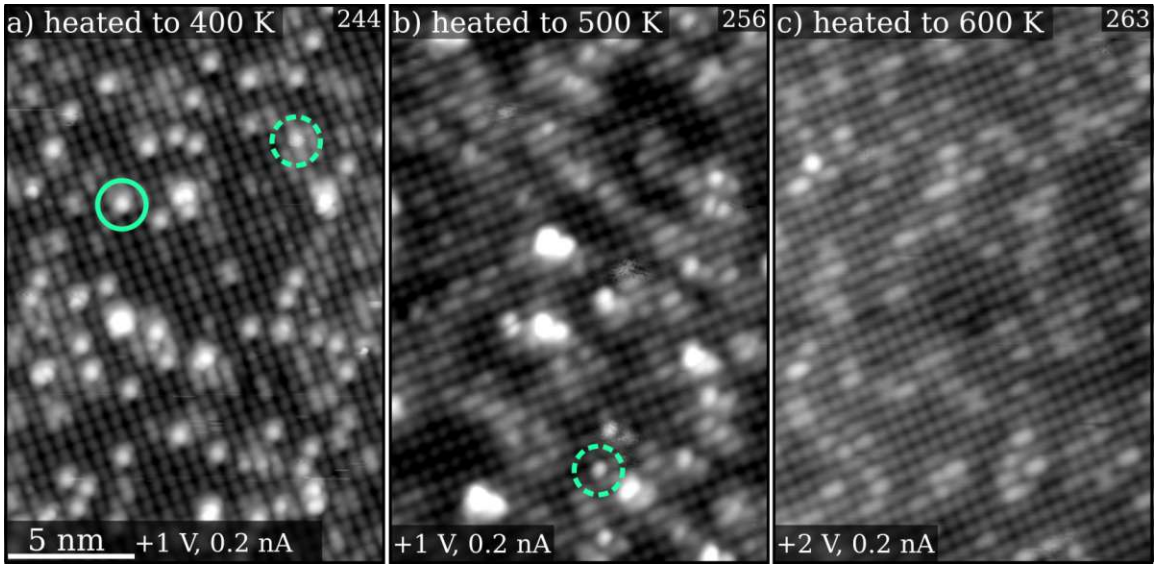

Figure 5.18: RT-STM images of the Fe_3O_4(001) surface with adsorbed Rh(C_2H_4) species after annealing the system to 400 K a), 500 K b), and 600 K c). Annealing to 400 K leads to no significant changes in the STM images. After annealing to 500 K, almost all 2-fold coordinated Rh_1 species disappear, while some incorporated 5-fold coordinated Rh adatoms and a small number of clusters can be observed. At 600 K Rh incorporates into the bulk, and the surface resembles its state prior to Rh deposition.

temperatures, series of TPD and XPS experiments were conducted. For the TPD experiment, 0.2 ML Rh was deposited onto Fe_3O_4(001), and subsequently, the sample was exposed to C_2H_4 until saturation coverage was reached. The sample was then cooled down to 250 K and afterwards annealed to 500 K, using a temperature ramp of 1 K/s. A continuous C_2H_4 desorption spectrum is observed, featuring a distinct peak at 462 K (see green curve in Figure 5.19 a)), which indicates desorption taking place from various sites on the surface, with differing adsorption energies. To better understand the desorption process, XPS spectra of the C 1s and Rh 3d region were analysed at different temperatures (see Figure 5.19 b) and c)). The C 1s region shows that the area of the C_2H_4 peak decreases by about one-third when the sample is heated to 395 K, which aligns well with the TPD desorption curve, as less than half of the C_2H_4 molecules have desorbed at this temperature. By 495 K, no C 1s peak can be detected, thus, we conclude that all C_2H_4 molecules have desorbed.

Die approbierte gedruckte Originalversion dieser Dissertation ist an der TU Wien Bibliothek verfügbar.
The approved original version of this doctoral thesis is available in print at TU Wien Bibliothek.
TU Bibliothek Your knowledge hub WIEN

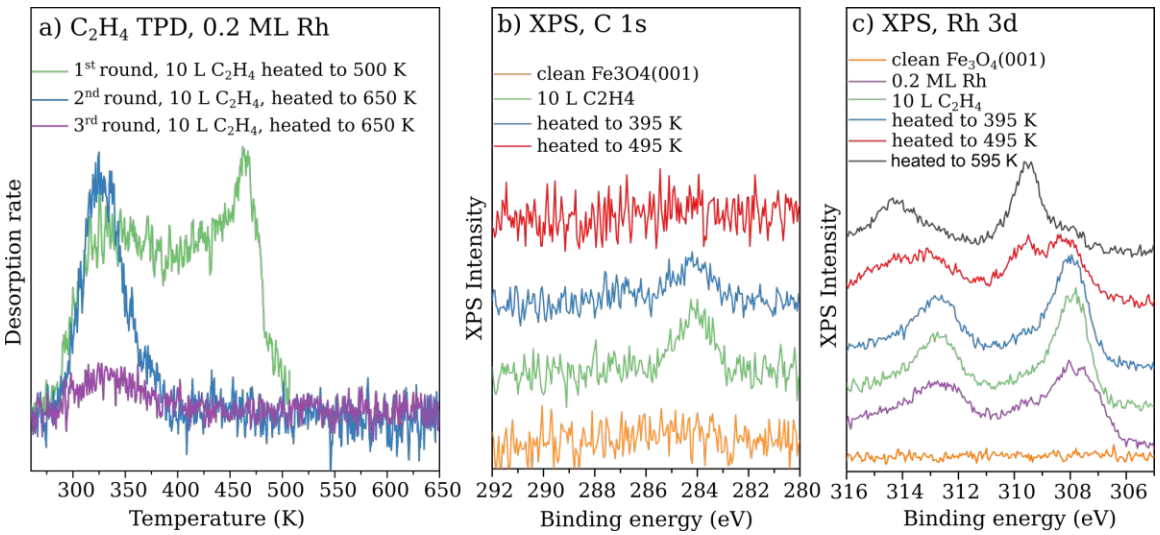

Figure 5.19: TPD and XPS spectra showing the thermal evolution of C_2H_4 adsorbed on the $Rh/Fe_3O_4(001)$ system. In a), a series of TPD spectra was obtained after deposition of 0.2 ML Rh and subsequent exposure to 10 L C_2H_4. The first TPD ramp was run from 250 K to 500 K. The sample was then cooled to 293 K, reexposed to 10 L C_2H_4, and the TPD was run from 250 K to 650 K. The proceeder was repeated in a third run. b) and c) shows XPS spectra of the C 1s and Rh 3d region after several annealing steps. After each step, the sample was cooled to room temperature for data acquisition.

The Rh 3d region (see Figure 5.19 c)) exhibits a relatively broad peak after Rh deposition (purple curve). This results from a combination of small clusters (307 eV), 2-fold coordinated Rh adatoms (307.7 eV), 5-fold coordinated Rh adatoms (308.0 eV), and 6-fold coordinated Rh adatoms (309.5 eV). [176] After exposure to C_2H_4, the peak sharpens due to the loss of components from low binding energy (green curve). As inferred from STM experiments, this behaviour is attributed to the splitting of Rh dimers and the redispersion of small clusters caused by C_2H_4 adsorption. Annealing to 395 K results in the desorption of more than half of the adsorbed C_2H_4 molecules. However, the chemical state and intensity of the Rh 3d peak does not change significantly (blue curve). Likely, C_2H_4 also desorbs from small clusters at that temperature (further explained in the discussion). Annealing further to 495 K results in the splitting of the peak into two components with binding energies of 308 eV and 309.5 eV,

Die approbierte gedruckte Originalversion dieser Dissertation ist an der TU Wien Bibliothek verfügbar.
The approved original version of this doctoral thesis is available in print at TU Wien Bibliothek.
TU Bibliothek Your knowledge hub WIEN

which we assign to 5-fold and 6-fold coordinated Rh adatoms (red curve) [176]. This corresponds well with the significant reduction of 2-fold coordinated Rh adatoms and appearance of 5-fold coordinated Rh adatoms, as observed in the STM images. Finally, after annealing to 600 K, the Rh 3d region is dominated by the contribution of 6-fold coordinated Rh atoms (grey curve), which aligns with the disappearance of 2-fold and 5-fold coordinated Rh adatoms seen in the STM images.
Revisiting the TPD experiment: for the second round (blue curve), the sample was cooled to room temperature, reexposed to C_2H_4, and annealed to 650 K. Since the sample was annealed to 500 K in the first round, mostly 5-fold and 6-fold coordinated Rh adatoms are left on the surface (as seen in Figure 5.18 b)) prior to C_2H_4 readsorption. A TPD spectrum with a peak at ≈330 K was observed (blue curve), again indicating weakly bound C_2H_4 adsorbed at 5-fold coordinated Rh adatoms and small clusters. Cooling the sample down, reexposing it to C_2H_4, and annealing it to 650 K result in a very small peak at the same temperature, likely due to a few Rh clusters that have not yet diffused into the bulk.
Using the same TPD analysis method like in sec 5.2 (explained in ref [130]), it was possible to analyse the sharp TPD peak at 462 K. The adsorption energy of C_2H_4 on 2-fold coordinated Rh adatoms was found to be −1.72 eV.

Discussion

Combining the results from STM, XPS, TPD, and DFT+U calculations, we conclude that C_2H_4 adsorbs molecularly on Rh adatoms and clusters on the $Fe_3O_4(001)$ surface, with no evidence of dissociation. The adsorption behaviour of C_2H_4 on the $Rh/Fe_3O_4(001)$ system is strongly influenced by the coordination environment of the Rh adatoms.
Adsorption of C_2H_4 does not change the appearance and apparent height of Rh_1 species in STM images, but XPS spectra of the C 1s region and TPD experiments provide evidence for the presence of C_2H_4. However, a significant increase of 5-fold coordinated Rh adatoms and the disappearance of Rh dimers after exposing the $Rh/Fe_3O_4(001)$ system to C_2H_4 can be observed in the STM images. A previous study carried out, by Jakub et al. in our research group shows that Rh predominantly forms 2-fold coordinated Rh adatoms, which incorporate into the lattice and become 5-fold and 6-fold coordinated adatoms after annealing to ≈450 K (see section 5.1). A small number, however, get incorporated already at room temperature, suggesting

Die approbierte gedruckte Originalversion dieser Dissertation ist an der TU Wien Bibliothek verfügbar.
The approved original version of this doctoral thesis is available in print at TU Wien Bibliothek.
TU Bibliothek Your knowledge hub WIEN

that specific locations facilitate the incorporation process. [176] Surface defects or Rh adatoms landing at particular sites within the unit cell could be the cause. It seems that adsorption of C_2H_4 promotes the formation of 5-fold coordinated Rh adatoms at specific sites, leading to a fivefold increase in concentration at room temperature after exposing the $Rh/Fe_3O_4(001)$ system to C_2H_4. Since we assume that the 2-fold coordinated Rh adatoms do not diffuse on the surface, the new 5-fold coordinated Rh adatoms likely arise from the redispersion of small Rh clusters and the splitting of Rh dimers after adsorption of C_2H_4. The dimer-splitting process is likely similar to that observed after CO adsorption on Rh adatoms on the $Fe_3O_4(001)$ surface [180], as explained in section 5.1.

Looking at the thermal evolution of the system, we observed that adsorption of C_2H_4 delays the incorporation of 2-fold coordinated Rh adatoms. These adatoms can still be detected up to annealing to 462 K, whereas annealing the surface with "bare Rh adatoms" to 420 K was sufficient to incorporate all 2-fold coordinated Rh adatoms, forming a mixture of 5-fold and 6-fold coordinated Rh_1 species. (This temperature differs slightly from that reported in the literature, which is likely due to different temperature readings from different experimental set-ups.) Additionally, XPS measurements show that 5-fold coordinated Rh adatoms are still present after heating to 595 K. Hence, it seems that adsorption of C_2H_4 stabilizes the Rh adatoms against incorporation and promotes the formation of 5-fold coordinated Rh adatoms at higher temperatures.

In addition to Rh adatoms with different coordination environments, small clusters can also be observed at room temperature. These clusters may have formed because several atoms landed at the same site during metal deposition, but it is also possible that O_2 from the residual gas causes sintering of Rh adatoms. [176] This heterogeneity is reflected in the broad TPD spectrum. Nevertheless, it was possible to determine that C_2H_4 binds most strongly to 2-fold coordinated Rh adatoms. Similar to CO adsorption on the $Rh/Fe_3O_4(001)$ system, C_2H_4 adsorption on 2-fold Rh adatoms leads to a pseudo-square planar environment, resulting from a weak bond between the Rh adatom and a subsurface O from the magnetite support. [180] In coordination chemistry, it is known that this geometry is stable for Rh(I) systems. Because of the appearance of 5-fold coordinated Rh adatoms in STM images after annealing the sample to 500 K, we assign the TPD signal at 300–400 K to desorption of C_2H_4 from 5-fold coordinated Rh adatoms. This assignment is consistent with the DFT+U cal-

Die approbierte gedruckte Originalversion dieser Dissertation ist an der TU Wien Bibliothek verfügbar.
The approved original version of this doctoral thesis is available in print at TU Wien Bibliothek.

culations, which show that the adsorption energy of C_2H_4 on 5-fold coordinated Rh adatoms (−1.49 eV) is significantly lower than that on 2-fold coordinated Rh adatoms (−2.26 eV). The broadness of the TPD peak is likely due to different environments of the 5-fold coordinated Rh adatoms resulting from various surface defects. Additionally, the presence of clusters of different sizes likely contributes to the broad peak. No coking related to C_2H_4 decomposition at the Rh clusters was detected, in contrast the substantial coking observed during C_2H_4 adsorption on alumina-supported Pt nanoclusters. [210]

In our study of CO adsorption on the $Rh/Fe_3O_4(001)$ system, we showed that gem di-carbonly species would be thermodynamically more stable than the monocarbonyl, but the experiments shows that di-carbonlys do not form directly at 2-fold coordinated Rh adatoms. However, Rh gem di-carbonlys form due to the splitting of Rh dimers via a metastable $Rh_2(CO)_3$ configuration. [180] (see section 5.1) In the case of C_2H_4 adsorption on Rh adatoms, no di-ethylene species can be observed. The differential adsorption energy calculated for a second C_2H_4 molecule adsorbed on a 2-fold coordinated Rh adatom is only −1.02 eV, suggesting that it is not stable enough at room temperature. However, adsorption of a second C_2H_4 molecule may also be prevented by the steric hindrance of the firstly adsorbed C_2H_4. Unlike in the CO adsorption study, no Rh di-ethylene species could be observed after the splitting of Rh dimers, implying that two C_2H_4 molecules are sufficient to split Rh dimers. Another possible explanation is that adsorption of three C_2H_4 molecules on a dimer causes its dissociation, similar to the behaviour observed with CO, but the second C_2H_4 molecule desorbs quickly from the $Rh(C_2H_4)_2$ complex because adsorption is not strong enough at room temperature. As in the case of CO adsorption, di-ethylene formation at 5-fold coordinated Rh adatoms is not possible.

Having studied both CO and C_2H_4 adsorption on the $Rh/Fe_3O_4(001)$ system, we observed that their different behaviour could impact the model hydroformylation reaction, as both molecules must adsorb at Rh adatoms for the reaction to occur. Typically, the reaction is conducted with a substantial excess of C_2H_4, as it has been proven that gem di-carbonyls can form under common reaction conditions. [149, 196] However, the absence of both di-carbonly and di-ethylene indicates that co-adsorption is not possible in UHV experiments, which is confirmed in a following study (see section 5.5).

Die approbierte gedruckte Originalversion dieser Dissertation ist an der TU Wien Bibliothek verfügbar.
The approved original version of this doctoral thesis is available in print at TU Wien Bibliothek.
TU Bibliothek Your knowledge hub WIEN

5.4 H_2 adsorption on $Rh/Fe_3O_4(001)$

In this section, I present a multitechnique study focusing on the interaction of H_2 with Rh adatoms adsorbed on the $Fe_3O_4(001)$ surface.

TPD

To determine the desorption behaviour of H_2 from Rh adatoms on the $Fe_3O_4(001)$ surface, 0.2 ML Rh was deposited onto the surface at room temperature, and subsequently the sample was exposed to 1 L D_2 at 200 K. The sample was then cooled down to 150 K and annealed to 700 K with a temperature ramp of 1 K/s. The resulting TPD spectrum for mass 4 shows one distinct peak at 295 K, indicating that D_2 desorbs from one specific site (see Figure 5.20).

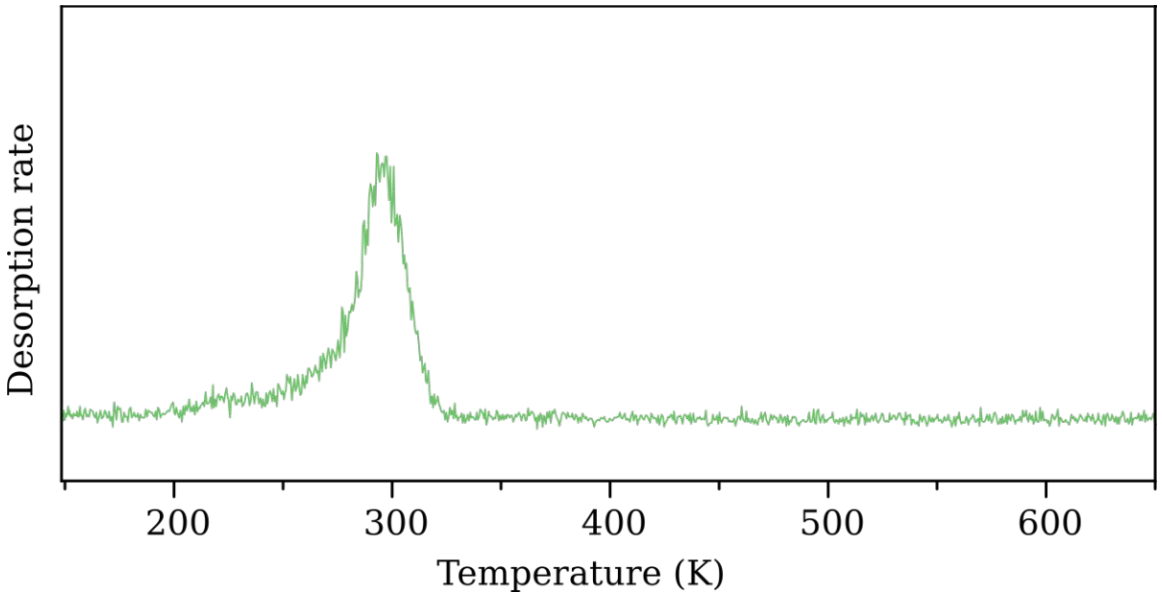

Figure 5.20: TPD spectrum of D_2 desorption from the $Rh/Fe_3O_4(001)$ system. A molecular beam was utilized to dose 1 L D_2 at 200 K. To acquire the TPD spectrum a temperature ramp of 1 K/s was run from 150 K to 700 K.

STM

STM imaging was carried out at the RT-STM.

Die approbierte gedruckte Originalversion dieser Dissertation ist an der TU Wien Bibliothek verfügbar.
The approved original version of this doctoral thesis is available in print at TU Wien Bibliothek.
TU Bibliothek Your knowledge hub WIEN

Since the desorption peak of H_2 from the $Rh/Fe_3O_4(001)$ system is at 295 K, adsorption at room temperature should be feasible. However, the onset of the desorption peak starts at ≈250 K, therefore, given the time-scale of a typical STM experiment (exposing the sample to molecules in the preparation chamber and subsequently transferring the sample into the imaging chamber), it is likely that the vast majority, if not all, of the H_2 molecules would have desorbed from the surface by the time STM imaging was conducted. To address this, a different approach was employed: 0.02 ML Rh was deposited onto the surface, afterwards the surface was imaged by STM. Once the system was stable, H_2 was dosed into the STM chamber during imaging.

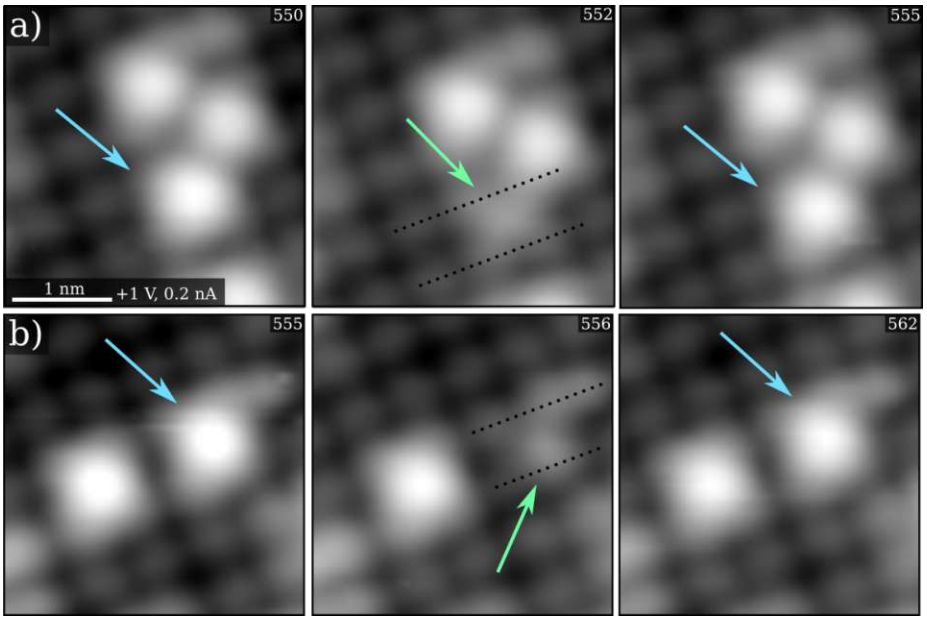

Figure 5.21: RT-STM images of the $Fe_3O_4(001)$ surface after deposition of 0.2 ML Rh. During imaging, a background pressure of $4 \cdot 10^{-9}$ mbar H_2 was maintained in the STM chamber. H_2 adsorption causes a reduction in the apparent height of the 2-fold coordinated Rh_1 species, highlighted with a green arrow. Two different structures of $Rh(H_2)$ species can be recognized: a) represents the majority of cases, where the feature is centred between the Fe rows, and b) shows the less frequent case, where the feature is slightly off-center. "Bare" 2-fold coordinated Rh adatoms are marked with a blue arrow.

In Figure 5.21, the adsorption and subsequent desorption of H_2 on 2-fold coordi-

Die approbierte gedruckte Originalversion dieser Dissertation ist an der TU Wien Bibliothek verfügbar.
The approved original version of this doctoral thesis is available in print at TU Wien Bibliothek.
TU Bibliothek Your knowledge hub WIEN

nated Rh adatoms is captured during scanning. A noticeable reduction in apparent height can be observed. Under the applied imaging conditions, 2-fold coordinated Rh adatoms exhibit an apparent height of 140 pm–160 pm. After H_2 adsorption, the apparent height decreases to a range of 40 pm–70 pm. Moreover, two different species can be observed due to H_2 adsorption. In most cases, the features are centred between the Fe rows (see Figure 5.21 a)), but in some cases, the features appear slightly tilted toward an Fe row (see Figure 5.21 b)). Both features exhibit approximately the same apparent height.

In any case, the experiments show that the adsorption energy of H_2 on 2-fold coordinated Rh adatoms is not high enough to form a stable Rh(H_2) species on the surface at room temperature.

Analysing the same area before and after exposure to 12 L H_2, it has been found that all 2-fold coordinated Rh adatoms, as well as the Rh dimers, remain at the same position. Thus, H_2 does not influence the stability or mobility of the Rh_1 and Rh_2 species. Unlike in the case of CO and C_2H_4 adsorption [134, 180], the same number of Rh dimers can be recognized after H_2 adsorption, suggesting that H_2 does not aid in the splitting of Rh dimers. The only difference between the two images is the reduction of apparent height of four 2-fold coordinated Rh adatoms due to H_2 adsorption.

A key question in the field of catalysis is whether H_2 can be activated and dissociated on Rh adatoms, followed by spillover onto the Fe_3O_4(001) surface. From the STM images, it can be inferred that no spillover occurs, as no changes are observed in the vicinity of Rh adatoms after H_2 adsorption.

DFT+U

DFT+U-based calculations for the minimum energy configuration of H_2 adsorption on 2-fold coordinated Rh adatoms on the Fe_3O_4(001) surface are shown in Figure 5.22. Two different structures, close in adsorption energy, were determined. In the first model, H_2 is adsorbed as a dihydrogen, remaining in its molecular form. The H atoms are oriented perpendicular to the Fe row ($E_{ads} = -1.08$ eV). In the second model, H_2 has dissociated and is therefore adsorbed as a dihydride on the Rh adatom, resulting in a slightly stronger adsorption energy ($E_{ads} = -1.24$ eV). In general, if the distance between the two H atoms is < 1 Å dihydrogen character is indicated, whereas if the H atoms are separated by > 1 Å it is better described as dihydride.

Die approbierte gedruckte Originalversion dieser Dissertation ist an der TU Wien Bibliothek verfügbar.
The approved original version of this doctoral thesis is available in print at TU Wien Bibliothek.
TU Bibliothek Your knowledge hub WIEN

However, the structure of the Rh(H_2) species remains the same, with the H atoms oriented perpendicular to the Fe rows. Similar to the adsorption of CO and C_2H_4 [134, 184], adsorption of H_2 results in sinking of the Rh adatom towards the Fe_3O_4(001) surface by 0.34 Å for the molecular case and by 0.45 Å for the dissociated case. In the molecular case, this allows the formation of a weak bond between the Rh adatom and an subsurface O atom from the magnetite support.

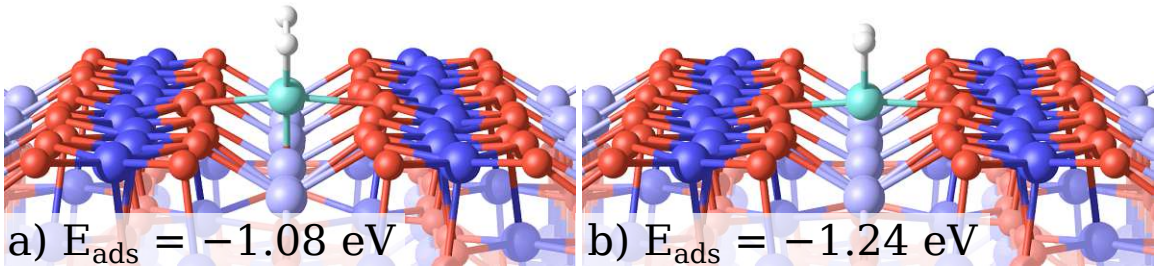

Figure 5.22: DFT+U-based calculations for the minimum energy configuration for H_2 adsorption on 2-fold coordinated Rh adatoms on the Fe_3O_4(001) surface. In a), H_2 adsorption in the form of a dihydride is shown, while in b), the dissociated structure is depicted.

Discussion

The adsorption behaviour of H_2 on 2-fold coordinated Rh adatoms bound to the Fe_3O_4(001) surface was thoroughly investigated by combining several surface-sensitive techniques, as well as DFT+U-based calculations. The observation of H_2 adsorption on 2-fold coordinated Rh adatoms, followed by rapid desorption during exposure to H_2, as seen in the RT-STM images, is consistent with the results from the TPD experiments. The TPD spectrum shows a distinct desorption peak of H_2 at 295 K, with the onset occurring at ≈250 K. Similar to the adsorption of CO [176], the apparent height of 2-fold coordinated Rh adatoms is significantly reduced by adsorption of H_2. This may result from a change in the electron density of the Rh atoms, likely due to the formation of a square-planar coordination environment. DFT+U-based calculations show that the 2-fold coordinated Rh adatoms sink towards the Fe_3O_4(001) surface after adsorption of H_2, analogous to the adsorption of CO and C_2H_4. [134, 180, 184] Therefore, the change in apparent height in the STM images could also be

Die approbierte gedruckte Originalversion dieser Dissertation ist an der TU Wien Bibliothek verfügbar.
The approved original version of this doctoral thesis is available in print at TU Wien Bibliothek.
TU Bibliothek Your knowledge hub WIEN

attributed to this effect.

Additionally, DFT+U-based calculations suggest that two different structures of H_2 adsorbed on 2-fold coordinated Rh adatoms, with a similar adsorption energy, could co-exist on the Fe_3O_4(001) surface. However, this does not explain the two different adsorption structures observed in the STM images. The calculated structures—one molecularly adsorbed, the other one dissociated—have the same orientation along the Fe_3O_4(001) surface lattice. In contrast, the two structures observed in the STM images are located on different positions relative to the lattice. Only the most frequently observed structure, where the Rh(H_2) complex is centred between the Fe rows, aligns with the theoretical calculations. A possible explanation for the two different structures is that, in some cases, H_2 adsorbed on the Rh adatom forms a hydrogen bond with a neighbouring hydroxyl group, thereby altering the orientation of the H_2 molecule. The presence of subsurface defects may also play a role in this phenomenon.

Unlike the adsorption of CO and C_2H_4, exposure to H_2 does not lead to splitting of Rh dimers. [134, 180] In general, no adsorption of H_2 on Rh_2 species could be recognized. However, due to the limited number of Rh dimers, and the infrequent occurrence of adsorption events on 2-fold coordinated Rh adatoms, it is possible that such a rare event was not captured during the experiments. Hence, we cannot fully exclude the possibility that H_2 adsorption on Rh_2 species could aid the splitting into two Rh_1 species.

Spillover of dissociated H, which would subsequently lead to the formation of surface hydroxyls on the Fe_3O_4(001) surface, was not observed. The surface shows no change in the close vicinity of Rh adatoms after H_2 adsorption. Only the characteristic switching of H between two O atoms on neighbouring Fe rows on the Fe_3O_4(001) surface can be seen. [198] A recent study by Mahapatra et al. supports our conclusions, also suggesting that under UHV conditions, no activation of H_2 takes place both on 2-fold coordinated and on 5-fold coordinated Rh adatoms. In contrast, the presence of Rh nanoparticles results in the formation of hydroxyls and subsequent etching of the Fe_3O_4(001) surface at temperatures higher than 500 K. [211]

The formation of dihydride and dihydrogen complexes is of significant importance not only for the hydroformylation reaction but also for other reactions, such as hydrogenation reactions and the hydrogen evolution reaction (HER). Stable dihydride and dihydrogen complexes are well documented and widely recognized in the field of

Die approbierte gedruckte Originalversion dieser Dissertation ist an der TU Wien Bibliothek verfügbar.
The approved original version of this doctoral thesis is available in print at TU Wien Bibliothek.
TU Bibliothek Your knowledge hub WIEN

organometallic chemistry. [212, 213] It has also been shown that dihydrogen complexes can exhibit high chemical stability. [214, 215] By altering the ligands, the degree of activation and the population of the H_2 antibonding orbital can be modulated. Given the analogies between SACs and coordination complexes, it is expected that similar H–M–H intermediates can form in these systems as well. A recent theoretical study has shown that the formation of stable H-M-H intermediates, in addition to the M-H intermediates, can alter the kinetics of HER in SAC. [216]
This highlights the importance of studying H_2 adsorption on SACs at the atomic level to fully understand the adsorption behaviour and enable the application of these model systems to the HER.

Die approbierte gedruckte Originalversion dieser Dissertation ist an der TU Wien Bibliothek verfügbar.
The approved original version of this doctoral thesis is available in print at TU Wien Bibliothek.
TU Bibliothek Your knowledge hub WIEN

5.5 Co-adsorption of CO and C_2H_4 on $Rh/Fe_3O_4(001)$

In this section, I present a multitechnique study determining the feasibility of co-adsorption of C_2H_4 and CO on Rh adatoms adsorbed on the $Fe_3O_4(001)$ surface under UHV conditions. This step is crucial for the hydroformylation reaction, as carbonylation of C_2H_4 needs to occur (see Figure 5.5 mechanism from structure 5 to 6)).

DFT+U

Minimum energy configurations for co-adsorption of CO and C_2H_4, as well as for di-carbonly and for di-ethylene on 2-fold coordinated Rh adatoms, were determined by DFT+U-based calculations (see Figure 5.23).

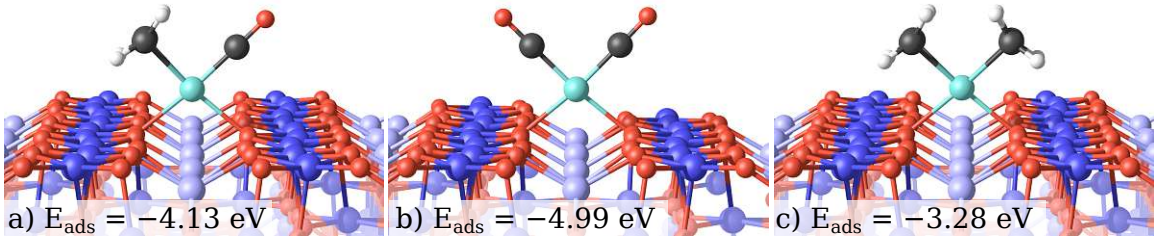

Figure 5.23: DFT+U-based calculation for the minimum energy configuration for co-adsorption of CO and C_2H_4 a), as well as for di-carbonly b) and for di-ethylene c) on 2-fold coordinated Rh adatoms on the $Fe_3O_4(001)$ surface

In all three structures, the ligands are oriented perpendicular to the Fe rows, with the Rh atom adopting a square planar configuration. The adsorption energy for co-adsorption of CO and C_2H_4, as well as for the di-carbonly structure, are relatively high, suggesting that both structures are stable at room temperature. The adsorption energy for di-ethylene is significantly lower, with the differential adsorption energy for the second C_2H_4 molecule only measuring −1.02 eV. This may not be enough for adsorption at room temperature.
However, from a theoretical perspective, co-adsorption of CO and C_2H_4 on 2-fold coordinated Rh adatoms should be feasible.

Die approbierte gedruckte Originalversion dieser Dissertation ist an der TU Wien Bibliothek verfügbar.
The approved original version of this doctoral thesis is available in print at TU Wien Bibliothek.

STM

Two sets of imaging experiments were conducted: one using RT-STM and the other one using LT-STM, with liquid nitrogen as a cryogen, which results in a sample temperature of 78 K.

Two different approaches were employed to attempt co-adsorption of CO and C_2H_4 on 2-fold coordinated Rh adatoms (co-adsorption on 5-fold and 6-fold coordinated Rh adatoms is not possible, because higher coordination than 6-fold is energetically not favourable). 0.2 ML Rh was deposited onto Fe_3O_4(001) at room temperature. For the first experiment, the sample was exposed to CO first, followed by C_2H_4 (see Figure 5.24 a)). In the second experiment, the exposure order was reversed, with the sample first exposed to C_2H_4 and subsequently to CO (see Figure 5.24 b)).

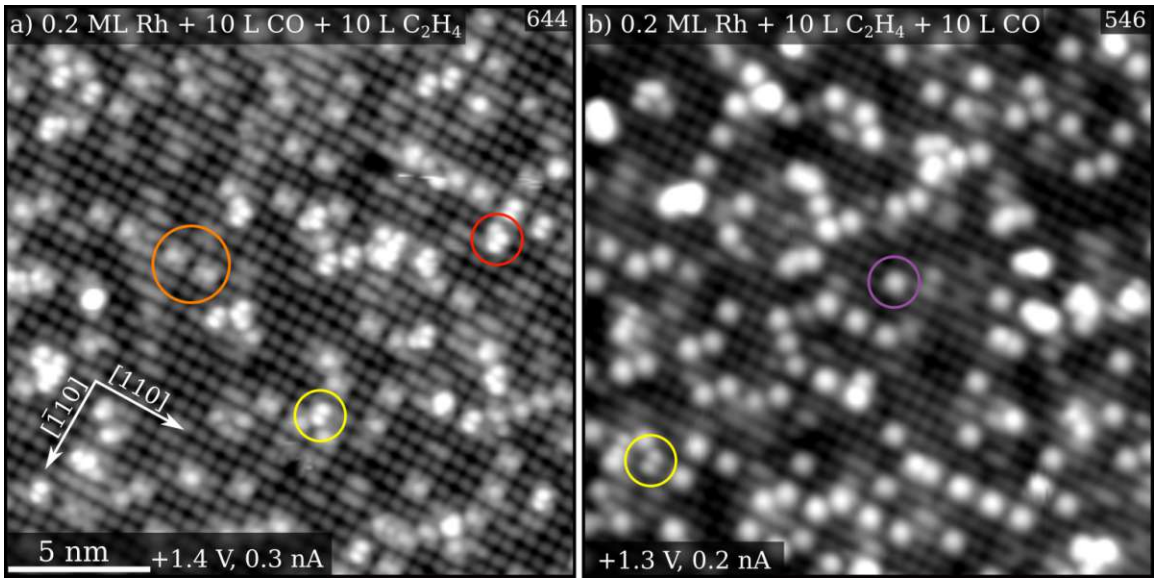

Figure 5.24: LT-STM images of the Fe_3O_4(001) surface after deposition of 0.2 ML Rh and subsequent exposure to CO and C_2H_4. a) shows the surface after exposure to 10 L CO, followed by exposure to 10 L C_2H_4. In b), the order of exposure is reversed, with the sample first exposed to 10 L C_2H_4 and subsequently to 10 L CO.

Upon closer examination of the LT-STM image in Figure 5.24 a) following the first approach (10 L CO, then 10 L C_2H_4), it is evident that the majority of features resemble those highlighted by the orange circle. Due to their characteristic appearance and apparent height, we can assign them to Rh monocarbonlys. These features ap-

Die approbierte gedruckte Originalversion dieser Dissertation ist an der TU Wien Bibliothek verfügbar.
The approved original version of this doctoral thesis is available in print at TU Wien Bibliothek.
TU Bibliothek Your knowledge hub WIEN

pear in two symmetrically mirrored configurations. A previous study demonstrated that Rh adatoms sink down towards the surface, forming a weak bond with a subsurface O atom, creating a pseudo-square planar environment for the Rh adatom. [184] There are two symmetrically equivalent subsurface O atoms beneath the Rh_1 site, enabling switching of the Rh-O bond between these two O atoms. Since both subsurface O atoms are not directly beneath the Rh adatom, the CO molecule is tilted away from the surface normal, resulting in two symmetrically equivalent configurations for Rh(CO) that can be recognized in STM. [180] Additionally double features (yellow circle), assigned to $Rh(CO)_2$ species [176] and L-shaped features (red circle), assigned to $Rh_2(CO)_3$ species, which consist of a $Rh(CO)_2$ species and a 5-fold coordinated Rh adatom with an adsorbed CO molecule [217], can also be recognized. All of these features are characteristic for CO adsorption on the $Rh/Fe_3O_4(001)$ system. ≈90 % of the features between the Fe rows can be attributed to mono- and di-carbonly species adsorbed at 2-fold coordinated Rh adatoms. The remaining ≈10 % are significantly higher in apparent height. However, this ratio remains similar, whether C_2H_4 is dosed or not. In the experiments conducted at the RT-STM, the dosage of the molecules was altered, with the sample being exposed to 3.4 L CO and subsequently to 17 L C_2H_4 after deposition of 0.2 ML Rh. The same features were observed, but with a slightly different ratio. Both with and without exposure to C_2H_4, features higher than Rh(CO) and $Rh(CO)_2$ are present with concentrations of 16–20 %. Overall, since no significant changes can were observed before and after exposure to C_2H_4, we suggest that co-adsorption did not occur.

LT-STM images following the second approach (10 L C_2H_4 , then 10 L CO) are shown in Figure 5.24 b). The same double features (yellow circle), with a comparable apparent height, present in Figure 5.24 a) and assigned to $Rh(CO)_2$ species can be seen occasionally. Since di-ethylene formation was not reported for C_2H_4 adsorption on Rh adatoms (see section 5.3), these features are very likely di-carbonyls. However, the majority of features are single dispersed features, highlighted with a violet circle, resembling the appearance and apparent height of "bare" 2-fold coordinated Rh adatoms. The same outcome can be recognized in the RT-STM experiments (3.4 L C_2H_4, then 17 L CO). As mentioned in the section above, C_2H_4 adsorption on the $Rh/Fe_3O_4(001)$ system leads to no significant change of the 2-fold coordinated Rh adatoms appearance in STM. Thus, from STM alone we cannot exclude or prove the presence of C_2H_4 or a possible co-adsorption of C_2H_4 and CO on the Rh adatoms.

Die approbierte gedruckte Originalversion dieser Dissertation ist an der TU Wien Bibliothek verfügbar.
The approved original version of this doctoral thesis is available in print at TU Wien Bibliothek.
TU Bibliothek Your knowledge hub WIEN

Therefore, other techniques are essential to further analyse this system.

TPD and XPS

0.2 ML Rh were deposited, and subsequently, the sample was exposed first to CO and then to C_2H_4 for the first experiment, and first to C_2H_4 and then to CO for the second experiment. Molecules were dosed at room temperature. To acquire the TPD spectra, the sample was cooled down to 250 K and then annealed to 650 K using a temperature ramp of 1 K/s. XPS measurements were conducted at room temperature.

As with the STM experiments, I will first discuss the experiments where CO was dosed first, followed by C_2H_4. The TPD spectra in orange and purple in Figure 5.25 serve as references for CO and C_2H_4 adsorption on $Rh/Fe_3O_4(001)$, respectively. The TPD spectrum for mass 29 (detecting CO), after exposure to 3.4 L CO, exhibits a broad spectrum due to CO desorption from multiple sites at the surface (2-fold and 5-fold coordinated Rh adatoms and Rh clusters). The distinct peak at ≈500 K corresponds to desorption from 2-fold coordinated Rh adatoms. [176] The TPD spectrum for mass 27 (detecting C_2H_4), after exposure to 3.4 L C_2H_4 is explained in detail in section 5.3. The peak at 462 K corresponds to C_2H_4 desorption from 2-fold coordinated Rh adatoms and the contribution at ≈330 K to 5-fold coordinated Rh adatoms and Rh clusters. After exposure to 3.4 L CO, followed by 3.4 L C_2H_4, the desorption spectrum for mass 29 (Figure 5.25 a) green curve) shows a decrease in peak intensity at 500 K, indicating a reduction in CO molecules adsorbed at 2-fold coordinated Rh adatoms compared to the spectrum obtained after exposure to CO alone. Additionally, the spectrum lacks a shoulder on the low-temperature side. The TPD spectrum for mass 27 (Figure 5.25 b) green curve) shows desorption in the region of 5-fold coordinated Rh adatoms and Rh clusters, as well as a small peak at 462 K, corresponding to desorption from 2-fold coordinated Rh adatoms. Overall, the data suggests that after exposure to 3.4 L CO and 3.4 L C_2H_4, a smaller fraction of the 2-fold coordinated Rh adatoms are occupied by CO, with C_2H_4 now occupying the newly available sites. However, co-adsorption of CO and C_2H_4 is likely not occurring. A detailed analysis is provided in the discussion.

Next, we turn to the second experiment, where C_2H_4 was dosed first, followed by CO. The desorption spectrum for mass 27 is almost identical, whether 3.4 L CO was additionally dosed or not. The only difference is the absence of a shoulder on the low-

Die approbierte gedruckte Originalversion dieser Dissertation ist an der TU Wien Bibliothek verfügbar.
The approved original version of this doctoral thesis is available in print at TU Wien Bibliothek.
TU Bibliothek Your knowledge hub WIEN

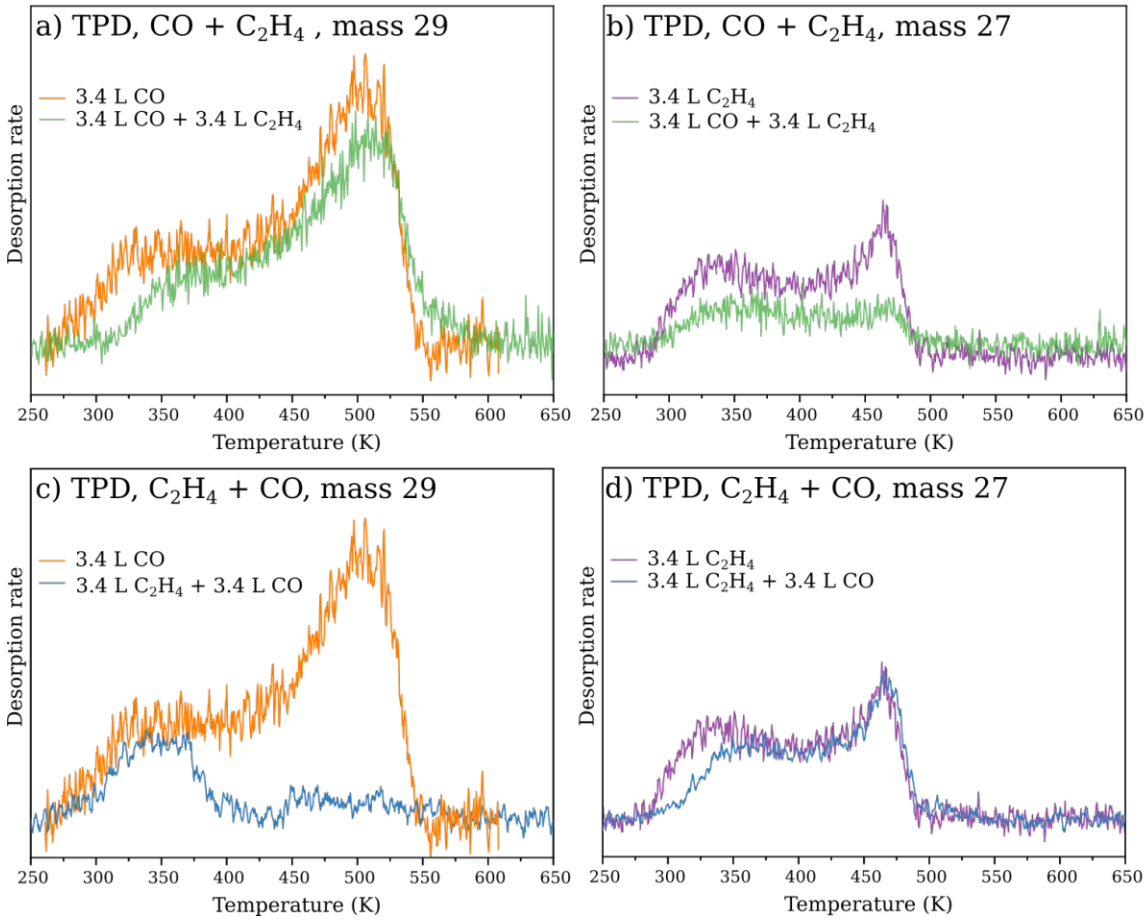

Figure 5.25: TPD spectra of the $Fe_3O_4(001)$ surface after deposition of 0.2 ML Rh and subsequent exposure to CO and C_2H_4 in different orders. Isotopical labelled CO (^{13}CO) was used to distinguish CO dosed onto the surface from CO in the residual gas. a) and c) show spectra of the mass 29, and b) and d) show spectra of the mass 27.

temperature side compared to the spectrum obtained after exposure to C_2H_4 alone (Figure 5.25 d) blue curve). In the TPD spectrum for mass 29 (Figure 5.25 c) blue curve), CO desorption is only observed in the low-temperature region, with no contribution from 2-fold coordinated Rh adatoms visible. As with the first experiment, co-adsorption of CO and C_2H_4 on Rh adatoms seems unlikely. A detailed analysis is provided in the discussion.

In addition to the experiments described above, two additional experiments were con-

Die approbierte gedruckte Originalversion dieser Dissertation ist an der TU Wien Bibliothek verfügbar.
The approved original version of this doctoral thesis is available in print at TU Wien Bibliothek.

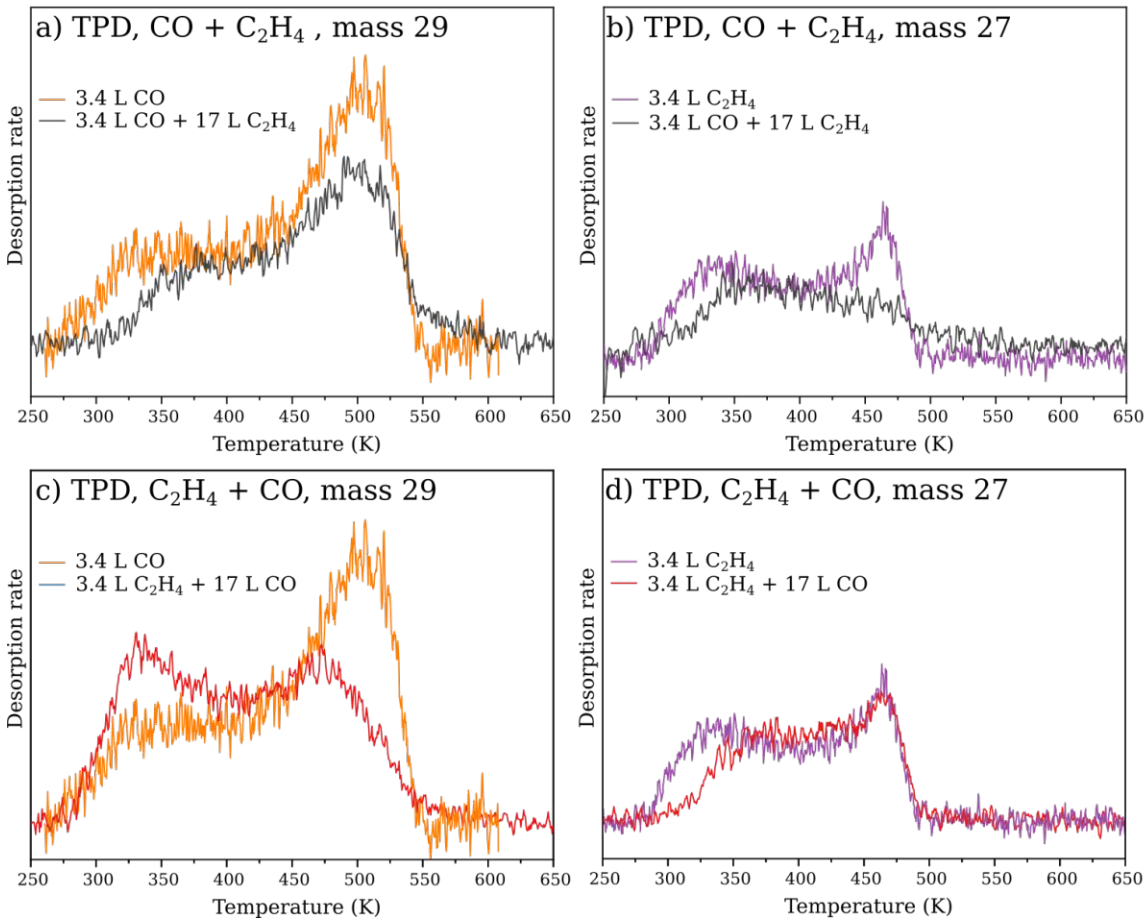

Figure 5.26: TPD spectra of the Fe_3O_4(001) surface after deposition of 0.2 ML Rh and subsequent exposure to CO and C_2H_4 in different orders. In this case, the second molecule was introduced in excess.

ducted in which 3.4 L of the first molecule was dosed, before the sample was exposed to the second molecule at a dosage of 17 L. The objective was to investigate whether co-adsorption could occur when the second molecule was introduced in excess. Similar to the experiments above, Figure 5.26 a) and b) show TPD spectra after exposure to CO followed by C_2H_4, while c) and d) show TPD spectra after exposure to C_2H_4 followed by CO.

The spectrum in a) for mass 29, (black curve) exhibits less peak intensity at 500 K than in Figure 5.25 a) (green curve), indicating that even less CO was adsorbed at 2-fold coordinated Rh adatoms. In accord with this, C_2H_4 adsorption seems to be

Die approbierte gedruckte Originalversion dieser Dissertation ist an der TU Wien Bibliothek verfügbar.
The approved original version of this doctoral thesis is available in print at TU Wien Bibliothek.

more pronounced. A broad spectrum spanning all desorption regions can be seen in the spectrum for mass 27, (Figure 5.26 b), black curve), with higher intensity than the spectrum in Figure 5.25 b) (green curve).
In the reversed experiment, the TPD spectrum in Figure 5.26 d) (red curve) is almost identical to the spectrum in Figure 5.25 d) (blue curve). Surprisingly, the TPD spectrum for mass 29 (Figure 5.26 b) (red curve)) exhibits a peak at ≈500 K with a very strong signal. However, since the XPS spectrum of the C 1s region (shown below) does not show comparable results, we assign this outcome to molecule displacement. Detailed explanations can be found in the discussion.

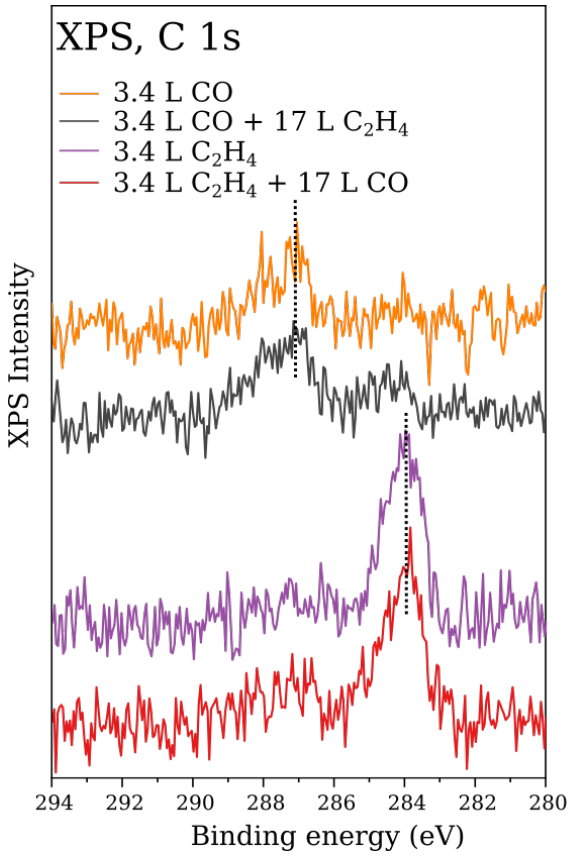

Figure 5.27: XPS spectra of the C 1s region of the Fe_3O_4(001) surface after deposition of 0.2 ML Rh and subsequent exposure to CO and C_2H_4 at room temperature in different orders.

Exposing the Rh/Fe_3O_4(001) system to 3.4 L CO leads to a peak in the C 1s region of the XPS spectrum at 287.1 eV (Figure 5.27 orange curve), corresponding to CO

Die approbierte gedruckte Originalversion dieser Dissertation ist an der TU Wien Bibliothek verfügbar.
The approved original version of this doctoral thesis is available in print at TU Wien Bibliothek.

adsorption on Rh adatoms on the Fe_3O_4(001) surface. [176] Exposing the sample to 3.4 L CO, followed by 17 L C_2H_4, results in the same peak with almost the same intensity and peak area. Additionally, a small peak at 284 eV appears, corresponding to C_2H_4 adsorption on Rh adatoms [134] (Figure 5.27 green curve).
Exposing the sample to 3.4 L C_2H_4 leads to a peak in the C 1s region of the XPS spectrum at 284 eV (Figure 5.27 purple curve). Exposing the sample to 3.4 L C_2H_4, followed by 17 L CO, results in the same peak with almost the same intensity and peak area. Additionally, a small peak at 287.1 eV appears.(Figure 5.27 blue curve) This behaviour is similar to the first experiment, but in a reversed order.

Discussion

Overall, the experimental data suggests that no co-adsorption of CO and C_2H_4 on 2-fold coordinated Rh adatoms on the Fe_3O_4(001) surface occurs at the given pressure regime, regardless of the order of dosing or the amount of dosed molecules.
The first experiment (first exposure to 3.4 L CO, then to 3.4 L C_2H_4) suggests that most 2-fold coordinated Rh adatoms are occupied by one or two CO molecules, even if C_2H_4 was introduced. However, in the STM images, a small percentage of features between the Fe rows exhibit a higher apparent hight, even if the sample was only exposed to CO. One possibility is that a small fraction of 2-fold coordinated Rh adatoms did not adsorb any molecule, though this seems unlikely at a dosage of 3.4 L. We suggest that another molecule from the residual gas may have coordinated to the Rh adatom before or during CO exposure. The observation that only little C_2H_4 adsorbs at a Rh adatom already occupied by CO is confirmed by XPS. Only a very small C 1s peak in the region for C_2H_4 adsorption is seen, even after a dosing 17 L C_2H_4. We cannot completely exclude the possibility that a small fraction of Rh adatoms accommodate both CO and C_2H_4, though this seems unlikely. The TPD spectrum suggests that a small amount of C_2H_4 desorbs both from weak binding sites (5-fold coordinated Rh adatoms and Rh clusters) and from 2-fold coordinated Rh adatoms. Desorption from weak binding sites could be explained by CO desorption during C_2H_4 exposure, allowing subsequent C_2H_4 adsorption at these sites. This effect could also explain the absence of a shoulder on the low-temperature side in mass 29 spectrum (green curve). Since the peak for CO desorption from 2-fold coordinated Rh adatoms is reduced while the peak for C_2H_4 desorption from 2-fold coordinated Rh adatoms emerges, it seems that an exchange from CO to C_2H_4 occurs.

Die approbierte gedruckte Originalversion dieser Dissertation ist an der TU Wien Bibliothek verfügbar.
The approved original version of this doctoral thesis is available in print at TU Wien Bibliothek.
TU Bibliothek Your knowledge hub WIEN

This is curious, as CO is more strongly bound to Rh adatoms than C_2H_4. [134, 184] It is possible that C_2H_4 adsorbs on Rh sites previously occupied by other molecules. Additionally, C_2H_4 is known to redisperse Rh dimers and small Rh clusters on the $Rh/Fe_3O_4(001)$ system, potentially enabling mono-ethylene formation on 2-fold coordinated Rh adatoms, though only in a limited number. However, this does not account for the observed reduction in the CO desorption peak, which remains unknown. A quantitative analysis of the STM images also provides no further insight, as the number of Rh(CO) and $Rh(CO)_2$ sites does not decreases after exposure to C_2H_4. Based on the results of the study on C_2H_4 adsorption on Rh adatoms, it is evident that the 2-fold coordinated Rh adatoms are not identical. It is possible that CO desorbs from some of these Rh adatoms already at room temperature, if they are located near a defect.

In the second experiment (first exposure to 3.4 L C_2H_4, then to 3.4 L CO), 2-fold coordinated Rh adatoms show no change in appearance and apparent height, characteristic for mono-ethylene adsorption. Additionally, XPS measurements do not indicate co-adsorption, as only a very small C 1s peak in the region of CO adsorption is seen, even after dosing 17 L CO. Finally, the TPD spectrum suggests that a small amount of CO adsorption occurs at 5-fold coordinated Rh adatoms and clusters, but not at 2-fold coordinated Rh adatoms. Similar to the first experiment, the absence of a shoulder on the low-temperature side in the mass 27 spectrum (blue curve) likely results from C_2H_4 desorption from weak binding sites during CO exposure, allowing for CO to adsorb at these sites. Some of the 2-fold coordinated Rh adatoms, as explained above, may also contribute due to weaker adsorption caused by their specific location on the surface.

Even when exposing the sample to an excess of the second molecule (17 L), we do not see clear evidence of co-adsorption on Rh adatoms from STM and XPS. The results from the TPD experiments are surprising, as for both experiments, desorption from weak binding sites and from 2-fold coordinated Rh adatoms is significantly higher than when the second molecule was introduced at a lower dosage. However, since this outcome is not supported by the results from other techniques, we attribute this to an experimental artefact. Dosing 17 L of CO or C_2H_4 following the dose of the first gas, the sticking probability of the molecules is very low. As a result, many molecules enter the gas phase near the sample and may adsorb outside of the beam spot. Additionally, the possibility of adsorption on Rh atoms present on the sample

Die approbierte gedruckte Originalversion dieser Dissertation ist an der TU Wien Bibliothek verfügbar.
The approved original version of this doctoral thesis is available in print at TU Wien Bibliothek.
TU Bibliothek Your knowledge hub WIEN

plate cannot be fully excluded.
It seems that co-adsorption is only possible on Rh nanoclusters, which can form due to O_2 in the residual gas. [176]
From a theoretical standpoint, co-adsorption of CO and C_2H_4 on 2-fold coordinated Rh adatoms should be possible and exhibit a high adsorption energy, suggesting stability at room temperature. However, as already mentioned earlier, after adsorption of either CO or C_2H_4 on 2-fold coordinated Rh adatoms, the Rh atoms sink towards the $Fe_3O_4(001)$ surface and form a bond with a subsurface O atom. [134, 180, 184] This quasi-square planar environment may block adsorption of an additional molecule, as the Rh atom is already in a favourable configuration. Another possible explanation for the absence of co-adsorption is steric hindrance. The bond between Rh and the two equivalent subsurface O atoms undergoes dynamic flipping, causing the ligand on top to oscillate. As a result, adsorption of an additional molecule may not be feasible under UHV conditions. If this was the case, increasing the pressure during exposure to the second molecule could potentially facilitate co-adsorption.

Overall, it seems that hydroformylation with this model system under the given conditions is not possible. However, important insight into molecule adsorption on the $Rh/Fe_3O_4(001)$ system were obtained, which may be of interest for other catalytic reactions on metal single atoms.

Die approbierte gedruckte Originalversion dieser Dissertation ist an der TU Wien Bibliothek verfügbar.
The approved original version of this doctoral thesis is available in print at TU Wien Bibliothek.

6 Summary

The goal of this thesis was to gain further insights into SAC at an atomic level, aiming to understand metal-support interactions, atomic structures of the active sites and their adsorption behaviour. All the support materials used—TiO_2, α-Fe_2O_3 and Fe_3O_4—are widely utilized as supports in SAC. The work focuses on several well-defined surfaces, addressing two main topics: first, the influence of water on various metal-support systems, and second, gaining insights into the hydroformylation reaction using a well defined SAC model system.

The first chapter of the results, chapter 3, focuses on rutile $TiO_2(110)$ and anatase $TiO_2(101)$. On rutile $TiO_2(110)$, the behaviour of Rh and Pt was investigated under two conditions: after deposition in UHV and in a water vapour background of $2 \cdot 10^{-8}$ mbar. In UHV, Rh was found to sinter at temperatures above 150 K, while at lower temperatures, single dispersed adatoms are coordinated to O atoms from the surface. Pt, on the other hand, forms a mixture of clusters and single atoms at room temperature, with the single atoms adsorbed at commonly occurring defect sites ($V_{O_{2c}}$). For Rh, water has no significant impact; however, for Pt, sintering is promoted due to water molecules splitting and occupying the $V_{O_{2c}}$ sites.

On anatase $TiO_2(101)$, the behaviour of Rh, Pt, Ni and Ir was examined under similar conditions. In UHV, a trend in dispersion was observed, aligning with the results on rutile $TiO_2(110)$: Ir $>$ Ni $>$ Pt $>$ Rh. Rh exclusively forms clusters, Pt and Ni form a mixture of clusters and single atoms, and Ir primarily forms single dispersed atoms. The trend on both surfaces corresponds well with the oxygen affinity of the metals, with the exception of Pt. When deposited in the presence of water, Ni showed enhanced dispersion, Ir exhibit sintering, and no significant effect was observed on Rh and Pt. These results demonstrate that the effect of water is significantly harder to predict then dispersion behaviour in UHV and varies for each metal-support system. This highlights that neglecting the influence of water, as is often done in model SAC, can lead to oversimplified models. Additionally, the finding suggest that single

Die approbierte gedruckte Originalversion dieser Dissertation ist an der TU Wien Bibliothek verfügbar.
The approved original version of this doctoral thesis is available in print at TU Wien Bibliothek.
TU Bibliothek Your knowledge hub WIEN

atoms are likely adsorbed at defect sites, indicating that extrinsic doping of support materials could be a strategy to create stronger binding sites.

The next chapter, chapter 4, also investigates the influence of water. In a previous study [159], Rh on α-$Fe_2O_3(1\bar{1}02)$ was shown to forms clusters when deposited in UHV, but water vapour during deposition stabilizes single dispersed Rh adatoms on the surface via coordination with OH ligands. This system was further investigated in this thesis by utilizing nc-AFM with a CO-functionalized tip. The greater resolution of nc-AFM compared to STM allowed for full resolution of the OH groups stabilizing the Rh adatoms, showing that two OH groups are sufficient for stabilization. A model, derived from feature positions observed in nc-AFM images and relaxed by DFT+U, suggests that the Rh atom exhibits square planar coordination, bonded to two O atoms from the surface and two OH ligands. The OH groups are also bonded to the nearest surface Fe atoms. Additionally, OH adsorbed at surface Fe atoms can form a hydrogen-bond with the O atom of the OH groups atop the Rh adatom. Occasionally, a third species coordinated to the Rh adatom, likely a water molecule, was observed. The influence of water on α-$Fe_2O_3(1\bar{1}02)$ differs significantly from that on the two TiO_2 surfaces examined, again emphasizing the need for individual investigation of each metal-support system.

Chapter 5, the final results chapter, focuses on fundamental adsorption studies on the $Rh/Fe_3O_4(001)$ system, providing insights into an industrially important reaction, the hydroformylation reaction, typically catalysed by a homogeneous catalyst. Rh is known to be 2-fold coordinated after deposition at room temperature, incorporating into the surface at higher temperatures—first in a 5-fold, then a 6-fold coordination and eventually diffusing into the bulk.

The first subchapter examines the adsorption behaviour of C_2H_4 on the bare surface. The molecules adsorb non-dissociatively, forming a full monolayer coverage consisting of 4 molecules per surface unit cell below 90 K. Two molecules adsorb along the Fe rows, occupying every other Fe_{oct} surface atom, while the other two are loosely bound between the rows. These desorb at 90 K from the surface, leaving behind half a monolayer. The strongest adsorption was observed at surfaces defect sites, with desorption at 160 K. Due to the weak adsorption on the surface, C_2H_4 is ideal to study adsorption on the $Rh/Fe_3O_4(001)$ system.

Reactants of the hydroformylation reaction (CO, C_2H_4 and H_2) were probed individually on Rh adatoms, with CO investigated in a previous study [180]. For C_2H_4,

Die approbierte gedruckte Originalversion dieser Dissertation ist an der TU Wien Bibliothek verfügbar.
The approved original version of this doctoral thesis is available in print at TU Wien Bibliothek.
TU Bibliothek Your knowledge hub WIEN

we found that one C_2H_4 molecule per Rh adatom adsorbs at room temperature. Studying the thermal evolution of the system reveals that the adsorption of C_2H_4 stabilizes Rh adatoms against incorporation and promotes the formation of 5-fold coordinated Rh adatoms at elevated temperatures. H_2 adsorption is weaker than C_2H_4 adsorption, desorbing at 295 K. STM and DFT+U calculations suggest that an H_2 molecule, bound to a 2-fold coordinated Rh adatom is oriented perpendicular to the Fe rows, either molecularly or dissociated, with no spillover to the surface. In the final subchapter, the feasibility of co-adsorption of C_2H_4 and CO on Rh adatoms was explored. However, no co-adsorption was observed within the pressure regime studied.

In summary, this thesis demonstrates that water can significantly influence metal-support interactions, often unpredictably. It also provides fundamental insights into the adsorption behaviour of a well-established model SAC system. The results highlight the importance of fundamental surface science research to fully understand SAC systems and molecular adsorption at an atomic level.

Die approbierte gedruckte Originalversion dieser Dissertation ist an der TU Wien Bibliothek verfügbar.
The approved original version of this doctoral thesis is available in print at TU Wien Bibliothek.
TU Bibliothek Your knowledge hub WIEN

Bibliography

1. Liu, L. & Corma, A. Metal catalysts for heterogeneous catalysis: from single atoms to nanoclusters and nanoparticles. *Chemical reviews* **118,** 4981–5079 (2018).
2. Wang, A., Li, J. & Zhang, T. Heterogeneous single-atom catalysis. *Nature Reviews Chemistry* **2,** 65–81 (2018).
3. Yang, X.-F. *et al.* Single-atom catalysts: a new frontier in heterogeneous catalysis. *Accounts of chemical research* **46,** 1740–1748 (2013).
4. Sautet, P. & Delbecq, F. Catalysis and surface organometallic chemistry: a view from theory and simulations. *Chemical reviews* **110,** 1788–1806 (2010).
5. Cui, X., Li, W., Ryabchuk, P., Junge, K. & Beller, M. Bridging homogeneous and heterogeneous catalysis by heterogeneous single-metal-site catalysts. *Nature Catalysis* **1,** 385–397 (2018).
6. Samantaray, M. K. *et al.* The comparison between single atom catalysis and surface organometallic catalysis. *Chemical reviews* **120,** 734–813 (2019).
7. Parkinson, G. S. Single-atom catalysis: How structure influences catalytic performance. *Catalysis letters* **149,** 1137–1146 (2019).
8. Abbet, S. *et al.* Acetylene cyclotrimerization on supported size-selected Pd_n clusters ($1 \leq n \leq 30$): one atom is enough! *Journal of the American Chemical Society* **122,** 3453–3457 (2000).
9. Fu, Q., Saltsburg, H. & Flytzani-Stephanopoulos, M. Active nonmetallic Au and Pt species on ceria-based water-gas shift catalysts. *Science* **301,** 935–938 (2003).
10. Flytzani-Stephanopoulos, M. & Gates, B. C. Atomically dispersed supported metal catalysts. *Annual review of chemical and biomolecular engineering* **3,** 545–574 (2012).

Die approbierte gedruckte Originalversion dieser Dissertation ist an der TU Wien Bibliothek verfügbar.
The approved original version of this doctoral thesis is available in print at TU Wien Bibliothek.
TU Bibliothek Your knowledge hub WIEN

11. Qiao, B. *et al.* Single-atom catalysis of CO oxidation using Pt_1/FeO_x. *Nature chemistry* **3,** 634–641 (2011).

12. Wang, Y. *et al.* Catalysis with two-dimensional materials confining single atoms: concept, design, and applications. *Chemical reviews* **119,** 1806–1854 (2018).

13. Chen, Y. *et al.* Single-atom catalysts: synthetic strategies and electrochemical applications. *Joule* **2,** 1242–1264 (2018).

14. Shang, Y., Xu, X., Gao, B., Wang, S. & Duan, X. Single-atom catalysis in advanced oxidation processes for environmental remediation. *Chemical Society Reviews* **50,** 5281–5322 (2021).

15. Yang, M., Allard, L. F. & Flytzani-Stephanopoulos, M. Atomically dispersed Au–$(OH)_x$ species bound on titania catalyze the low-temperature water-gas shift reaction. *Journal of the American Chemical Society* **135,** 3768–3771 (2013).

16. Lin, J. *et al.* Remarkable performance of Ir_1/FeO_x single-atom catalyst in water gas shift reaction. *Journal of the American Chemical Society* **135,** 15314–15317 (2013).

17. Wei, H. *et al.* FeO_x-supported platinum single-atom and pseudo-single-atom catalysts for chemoselective hydrogenation of functionalized nitroarenes. *Nature communications* **5,** 5634 (2014).

18. Zhang, L., Zhou, M., Wang, A. & Zhang, T. Selective hydrogenation over supported metal catalysts: from nanoparticles to single atoms. *Chemical reviews* **120,** 683–733 (2019).

19. Thomas, J. M. *Design and applications of single-site heterogeneous catalysts: contributions to green chemistry, clean technology and sustainability* (World Scientific Publishing Company, 2012).

20. Liu, J. Catalysis by supported single metal atoms. *Acs Catalysis* **7,** 34–59 (2017).

21. Liu, J. Aberration-corrected scanning transmission electron microscopy in single-atom catalysis: Probing the catalytically active centers. *Chinese Journal of Catalysis* **38,** 1460–1472 (2017).

Die approbierte gedruckte Originalversion dieser Dissertation ist an der TU Wien Bibliothek verfügbar.
The approved original version of this doctoral thesis is available in print at TU Wien Bibliothek.
TU Bibliothek Your knowledge hub WIEN

22. Hoffmann, M. R., Martin, S. T., Choi, W. & Bahnemann, D. W. Environmental applications of semiconductor photocatalysis. *Chemical reviews* **95,** 69–96 (1995).

23. Linsebigler, A. L., Lu, G. & Yates Jr, J. T. Photocatalysis on TiO_2 surfaces: principles, mechanisms, and selected results. *Chemical reviews* **95,** 735–758 (1995).

24. Kalyanasundaram, K. & Grätzel, M. Applications of functionalized transition metal complexes in photonic and optoelectronic devices. *Coordination chemistry reviews* **177,** 347–414 (1998).

25. Grätzel, M. Dye-sensitized solar cells. *Journal of photochemistry and photobiology C: Photochemistry Reviews* **4,** 145–153 (2003).

26. Gong, J., Li, Y., Hu, Z., Zhou, Z. & Deng, Y. Ultrasensitive NH_3 gas sensor from polyaniline nanograin enchased TiO_2 fibers. *The Journal of Physical Chemistry C* **114,** 9970–9974 (2010).

27. Mun, K.-S., Alvarez, S. D., Choi, W.-Y. & Sailor, M. J. A stable, label-free optical interferometric biosensor based on TiO_2 nanotube arrays. *ACS nano* **4,** 2070–2076 (2010).

28. Bao, S.-J. *et al.* New nanostructured TiO_2 for direct electrochemistry and glucose sensor applications. *Advanced Functional Materials* **18,** 591–599 (2008).

29. Braun, J. H., Baidins, A. & Marganski, R. E. TiO_2 pigment technology: a review. *Progress in organic coatings* **20,** 105–138 (1992).

30. Grant, F. Properties of rutile (titanium dioxide). *Reviews of Modern Physics* **31,** 646 (1959).

31. Samsonov Grigori, V. *The oxide handbook* (Springer Science & Business Media, 2013).

32. Diebold, U. The surface science of titanium dioxide. *Surface science reports* **48,** 53–229 (2003).

33. O'regan, B. & Grätzel, M. A low-cost, high-efficiency solar cell based on dye-sensitized colloidal TiO_2 films. *nature* **353,** 737–740 (1991).

34. Chen, X. & Mao, S. S. Titanium dioxide nanomaterials: synthesis, properties, modifications, and applications. *Chemical reviews* **107,** 2891–2959 (2007).

Die approbierte gedruckte Originalversion dieser Dissertation ist an der TU Wien Bibliothek verfügbar.
The approved original version of this doctoral thesis is available in print at TU Wien Bibliothek.
TU Bibliothek Your knowledge hub WIEN

35. Amores, J. M. G., Escribano, V. S., *et al.* Anatase crystal growth and phase transformation to rutile in high-area TiO_2, MoO_3–TiO_2 and other TiO_2-supported oxide catalytic systems. *Journal of Materials Chemistry* **5,** 1245–1249 (1995).

36. Treacy, J. P. *et al.* Geometric structure of anatase TiO_2(101). *Physical Review B* **95,** 075416 (2017).

37. Hengerer, R., Bolliger, B., Erbudak, M. & Grätzel, M. Structure and stability of the anatase TiO_2(101) and (001) surfaces. *Surface science* **460,** 162–169 (2000).

38. Pang, C. L., Lindsay, R. & Thornton, G. Chemical reactions on rutile TiO_2(110). *Chemical Society Reviews* **37,** 2328–2353 (2008).

39. Dohnálek, Z., Lyubinetsky, I. & Rousseau, R. Thermally-driven processes on rutile TiO_2(110)-(1×1): A direct view at the atomic scale. *Progress in Surface Science* **85,** 161–205 (2010).

40. Tasker, P. The stability of ionic crystal surfaces. *Journal of Physics C: Solid State Physics* **12,** 4977 (1979).

41. Kavan, L., Grätzel, M., Gilbert, S., Klemenz, C. & Scheel, H. Electrochemical and photoelectrochemical investigation of single-crystal anatase. *Journal of the American Chemical Society* **118,** 6716–6723 (1996).

42. Lindsay, R. *et al.* Revisiting the surface structure of TiO_2(110): a quantitative low-energy electron diffraction study. *Physical review letters* **94,** 246102 (2005).

43. Cabailh, G. *et al.* Geometric structure of TiO_2(110) (1×1): Achieving experimental consensus. *Physical Review B* **75,** 241403 (2007).

44. Reticcioli, M. *et al.* Polaron-driven surface reconstructions. *Physical Review X* **7,** 031053 (2017).

45. Busayaporn, W. *et al.* Geometric structure TiO_2(110)(1×1): confirming experimental conclusions. *Physical Review B* **81,** 153404 (2010).

46. Henderson, M. A. A surface perspective on self-diffusion in rutile TiO_2. *Surface Science* **419,** 174–187 (1999).

47. Diebold, U., Anderson, J. F., Ng, K.-O. & Vanderbilt, D. Evidence for the Tunneling Site on Transition-Metal Oxides: TiO_2(110). *Physical review letters* **77,** 1322 (1996).

Die approbierte gedruckte Originalversion dieser Dissertation ist an der TU Wien Bibliothek verfügbar.
The approved original version of this doctoral thesis is available in print at TU Wien Bibliothek.
TU Bibliothek Your knowledge hub WIEN

48. Tanner, R., Castell, M. & Briggs, G. High resolution scanning tunnelling microscopy of the rutile TiO_2(110) surface. *Surface science* **412,** 672–681 (1998).

49. Hugenschmidt, M. B., Gamble, L. & Campbell, C. T. The interaction of H_2O with a TiO_2(110) surface. *Surface Science* **302,** 329–340 (1994).

50. Lee, J., Sorescu, D. C., Deng, X. & Jordan, K. D. Water chain formation on TiO_2(110). *The journal of physical chemistry letters* **4,** 53–57 (2013).

51. Schaub, R. *et al.* Oxygen vacancies as active sites for water dissociation on rutile TiO_2(110). *Physical Review Letters* **87,** 266104 (2001).

52. Wendt, S. *et al.* Oxygen vacancies on TiO_2(110) and their interaction with H_2O and O_2: A combined high-resolution STM and DFT study. *Surface Science* **598,** 226–245 (2005).

53. Du, Y. *et al.* Imaging consecutive steps of O_2 reaction with hydroxylated TiO_2(110): Identification of HO_2 and terminal OH intermediates. *The Journal of Physical Chemistry C* **113,** 666–671 (2009).

54. Silversmit, G., Poelman, H., Fiermans, L. & De Gryse, R. An X-ray photoelectron diffraction study of a TiO_2(001) anatase single crystal mineral. *Solid state communications* **119,** 101–104 (2001).

55. Poelman, H. & Fiermans, L. Surface phonon spectra of mineral TiO_2 anatase (001) and (100). *Surface Science Spectra* **5,** 252–256 (1998).

56. Diebold, U., Ruzycki, N., Herman, G. S. & Selloni, A. One step towards bridging the materials gap: surface studies of TiO_2 anatase. *Catalysis today* **85,** 93–100 (2003).

57. Setvin, M. *et al.* Surface preparation of TiO_2 anatase (101): Pitfalls and how to avoid them. *Surface science* **626,** 61–67 (2014).

58. Setvin, M. *et al.* Reaction of O_2 with subsurface oxygen vacancies on TiO_2 anatase (101). *Science* **341,** 988–991 (2013).

59. Scheiber, P. *et al.* (Sub) Surface mobility of oxygen vacancies at the TiO_2 anatase(101) surface. *Physical review letters* **109,** 136103 (2012).

60. He, Y., Dulub, O., Cheng, H., Selloni, A. & Diebold, U. Evidence for the predominance of subsurface defects on reduced anatase TiO_2(101). *Physical Review Letters* **102,** 106105 (2009).

Die approbierte gedruckte Originalversion dieser Dissertation ist an der TU Wien Bibliothek verfügbar.
The approved original version of this doctoral thesis is available in print at TU Wien Bibliothek.
TU Bibliothek Your knowledge hub WIEN

61. Herman, G. S., Dohnalek, Z., Ruzycki, N. & Diebold, U. Experimental investigation of the interaction of water and methanol with anatase-TiO_2(101). *The Journal of Physical Chemistry B* **107,** 2788–2795 (2003).

62. Dictor, R. A. & Bell, A. T. Fischer-Tropsch synthesis over reduced and unreduced iron oxide catalysts. *Journal of Catalysis* **97,** 121–136 (1986).

63. Weiss, W. & Ranke, W. Surface chemistry and catalysis on well-defined epitaxial iron-oxide layers. *Progress in Surface Science* **70,** 1–151 (2002).

64. Munoz, M., de Pedro, Z. M., Casas, J. A. & Rodriguez, J. J. Preparation of magnetite-based catalysts and their application in heterogeneous Fenton oxidation—a review. *Applied Catalysis B: Environmental* **176,** 249–265 (2015).

65. Tartaj, P., Morales, M. P., Gonzalez-Carreño, T., Veintemillas-Verdaguer, S. & Serna, C. J. The Iron Oxides Strike Back: From Biomedical Applications to Energy Storage Devices and Photoelectrochemical Water Splitting. *Advanced Materials* **44,** 5243–5249 (2011).

66. Dilnawaz, F., Singh, A., Mohanty, C. & Sahoo, S. K. Dual drug loaded superparamagnetic iron oxide nanoparticles for targeted cancer therapy. *Biomaterials* **31,** 3694–3706 (2010).

67. Block, T. & Schmücker, M. Metal oxides for thermochemical energy storage: A comparison of several metal oxide systems. *Solar Energy* **126,** 195–207 (2016).

68. Ketteler, G., Weiss, W., Ranke, W. & Schlögl, R. Bulk and surface phases of iron oxides in an oxygen and water atmosphere at low pressure. *Physical Chemistry Chemical Physics* **3,** 1114–1122 (2001).

69. Pauling, L. & Hendricks, S. B. The crystal structures of hematite and corundum. *Journal of the American Chemical Society* **47,** 781–790 (1925).

70. Maslen, E., Streltsov, V., Streltsova, N. & Ishizawa, N. Synchrotron X-ray study of the electron density in α-Fe_2O_3. *Acta Crystallographica Section B: Structural Science* **50,** 435–441 (1994).

71. Tamirat, A. G., Rick, J., Dubale, A. A., Su, W.-N. & Hwang, B.-J. Using hematite for photoelectrochemical water splitting: a review of current progress and challenges. *Nanoscale horizons* **1,** 243–267 (2016).

Die approbierte gedruckte Originalversion dieser Dissertation ist an der TU Wien Bibliothek verfügbar.
The approved original version of this doctoral thesis is available in print at TU Wien Bibliothek.
TU Bibliothek Your knowledge hub WIEN

72. Kraushofer, F. *et al.* Atomic-scale structure of the hematite α-$Fe_2O_3(1\bar{1}02)$ "R-Cut" Surface. *The Journal of Physical Chemistry C* **122,** 1657–1669 (2018).

73. Sivula, K., Le Formal, F. & Grätzel, M. Solar water splitting: progress using hematite (α-Fe_2O_3) photoelectrodes. *ChemSusChem* **4,** 432–449 (2011).

74. Zboril, R., Mashlan, M. & Petridis, D. Iron (III) oxides from thermal processes synthesis, structural and magnetic properties, Mössbauer spectroscopy characterization, and applications. *Chemistry of Materials* **14,** 969–982 (2002).

75. Warnes, B., Aplan, F. & Simkovich, G. Electrical conductivity and seebeck voltage of Fe_2O_3, pure and doped, as a function of temperature and oxygen pressure. *Solid State Ionics* **12,** 271–276 (1984).

76. Morin, F. Electrical properties of α-Fe_2O_3 and α-Fe_2O_3 containing titanium. *Physical Review* **83,** 1005 (1951).

77. Nakau, T. Electrical conductivity of α-Fe_2O_3. *Journal of the Physical Society of Japan* **15,** 727–727 (1960).

78. Le Formal, F. *et al.* Passivating surface states on water splitting hematite photoanodes with alumina overlayers. *Chemical Science* **2,** 737–743 (2011).

79. Parkinson, G. S. Iron oxide surfaces. *Surface Science Reports* **71,** 272–365 (2016).

80. Kuhlenbeck, H., Shaikhutdinov, S. & Freund, H.-J. Well-ordered transition metal oxide layers in model catalysis—a series of case studies. *Chemical reviews* **113,** 3986–4034 (2013).

81. Lad, R. J. & Henrich, V. E. Structure of α-Fe_2O_3 single crystal surfaces following Ar^+ ion bombardment and annealing in O_2. *Surface Science* **193,** 81–93 (1988).

82. Gautier-Soyer, M., Pollak, M., Henriot, M. & Guittet, M. The (1×2) reconstruction of the α-$Fe_2O_3(1\bar{1}02)$ surface. *Surface science* **352,** 112–116 (1996).

83. Henderson, M. A. Low temperature oxidation of Fe^{2+} surface sites on the (2×1) reconstructed surface of α-$Fe_2O_3(1\bar{1}02)$. *Surface science* **604,** 1197–1201 (2010).

Die approbierte gedruckte Originalversion dieser Dissertation ist an der TU Wien Bibliothek verfügbar.
The approved original version of this doctoral thesis is available in print at TU Wien Bibliothek.
TU Bibliothek Your knowledge hub WIEN

84. Wang, J. & Rustad, J. R. A simple model for the effect of hydration on the distribution of ferrous iron at reduced hematite (012) surfaces. *Geochimica et cosmochimica acta* **70,** 5285–5292 (2006).

85. Henderson, M. A. Insights into the (1×1)-to-(2×1) phase transition of the α-Fe_2O_3(012) surface using EELS, LEED and water TPD. *Surface science* **515,** 253–262 (2002).

86. Sugimoto, Y. *et al.* Chemical identification of individual surface atoms by atomic force microscopy. *Nature* **446,** 64–67 (2007).

87. Enevoldsen, G. H. *et al.* Detailed scanning probe microscopy tip models determined from simultaneous atom-resolved AFM and STM studies of the TiO_2(110) surface. *Physical Review B—Condensed Matter and Materials Physics* **78,** 045416 (2008).

88. Enevoldsen, G. H., Foster, A. S., Christensen, M. C., Lauritsen, J. V. & Besenbacher, F. Noncontact atomic force microscopy studies of vacancies and hydroxyls of TiO_2(110): Experiments and atomistic simulations. *Physical Review B—Condensed Matter and Materials Physics* **76,** 205415 (2007).

89. Gross, L., Mohn, F., Moll, N., Liljeroth, P. & Meyer, G. The chemical structure of a molecule resolved by atomic force microscopy. *Science* **325,** 1110–1114 (2009).

90. Hapala, P. *et al.* Mechanism of high-resolution STM/AFM imaging with functionalized tips. *Physical Review B* **90,** 085421 (2014).

91. Yurtsever, A. *et al.* Understanding image contrast formation in TiO_2 with force spectroscopy. *Physical Review B—Condensed Matter and Materials Physics* **85,** 125416 (2012).

92. Franceschi, G. *et al.* A model system for photocatalysis: Ti-doped α-$Fe_2O_3(1\bar{1}02)$ single-crystalline films. *Chemistry of Materials* **32,** 3753–3764 (2020).

93. Jakub, Z. *et al.* Partially dissociated water dimers at the water-hematite interface. *ACS Energy Letters* **4,** 390–396 (2019).

94. Henderson, M. A., Joyce, S. A. & Rustad, J. R. Interaction of water with the (1×1) and (2×1) surfaces of α-Fe_2O_3(012). *Surface Science* **417,** 66–81 (1998).

Die approbierte gedruckte Originalversion dieser Dissertation ist an der TU Wien Bibliothek verfügbar.
The approved original version of this doctoral thesis is available in print at TU Wien Bibliothek.
TU Bibliothek Your knowledge hub WIEN

95. Balajka, J. *et al.* High-affinity adsorption leads to molecularly ordered interfaces on TiO_2 in air and solution. *Science* **361,** 786–789 (2018).

96. Balajka, J., Pavelec, J., Komora, M., Schmid, M. & Diebold, U. Apparatus for dosing liquid water in ultrahigh vacuum. *Review of Scientific Instruments* **89** (2018).

97. Taimoory, S. M. *et al.* Importance of the inter-electrode distance for the electrochemical synthesis of magnetite nanoparticles: synthesis, characterization, computational modelling, and cytotoxicity. *e-Journal of Surface Science and Nanotechnology* **15,** 31–39 (2017).

98. Verwey, E. Electronic conduction of magnetite (Fe_3O_4) and its transition point at low temperatures. *Nature* **144,** 327–328 (1939).

99. Néel, L. *Propriétés magnétiques des ferrites; ferrimagnétisme et antiferromagnétisme* in *Annales de physique* **12** (1948), 137–198.

100. Cornell, R. M., Schwertmann, U., *et al. The iron oxides: structure, properties, reactions, occurrences, and uses* (Wiley-vch Weinheim, 2003).

101. Yu, X., Huo, C.-F., Li, Y.-W., Wang, J. & Jiao, H. Fe_3O_4 surface electronic structures and stability from GGA+U. *Surface Science* **606,** 872–879 (2012).

102. Santos-Carballal, D., Roldan, A., Grau-Crespo, R. & de Leeuw, N. H. A DFT study of the structures, stabilities and redox behaviour of the major surfaces of magnetite Fe_3O_4. *Physical Chemistry Chemical Physics* **16,** 21082–21097 (2014).

103. Tao, Y. *et al.* Surface structures of Fe_3O_4(111), (110), and (001): A density functional theory study. *Journal of Fuel Chemistry and Technology* **38,** 121–128 (2010).

104. Bliem, R. *et al.* Subsurface cation vacancy stabilization of the magnetite (001) surface. *Science* **346,** 1215–1218 (2014).

105. Arndt, B. *et al.* Atomic structure and stability of magnetite Fe_3O_4(001): An X-ray view. *Surface Science* **653,** 76–81 (2016).

106. Noh, J., Osman, O. I., Aziz, S. G., Winget, P. & Bredas, J.-L. Magnetite Fe_3O_4(111) surfaces: impact of defects on structure, stability, and electronic properties. *Chemistry of Materials* **27,** 5856–5867 (2015).

Die approbierte gedruckte Originalversion dieser Dissertation ist an der TU Wien Bibliothek verfügbar.
The approved original version of this doctoral thesis is available in print at TU Wien Bibliothek.
TU Bibliothek Your knowledge hub WIEN

107. Sala, A. *et al.* Defects and inhomogeneities in $Fe_3O_4(111)$ thin film growth on Pt(111). *Physical Review B—Condensed Matter and Materials Physics* **86,** 155430 (2012).

108. Barbieri, A., Weiss, W., Van Hove, M. & Somorjai, G. Magnetite $Fe_3O_4(111)$: surface structure by LEED crystallography and energetics. *Surface Science* **302,** 259–279 (1994).

109. Shimizu, T. K., Jung, J., Kato, H. S., Kim, Y. & Kawai, M. Termination and Verwey transition of the (111) surface of magnetite studied by scanning tunneling microscopy and first-principles calculations. *Physical Review B—Condensed Matter and Materials Physics* **81,** 235429 (2010).

110. Li, X. *et al.* Surface termination of $Fe_3O_4(111)$ films studied by CO adsorption revisited. *The Journal of Physical Chemistry B* **122,** 527–533 (2018).

111. Mirabella, F. *et al.* Cooperative Formation of Long-Range Ordering in Water Ad-layers on $Fe_3O_4(111)$ Surfaces. *Angewandte Chemie International Edition* **57,** 1409–1413 (2018).

112. Pentcheva, R. *et al.* Jahn-Teller stabilization of a "polar" metal oxide surface: $Fe_3O_4(001)$. *Physical review letters* **94,** 126101 (2005).

113. Łodziana, Z. Surface Verwey transition in magnetite. *Physical review letters* **99,** 206402 (2007).

114. Pentcheva, R. *et al.* A combined DFT/LEED-approach for complex oxide surface structure determination: $Fe_3O_4(001)$. *Surface Science* **602,** 1299–1305 (2008).

115. Wiesendanger, R. *et al.* Topographic and magnetic-sensitive scanning tunneling microscope study of magnetite. *Science* **255,** 583–586 (1992).

116. Stanka, B., Hebenstreit, W., Diebold, U. & Chambers, S. Surface reconstruction of $Fe_3O_4(001)$. *Surface science* **448,** 49–63 (2000).

117. Novotnỳ, Z. *et al.* Ordered array of single adatoms with remarkable thermal stability: $Au/Fe_3O_4(001)$. *Physical review letters* **108,** 216103 (2012).

118. Bliem, R. *et al.* Adsorption and incorporation of transition metals at the magnetite $Fe_3O_4(001)$ surface. *Physical Review B* **92,** 075440 (2015).

Die approbierte gedruckte Originalversion dieser Dissertation ist an der TU Wien Bibliothek verfügbar.
The approved original version of this doctoral thesis is available in print at TU Wien Bibliothek.
TU Bibliothek Your knowledge hub WIEN

119. Ryan, P. *et al.* Direct measurement of Ni incorporation into Fe_3O_4(001). *Physical Chemistry Chemical Physics* **20,** 16469–16476 (2018).

120. Parkinson, G. S., Novotný, Z., Jacobson, P., Schmid, M. & Diebold, U. Room temperature water splitting at the surface of magnetite. *Journal of the American Chemical Society* **133,** 12650–12655 (2011).

121. Parkinson, G. S. *et al.* Antiphase domain boundaries at the Fe_3O_4(001) surface. *Physical Review B—Condensed Matter and Materials Physics* **85,** 195450 (2012).

122. Gamba, O. *et al.* The role of surface defects in the adsorption of methanol on Fe_3O_4(001). *Topics in Catalysis* **60,** 420–430 (2017).

123. Kraushofer, F. *et al.* Self-limited growth of an oxyhydroxide phase at the Fe_3O_4(001) surface in liquid and ambient pressure water. *The Journal of Chemical Physics* **151** (2019).

124. Binnig, G. & Rohrer, H. Scanning tunneling microscopy. *Surface science* **126,** 236–244 (1983).

125. Binnig, G. & Rohrer, H. Scanning tunneling microscopy—from birth to adolescence. *reviews of modern physics* **59,** 615 (1987).

126. Tersoff, J. & Hamann, D. R. Theory of the scanning tunneling microscope. *Physical Review B* **31,** 805 (1985).

127. Giessibl, F. J. The qPlus sensor, a powerful core for the atomic force microscope. *Review of scientific instruments* **90** (2019).

128. Pavelec, J. *et al.* A multi-technique study of CO_2 adsorption on Fe_3O_4 magnetite. *The Journal of Chemical Physics* **146** (2017).

129. Tait, S. L., Dohnálek, Z., Campbell, C. T. & Kay, B. D. n-alkanes on MgO(100). I. Coverage-dependent desorption kinetics of n-butane. *The Journal of chemical physics* **122** (2005).

130. Schmid, M., Parkinson, G. S. & Diebold, U. Analysis of temperature-programmed desorption via equilibrium thermodynamics. *ACS physical chemistry Au* **3,** 44–62 (2022).

Die approbierte gedruckte Originalversion dieser Dissertation ist an der TU Wien Bibliothek verfügbar.
The approved original version of this doctoral thesis is available in print at TU Wien Bibliothek.
TU Bibliothek Your knowledge hub WIEN

131. Kresse, G. & Furthmüller, J. Efficiency of ab-initio total energy calculations for metals and semiconductors using a plane-wave basis set. *Computational materials science* **6,** 15–50 (1996).

132. Sombut, P. *et al.* Role of Polarons in Single-Atom Catalysts: Case Study of Me_1 [Au_1, Pt_1, and Rh_1] on TiO_2(110). *Topics in Catalysis* **65,** 1620–1630 (2022).

133. Puntscher, L. *et al.* A Multitechnique Study of C_2H_4 Adsorption on Fe_3O_4(001). *The Journal of Physical Chemistry C* **127,** 18378–18388 (2023).

134. Wang, C. *et al.* A Multitechnique Study of C_2H_4 Adsorption on a Model Single-Atom Rh_1 Catalyst. *The Journal of Physical Chemistry C* **128,** 15404–15411 (2024).

135. Huber, F. & Giessibl, F. J. Low noise current preamplifier for qPlus sensor deflection signal detection in atomic force microscopy at room and low temperatures. *Review of Scientific Instruments* **88** (2017).

136. Pavelec, J. *Surface chemistry setup and adsorption of CO_2 on Fe_3O_4(001)* PhD thesis (Technische Universität Wien, 2019).

137. Halwidl, D. *Development of an effusive molecular beam apparatus* (Springer, 2016).

138. Rath, D. *et al.* Infrared reflection absorption spectroscopy setup with incidence angle selection for surfaces of non-metals. *Review of Scientific Instruments* **95** (2024).

139. Puntscher, L., Daninger, K., Schmid, M., Diebold, U. & Parkinson, G. S. A study of Pt, Rh, Ni and Ir dispersion on anatase TiO_2(101) and the role of water. *Electrochimica Acta* **449,** 142190 (2023).

140. Kraushofer, F. & Parkinson, G. S. Single-atom catalysis: Insights from model systems. *Chemical Reviews* **122,** 14911–14939 (2022).

141. Mellor, A. *et al.* Direct visualization of Au atoms bound to TiO_2(110) O-vacancies. *The Journal of Physical Chemistry C* **121,** 24721–24725 (2017).

142. Wahlström, E. *et al.* Bonding of gold nanoclusters to oxygen vacancies on rutile TiO_2(110). *Physical review letters* **90,** 026101 (2003).

Die approbierte gedruckte Originalversion dieser Dissertation ist an der TU Wien Bibliothek verfügbar.
The approved original version of this doctoral thesis is available in print at TU Wien Bibliothek.
TU Bibliothek Your knowledge hub WIEN

143. Dong, S.-h., Wang, A.-l., Zhao, J., Tan, S.-j. & Wang, B. Interaction of CO and O_2 with supported Pt single-atoms on TiO_2(110). *Chinese Journal of Chemical Physics* **33,** 349–356 (2020).

144. Luo, K., St. Clair, T., Lai, X. & Goodman, D. Silver Growth on TiO_2(110) (1×1) and (1×2). *The Journal of Physical Chemistry B* **104,** 3050–3057 (2000).

145. Zhou, J., Kang, Y., Ma, S. & Chen, D. Adsorbate-induced dissociation of metal clusters: TiO_2(110)-supported Cu and Ni clusters exposed to oxygen gas. *Surface science* **562,** 113–127 (2004).

146. Fujikawa, K., Suzuki, S., Koike, Y., Chun, W.-J. & Asakura, K. Self-regulated Ni cluster formation on the TiO_2(110) terrace studied using scanning tunneling microscopy. *Surface science* **600,** 117–121 (2006).

147. Xu, C., Lai, X., Zajac, G. & Goodman, D. Scanning tunneling microscopy studies of the TiO_2(110) surface: structure and the nucleation growth of Pd. *Physical Review B* **56,** 13464 (1997).

148. Dong, S., Li, B., Cui, X., Tan, S. & Wang, B. Photoresponses of supported Au single atoms on TiO_2(110) through the metal-induced gap states. *The Journal of Physical Chemistry Letters* **10,** 4683–4691 (2019).

149. Tang, Y. *et al.* Rh single atoms on TiO_2 dynamically respond to reaction conditions by adapting their site. *Nature communications* **10,** 4488 (2019).

150. Gong, X.-Q., Selloni, A., Dulub, O., Jacobson, P. & Diebold, U. Small Au and Pt clusters at the anatase TiO_2(101) surface: behavior at terraces, steps, and surface oxygen vacancies. *Journal of the American Chemical Society* **130,** 370–381 (2008).

151. Saavedra, J., Doan, H. A., Pursell, C. J., Grabow, L. C. & Chandler, B. D. The critical role of water at the gold-titania interface in catalytic CO oxidation. *Science* **345,** 1599–1602 (2014).

152. Wang, C. *et al.* Water-mediated Mars-van Krevelen mechanism for CO oxidation on ceria-supported single-atom Pt_1 catalyst. *Acs Catalysis* **7,** 887–891 (2017).

Die approbierte gedruckte Originalversion dieser Dissertation ist an der TU Wien Bibliothek verfügbar.
The approved original version of this doctoral thesis is available in print at TU Wien Bibliothek.
TU Bibliothek Your knowledge hub WIEN

153. Thang, H. V., Pacchioni, G., DeRita, L. & Christopher, P. Nature of stable single atom Pt catalysts dispersed on anatase TiO_2. *Journal of Catalysis* **367,** 104–114 (2018).

154. DeRita, L. *et al.* Catalyst architecture for stable single atom dispersion enables site-specific spectroscopic and reactivity measurements of CO adsorbed to Pt atoms, oxidized Pt clusters, and metallic Pt clusters on TiO_2. *Journal of the American Chemical Society* **139,** 14150–14165 (2017).

155. Matthey, D. *et al.* Enhanced bonding of gold nanoparticles on oxidized $TiO_2(110)$. *Science* **315,** 1692–1696 (2007).

156. Hansen, J. Ø. *et al.* Enhanced bonding of silver nanoparticles on oxidized $TiO_2(110)$. *The Journal of Physical Chemistry C* **114,** 16964–16972 (2010).

157. Mellor, A. *et al.* Photoemission core level binding energies from multiple sized nanoparticles on the same support: $TiO_2(110)$/Au. *The Journal of Chemical Physics* **152** (2020).

158. Wang, X., Zhang, L., Bu, Y. & Sun, W. Interplay between invasive single atom Pt and native oxygen vacancy in rutile $TiO_2(110)$ surface: A theoretical study. *Nano Research* **15,** 669–676 (2022).

159. Kraushofer, F. *et al.* Single Rh adatoms stabilized on α-$Fe_2O_3(1\bar{1}02)$ by coadsorbed water. *ACS Energy Letters* **7,** 375–380 (2021).

160. Setvin, M. *et al.* Formaldehyde adsorption on the anatase $TiO_2(101)$ surface: experimental and theoretical investigation. *The Journal of Physical Chemistry C* **121,** 8914–8922 (2017).

161. Setvin, M. *et al.* A multitechnique study of CO adsorption on the TiO_2 anatase (101) surface. *The Journal of Physical Chemistry C* **119,** 21044–21052 (2015).

162. Setvin, M. *et al.* Identification of adsorbed molecules via STM tip manipulation: CO, H_2O, and O_2 on TiO_2 anatase (101). *Physical Chemistry Chemical Physics* **16,** 21524–21530 (2014).

163. Setvin, M., Hulva, J., Parkinson, G. S., Schmid, M. & Diebold, U. Electron transfer between anatase TiO_2 and an O_2 molecule directly observed by atomic force microscopy. *Proceedings of the National Academy of Sciences* **114,** E2556–E2562 (2017).

Die approbierte gedruckte Originalversion dieser Dissertation ist an der TU Wien Bibliothek verfügbar.
The approved original version of this doctoral thesis is available in print at TU Wien Bibliothek.
TU Bibliothek Your knowledge hub WIEN

164. Jin, C. *et al.* Effects of single metal atom (Pt, Pd, Rh and Ru) adsorption on the photocatalytic properties of anatase TiO_2. *Applied Surface Science* **426,** 639–646 (2017).

165. Han, Y., Liu, C.-j. & Ge, Q. Interaction of Pt clusters with the anatase $TiO_2(101)$ surface: A first principles study. *The Journal of Physical Chemistry B* **110,** 7463–7472 (2006).

166. Mao, Z. & Campbell, C. T. Predicting a key catalyst-performance descriptor for supported metal nanoparticles: Metal chemical potential. *ACS Catalysis* **11,** 8284–8291 (2021).

167. Chastain, J. & King Jr, R. C. Handbook of X-ray photoelectron spectroscopy. *Perkin-Elmer Corporation* **40,** 221 (1992).

168. Zhou, Y., Muhich, C. L., Neltner, B. T., Weimer, A. W. & Musgrave, C. B. Growth of Pt particles on the anatase $TiO_2(101)$ surface. *The Journal of Physical Chemistry C* **116,** 12114–12123 (2012).

169. Setvin, M., Schmid, M. & Diebold, U. Aggregation and electronically induced migration of oxygen vacancies in TiO_2 anatase. *Physical Review B* **91,** 195403 (2015).

170. Hebenstreit, W., Ruzycki, N., Herman, G. S., Gao, Y. & Diebold, U. Scanning tunneling microscopy investigation of the TiO_2 anatase (101) surface. *Physical Review B* **62,** R16334 (2000).

171. Li, F., Li, Y., Zeng, X. C. & Chen, Z. Exploration of high-performance single-atom catalysts on support M_1/FeO_x for CO oxidation via computational study. *Acs Catalysis* **5,** 544–552 (2015).

172. Qiao, B. *et al.* Ultrastable single-atom gold catalysts with strong covalent metal-support interaction (CMSI). *Nano Research* **8,** 2913–2924 (2015).

173. Rafsanjani-Abbasi, A. *et al.* Digging Its Own Site: Linear Coordination Stabilizes a Pt_1/Fe_2O_3 Single-Atom Catalyst. *ACS nano* (2024).

174. Kraushofer, F. *et al.* Surface Reduction State Determines Stabilization and Incorporation of Rh on α-$Fe_2O_3(1\bar{1}02)$. *Advanced Materials Interfaces* **8,** 2001908 (2021).

Die approbierte gedruckte Originalversion dieser Dissertation ist an der TU Wien Bibliothek verfügbar.
The approved original version of this doctoral thesis is available in print at TU Wien Bibliothek.
TU Bibliothek Your knowledge hub WIEN

175. Jakub, Z. *et al.* Local structure and coordination define adsorption in a model Ir_1/Fe_3O_4 single-atom catalyst. *Angewandte Chemie International Edition* **58,** 13961–13968 (2019).

176. Jakub, Z. *et al.* Adsorbate-induced structural evolution changes the mechanism of CO oxidation on a $Rh/Fe_3O_4(001)$ model catalyst. *Nanoscale* **12,** 5866–5875 (2020).

177. Hulva, J. *et al.* Adsorption of CO on the $Fe_3O_4(001)$ Surface. *The Journal of Physical Chemistry B* **122,** 721–729 (2018).

178. Parkinson, G. S. *et al.* Semiconductor–half metal transition at the $Fe_3O_4(001)$ surface upon hydrogen adsorption. *Physical Review B—Condensed Matter and Materials Physics* **82,** 125413 (2010).

179. Hiura, S., Ikeuchi, A., Shirini, S., Subagyo, A. & Sueoka, K. Effect of adsorbed H atoms on the Fe electronic states of $Fe_3O_4(001)$ film surfaces. *Physical Review B* **91,** 205411 (2015).

180. Wang, C. *et al.* CO-induced dimer decay responsible for gem-dicarbonyl formation on a model single-atom catalyst. *Angewandte Chemie* **136,** e202317347 (2024).

181. Bliem, R. *et al.* Cluster nucleation and growth from a highly supersaturated adatom phase: silver on magnetite. *Acs Nano* **8,** 7531–7537 (2014).

182. Meier, M. *et al.* Probing the geometry of copper and silver adatoms on magnetite: quantitative experiment versus theory. *Nanoscale* **10,** 2226–2230 (2018).

183. Gargallo-Caballero, R. *et al.* Co on $Fe_3O_4(001)$: Towards precise control of surface properties. *The Journal of Chemical Physics* **144** (2016).

184. Hulva, J. *et al.* Unraveling CO adsorption on model single-atom catalysts. *Science* **371,** 375–379 (2021).

185. Wikipedia. *Hydroformylation* `https://en.wikipedia.org/wiki/Hydroformylation`.

186. Wodrich, M. D., Busch, M. & Corminboeuf, C. Accessing and predicting the kinetic profiles of homogeneous catalysts from volcano plots. *Chemical science* **7,** 5723–5735 (2016).

187. Franke, R., Selent, D. & Börner, A. Applied hydroformylation. *Chemical reviews* **112,** 5675–5732 (2012).

Die approbierte gedruckte Originalversion dieser Dissertation ist an der TU Wien Bibliothek verfügbar.
The approved original version of this doctoral thesis is available in print at TU Wien Bibliothek.
TU Bibliothek Your knowledge hub WIEN

188. Van Leeuwen, P. W. & Claver, C. *Rhodium catalyzed hydroformylation* (Springer Science & Business Media, 2002).

189. Bohnen, H.-W. & Cornils, B. Hydroformylation of alkenes: An industrial view of the status and importance (2002).

190. Haumann, M. & Riisager, A. Hydroformylation in room temperature ionic liquids (RTILs): catalyst and process developments. *Chemical Reviews* **108,** 1474–1497 (2008).

191. Lang, R. *et al.* Hydroformylation of olefins by a rhodium single-atom catalyst with activity comparable to RhCl $(PPh_3)_3$. *Angewandte Chemie International Edition* **55,** 16054–16058 (2016).

192. Amsler, J. *et al.* Prospects of heterogeneous hydroformylation with supported single atom catalysts. *Journal of the American Chemical Society* **142,** 5087–5096 (2020).

193. Gao, P. *et al.* Phosphorus coordinated Rh single-atom sites on nanodiamond as highly regioselective catalyst for hydroformylation of olefins. *Nature communications* **12,** 4698 (2021).

194. Li, T. *et al.* Styrene hydroformylation with in situ hydrogen: regioselectivity control by coupling with the low-temperature water-gas shift reaction. *Angewandte Chemie* **132,** 7500–7504 (2020).

195. Zheng, Y. *et al.* Boosting the hydroformylation activity of a Rh/CeO_2 single-atom catalyst by tuning surface deficiencies. *ACS Catalysis* **13,** 7243–7255 (2023).

196. Farpón, M. G. *et al.* Rhodium Single-Atom Catalyst Design through Oxide Support Modulation for Selective Gas-Phase Ethylene Hydroformylation. *Angewandte Chemie International Edition* **62,** e202214048 (2023).

197. Jurado, L. *et al.* Highly dispersed Rh single atoms over graphitic carbon nitride as a robust catalyst for the hydroformylation reaction. *Catalysis science & technology* **13,** 1425–1436 (2023).

198. Bourgund, A. *et al.* Influence of local defects on the dynamics of O-H bond breaking and formation on a magnetite surface. *The Journal of Physical Chemistry C* **123,** 19742–19747 (2019).

Die approbierte gedruckte Originalversion dieser Dissertation ist an der TU Wien Bibliothek verfügbar.
The approved original version of this doctoral thesis is available in print at TU Wien Bibliothek.
TU Bibliothek Your knowledge hub WIEN

199. Lee, C. J., Sharp, M. A., Smith, R. S., Kay, B. D. & Dohnálek, Z. Adsorption of ethane, ethene, and ethyne on reconstructed Fe_3O_4(001). *Surface Science* **714,** 121932 (2021).

200. Gedanken, A., Kuebler, N. & Robin, M. An MPI search for the $\pi \rightarrow 3p$ Rydberg states of ethylene. *The Journal of Chemical Physics* **76,** 46–52 (1982).

201. Wilden, D. & Comer, J. Rydberg states of C_2H_4 and C_2D_4: assignments using the technique of low-energy electron energy-loss spectroscopy. *Journal of Physics B: Atomic and Molecular Physics* **13,** 1009 (1980).

202. Mulliken, R. S. The excited states of ethylene. *The Journal of Chemical Physics* **66,** 2448–2451 (1977).

203. McMurchie, L. E. & Davidson, E. R. Singlet Rydberg states of ethylene. *The Journal of Chemical Physics* **67,** 5613–5618 (1977).

204. Peng, H., Yang, Z.-H., Perdew, J. P. & Sun, J. Versatile van der Waals density functional based on a meta-generalized gradient approximation. *Physical Review X* **6,** 041005 (2016).

205. Yang, J. H., Kitchaev, D. A. & Ceder, G. Rationalizing accurate structure prediction in the meta-GGA SCAN functional. *Physical Review B* **100,** 035132 (2019).

206. Sun, J. *et al.* Accurate first-principles structures and energies of diversely bonded systems from an efficient density functional. *Nature chemistry* **8,** 831–836 (2016).

207. Liang, Z. *et al.* Adsorption and oxidation of ethylene on the stoichiometric and O-rich RuO_2(110) surfaces. *The Journal of Physical Chemistry C* **121,** 20375–20386 (2017).

208. Chen, L., Smith, R. S., Kay, B. D. & Dohnálek, Z. Adsorption of small hydrocarbons on rutile TiO_2(110). *Surface Science* **650,** 83–92 (2016).

209. Nie, S. *et al.* Insight into magnetite's redox catalysis from observing surface morphology during oxidation. *Journal of the American Chemical Society* **135,** 10091–10098 (2013).

Die approbierte gedruckte Originalversion dieser Dissertation ist an der TU Wien Bibliothek verfügbar.
The approved original version of this doctoral thesis is available in print at TU Wien Bibliothek.
TU Bibliothek Your knowledge hub WIEN

210. Baxter, E. T., Ha, M.-A., Cass, A. C., Alexandrova, A. N. & Anderson, S. L. Ethylene dehydrogenation on $Pt_{4,7,8}$ clusters on Al_2O_3: Strong cluster size dependence linked to preferred catalyst morphologies. *Acs Catalysis* **7,** 3322–3335 (2017).

211. Mahapatra, M. *et al.* The evolution of model $Rh/Fe_3O_4(001)$ catalysts in hydrogen environments. *Surface Science,* 122617 (2024).

212. Crabtree, R. H. Dihydrogen complexes: some structural and chemical studies. *Accounts of Chemical Research* **23,** 95–101 (1990).

213. Heinekey, D. M., Lledós, A. & Lluch, J. M. Elongated dihydrogen complexes: what remains of the H–H Bond? *Chemical Society Reviews* **33,** 175–182 (2004).

214. Kubas, G. J. Fundamentals of H_2 binding and reactivity on transition metals underlying hydrogenase function and H_2 production and storage. *Chemical reviews* **107,** 4152–4205 (2007).

215. Kubas, G. J. Molecular hydrogen complexes: coordination of a. sigma. bond to transition metals. *Accounts of Chemical Research* **21,** 120–128 (1988).

216. Di Liberto, G., Cipriano, L. A. & Pacchioni, G. Role of dihydride and dihydrogen complexes in hydrogen evolution reaction on single-atom catalysts. *Journal of the American Chemical Society* **143,** 20431–20441 (2021).

217. Zdeněk, J. *Surface science studies of iron oxides as model catalyst supports* PhD thesis (Technische Universität Wien, 2020).

Die approbierte gedruckte Originalversion dieser Dissertation ist an der TU Wien Bibliothek verfügbar.
The approved original version of this doctoral thesis is available in print at TU Wien Bibliothek.
TU Bibliothek Your knowledge hub WIEN

List of Publications

The publications I have co-authored during my time as a phd student at the Institute of Applied Physics are listed below:

1. Kraushofer, F., **Haager, L.**, Eder, M., Rafsanjani-Abbasi, A., Jakub, Z., Franceschi, G., Riva, M., Meier, M., Schmid, M., Diebold, U., Parkinson, G. S. **Single Rh adatoms stabilized on α-$Fe_2O_3(1\bar{1}02)$ by coadsorbed water.** ACS Energy Letters 7, 375–380 (2021).

2. Sombut, P., **Puntscher, L.**, Atzmueller, M., Jakub, Z., Reticcioli, M., Meier, M., Parkinson, G. S., Franchini, C., **Role of Polarons in Single-Atom Catalysts: Case Study of Me_1 [Au_1, Pt_1, and Rh_1] on $TiO_2(110)$.** Topics in Catalysis 65, 1620–1630 (2022).

3. **Puntscher, L.**, Daninger, K., Schmid, M., Diebold, U., Parkinson, G. S. **A study of Pt, Rh, Ni and Ir dispersion on anatase $TiO_2(101)$ and the role of water.** Electrochimica Acta 449, 142190 (2023).

4. **Puntscher, L.**, Sombut, P., Wang, C., Ulreich, M., Pavelec, J., Rafsanjani-Abbasi, A., Meier, M., Lagin, A., Setvin, M., Diebold, U., Franchini, C., Schmid, M., Parkinson, G. S. **A Multitechnique Study of C_2H_4 Adsorption on $Fe_3O_4(001)$.** The Journal of Physical Chemistry C 127, 18378–18388 (2023).

5. Wang, C., Sombut, P., **Puntscher, L.**, Jakub, Z., Meier, M., Pavelec, J., Bliem, R., Schmid, M., Diebold, U., Franchini, C., Parkinson, G. S. **CO-induced dimer decay responsible for gem-dicarbonyl formation on a model single-atom catalyst.** Angewandte Chemie 136, e202317347 (2024).

6. Wang, C., Sombut, P., **Puntscher, L.**, Ulreich, M., Pavelec, J., Rath, D., Balajka, J., Meier, M., Schmid, M., Diebold, U., Franchini, C., Parkinson, G.

Die approbierte gedruckte Originalversion dieser Dissertation ist an der TU Wien Bibliothek verfügbar.
The approved original version of this doctoral thesis is available in print at TU Wien Bibliothek.
TU Bibliothek Your knowledge hub WIEN

S. **A Multi-Technique Study of C_2H_4 Adsorption on a Model Single-Atom Rh_1 Catalyst.** The Journal of Physical Chemistry C 128, 15404–15411 (2024).

7. Rafsanjani-Abbasi, A., Buchner, F., Lewis, F. J., **Puntscher, L.**, Kraushofer, F., Sombut, P., Eder, M., Pavelec, J., Rheinfrank, E., Franceschi, G., Birschitzky, V., Riva, M., Franchini, C., Schmid, M., Diebold, U., Meier, M., Madsen, G. K. H., Parkinson, G. S. **Digging Its Own Site: Linear Coordination Stabilizes a Pt_1/Fe_2O_3 Single-Atom Catalyst.** ACS nano (2024).

Die approbierte gedruckte Originalversion dieser Dissertation ist an der TU Wien Bibliothek verfügbar.
The approved original version of this doctoral thesis is available in print at TU Wien Bibliothek.

List of Prizes

The awards I have received during my time as a phd student at the Institute of Applied Physics are listed below:

1. **Student poster price**, at the Cluster Meeting 2021 in Prague
2. **Platinum Award for Outstanding Student Presentation**, at the American Vacuum Society Symposium 2021 (Fundamental Discoveries in Heterogeneous Catalysis Focus Topic; Graduate Student Presentation Award)
3. **Franz Viehböck Young Investigator Prize 2021**, at the TU Vienna
4. **IUVSTA-Elsevier Student Award**, at the International Vacuum Congress 2022 in Japan

Die approbierte gedruckte Originalversion dieser Dissertation ist an der TU Wien Bibliothek verfügbar.
The approved original version of this doctoral thesis is available in print at TU Wien Bibliothek.
TU Bibliothek Your knowledge hub WIEN